AUTOMATIC QUANTIFICATION OF BRAIN MIDLINE SHIFT IN CT IMAGES

BY

RUIZHE LIU

A THESIS SUBMITTED

FOR THE DEGREE OF DOCTOR OF PHILOSOPHY

AT

DEPARTMENT OF COMPUTER SCIENCE

SCHOOL OF COMPUTING

NATIONAL UNIVERSITY OF SINGAPORE

COMPUTING 1, 13 COMPUTING DRIVE, SINGAPORE 117417

FEB, 2012

Name: Liu Ruizhe

Degree: Doctor of Philosophy

Department: Department of Computer Science, School of Computing

Thesis Title: **Automatic Quantification of Brain Midline Shift in CT Images**

Abstract:

Computer Tomography (CT) images of traumatic brain injury (TBI) are widely used for clinical diagnosis. Pathological features on these images such as the volume and type of hemorrhage regions, the amount of brain midline shift, and the volume of ventricle are important indicators based on which decision of treatment or prognosis is made. Among the various clinical features, brain midline shift (MLS) is a significant factor in TBI diagnosis, which is a major cause of death. It indicates the severity of injury and the chance of survival of patients. Many studies have been carried out to find the associations between MLS and the injury outcomes such as disability or mortality. However, in these studies, measurements of MLS are either quantitatively measured manually by experts or described qualitatively. Due to the lack of quantified data in large population, no precise or reliable statistical figures can be obtained. In addition, there may be many unknown associations to be discovered if large quantified datasets are available. Therefore, automatically quantifying the MLS in CT image has become an urgent task for TBI prognosis research. Once efficient quantifying methods are developed and applied to large brain image database, finding precise and reliable statistical figures and building fast and effective predictive models for TBI prognosis will become a much easier task. Techniques to be developed in this thesis will provide prognosis research in TBI with significantly rich amount of quantified image data, specifically, the quantified brain midline shift, which have never been available before to doctors and researchers. With the new methods and findings, new prototype online retrieval system is to be developed. It is hoped that outcomes from the present project will eventually benefit the traumatic brain injury clinical diagnosis, treatment, patients' survival and recovery.

Keywords: Medical Imaging, Computer Tomography (CT), Traumatic Brain Injury (TBI), Indexing of Brain Slices, Brain Tissue Segmentation, Hemorrhage Detection, Brain Midline Shift, Computer-assisted Diagnosis (CAD), Content-based Retrieval (CBIR)

ACKNOWLEDGEMENT

I would like to express my deep and sincere gratitude to all those people who have offered their ingenious ideas and invaluable support continuously throughout this research work. This thesis would not have been possible without their generous contributions in one way or another.

I am deeply grateful to my supervisor, Professor Chew Lim Tan in School of Computing, National University of Singapore, for his valuable supervision and guidance along the way from the topic selection to the completion of this thesis. His wide knowledge and constructive advice have inspired me with various ideas to tackle the difficulties and attempt new directions. He has also been very supportive in purchasing experimental equipments used in this research. His kind guidance and support have been of great value to me.

I wish to thank Dr. Shimiao Li, in School of Computing, National University of Singapore, for her insightful advice and comprehensive comments on the thesis works. Moreover, her detailed and constructive suggestions have helped me greatly in improving several papers towards their final publications.

I owe my sincere gratitude to Professor Wynne Hsu, and Associate Professor Tze Yun Leong in School of Computing, National University of Singapore, for their detailed reviews, constructive comments and suggestions to my graduate research paper and thesis proposal during the whole research program.

I wish to extend my warmest thanks to all those colleagues and friends who have helped me and encouraged me in one way or another during my research study in the Center for Information Mining and Extraction (CHIME) lab[1] of School of Computing, National University of Singapore.

Last but not least, I wish to express my special gratitude to my loving parents for their continual support and understanding throughout my undergraduate and postgraduate studies abroad for all these years. Specially, I wish to express my deep memorials of my late father, who was a great professor in the Chinese Academy of Science (CAS), for his wise help and support during my first three-year research.

[1] Currently Artificial Intelligence Lab 2

TABLE OF CONTENT

LIST OF FIGURES

LIST OF TABLES

LIST OF EQUATIONS

LIST OF ACRONYMS

AMM	Anatomical Marker Model
CAD	Computer-assisted Diagnosis
CBIR	Content-based Information Retrieval
CSF	Cerebrospinal Fluid
CT	Computer Tomography
DSCC	Directional Single Connected Chain
DML	Deformed Midline
EDH	Extradural Hematoma
FT	Fourier Transform
GMM	Gaussian Mixture Model
ICH	Intracerebral Hemorrhage
ICSM	Image to Curved Surface Matching
ICU	Intensive Care Unit
IML	Ideal Midline
IMSP	Ideal Middle Sagittal Plane
IPSM	Image to Planar Surface Matching
MLS	Midline Shift
MR	Magnetic Resonance

MRI	Magnetic Resonance Image
MS	Middle Slice
NMI	Normalized Mutual Information
PMV	Probability Map of Ventricles
ROI	Region of Interest
SDH	Subdural Hematoma
TBI	Traumatic Brain Injury
WT	Wavelet Transform

Chapter 1

INTRODUCTION

1.1 Motivation

Clinical prognosis is doctor's prediction on the possible development or likely outcome of an illness. Knowing the prognosis can help apply certain treatments in a more sensible way and avoid predictable crisis, thus shortening the recovery time or increasing the survival chance [Moons09]. Prognosis is usually based on doctor's previous experience and knowledge of associations between clinical findings and possible illness outcomes. It may be inaccurate due to the limitation of individual doctor's experience. Statistical figures on large populations, showing the relationships between important prognostic indicators and their associated outcome, help to overcome this limitation and increase the accuracy of prognosis. Using these figures, prognosis can be made based on the statistics gathered from a huge number of previous cases with similar prognostic indicators. Prognosis models have been built based on these statistics. For example, in intensive care unit (ICU), the APACHE II score, which is calculated from 12 routine physiological measurements, is an important indicator to measure the severity and predict the patient mortality [Knaus85]

[Knaus91]. However, in many areas, reliable and precise statistical figures for prognosis are still missing.

In particular, in modern hospitals, medical imaging such as CT or MR has been playing an important role in clinical diagnosis. Pathological features found in medical images are used as important indicators for outcome prediction. Traditionally, medical image interpretation by radiologists has been mainly a qualitative perception process. Radiology reports describe findings in images by qualitative words such as ‘small’, ‘large’, ‘mild’ etc. It is rare to see precisely quantitative measurements in those reports. In prognosis research, due to the lack of tools to quantify the pathological image features efficiently, current studies on the associations between clinical feature indicators in image and outcomes are mainly based on qualitative feature descriptions extracted from radiologist reports. Such feature descriptions, while being used for getting statistical figures from large population, suffer from reading inconsistency among different radiologists.

To overcome the inconsistency, many studies are based on re-read feature descriptions by one expert. However, the re-reading process makes a large population study very time-consuming and expensive. More importantly, studies based on qualitative feature descriptions do not provide precise knowledge on the associations. A deeper understanding can only be obtained when the associations are quantitatively well estimated.

In another aspect, with the fast development of medical imaging devices and image processing techniques, the research community in medical imaging is prospecting that future radiological interpretation will be changing towards quantitative image assessment [Boone07][Daniel08]. This will require efficient methods to extract robust quantitative data from images. Such data, once available, might significantly change the current situation of clinical prognosis research.

In particular, in traumatic brain injury (TBI) [Silver05], which is a major cause of death, brain CT images are widely used for clinical diagnosis. Pathological features on these images, such as the volume and type of hemorrhage regions, the amount of brain midline shift, and the volume of ventricle, are important indicators based on which decision of treatment or prognosis is made. Many studies have been carried out to find the associations between these findings from images and the outcomes; for example, on the relationship between brain midline shift and the recovery of consciousness [Ross89], on the relationship between brain midline shift and the chance of survival [Sucu06], on the relationship between hemorrhage location and patient mental status and motor function [Andrews88], on the relationship between Marshall CT classification (which is a combination of a group of qualitative findings in the brain CT image) and patient mortality [Maas05]. However, in these studies, findings of image features are either quantitatively measured manually by experts or described qualitatively. In the former case, studies are only based on datasets of small number of patients (less than 100) due to the time consuming labor work, despite the

fact that huge amount of brain image data and the associated outcome information is stored in the hospital database systems. In the latter case, datasets suffer from inconsistency as discussed. In both cases, due to the lack of quantified data in large populations, no precise or reliable statistical figures can be obtained. In addition, there may be many unknown associations to be discovered in large quantified datasets.

Therefore, quantifying clinical features automatically in CT or MR image has become an urgent task for TBI prognosis research. Once efficient quantifying methods are developed and applied to large brain image databases, finding precise and reliable statistical figures and building fast and effective predictive models for TBI prognosis will become a much easier task.

Among the various clinical features, brain midline shift (MLS) is a significant factor in TBI, which is a major cause of death. It has been related to the severity of injury and the chance of survival of patients [Quattrocchi91] [Marshall91] [Gruen02] [Maas08]. Many studies have been carried out to find the associations between MLS and injury outcomes such as disability or mortality. In brain CT images, the brain midline is a line connecting the centers of the attachment of the falx (Figure 1.1). It is not a human anatomical feature, but an imaginary line dividing the brain into two equal hemispheres. Ideally, the midline should be a straight line, called ideal midline (IML). Severe brain trauma will cause swelling inside the brain, which adds imbalanced pressures to the left and right hemispheres. The imbalanced pressure will

further deform the ideal midline to a curve, which is called the *deformed midline* (DML).

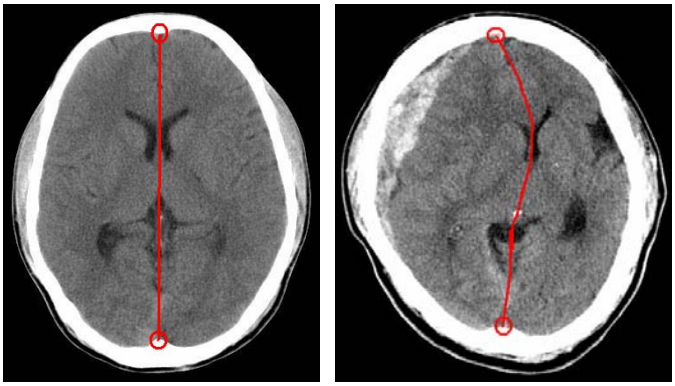

Figure 1.1. Left: IML. Right: DML.

Techniques reported in this thesis describe prognosis research in TBI with significantly rich amount of quantified image data, specifically quantified brain midline shift, which have never been available before to doctors and researchers. With the new methods and findings, new prototype online retrieval system is to be developed. It is hoped that outcomes from the present project will eventually benefit TBI clinical diagnosis, treatment, patient survival and recovery.

1.2 Technical Challenges and Contributions of the Thesis

The challenges and contributions of this work impact both computer science and clinical studies.

1.2.1 Challenges and contributions on medical image processing

Firstly, there are limited works addressing the problem of brain midline shift detection in CT images. This is mainly due to the following difficulties. Firstly, the midline is not a real anatomical feature, but an imaginary centerline dividing the brain into equal halves. Hence it cannot be segmented using conventional segmentation algorithms. Secondly, because of the noise and low contrast of CT images, brain tissues such as ventricles and brain matters are displayed with weakly defined boundaries. From Figure 1.2 we see that there is only a single peak in the intensity histograms of the brain CT slice. It is hence hard to separate the brain tissues based only on intensity histograms. Therefore it is difficult to identify the brain anatomical structures using this kind of intensity based method. Thirdly, because TBI is unpredictable, the damages can happen at random location of the brain with an arbitrary level of severity. Thus the brain structure is arbitrarily distorted. As a result, it is problematic to design a similarity function or probabilistic atlas to cope with these unpredictable variations and abnormalities [Liu.Jm10]. Therefore, to overcome these difficulties, the thesis proposes a new algorithm to automatically trace and quantify the brain midline shift from TBI CT images. Specifically, the work proposes an anatomical marker model (AMM) to model the brain midline shift. Instead of extracting of the brain midline directly from the image, the model attempts to find the *midline shift markers*. An algorithm based on the AMM is developed. The

experimental results show its advantage in accuracy, time efficiency and robustness comparing with the literature.

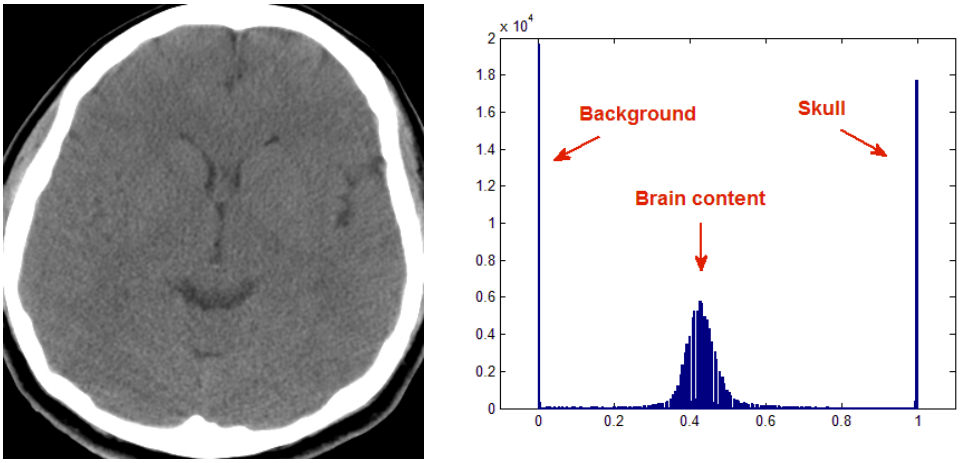

Figure 1.2. The intensity histogram of a CT image.

Secondly, the thesis proposes a probabilistic spatial relationship model to improve the robustness of MLS marker detection and falx segmentation. The spatial relationship model is not only operated on brain CT slices, but also can be extended on MR images.

Thirdly, according to our literature review, there is no method presently available to extract the brain falx from brain CT images. This is because of the following difficulties. Firstly, the brain falx is normally weakly displayed in brain CT images. From Figure 1.3a, circled area, we can see that the falx is hard to visualize by human eyes. This is because of the noise and low contrast of the CT images. From Figure 1.3b, we see that it is hard to segment using a standard edge detection algorithm such as sobel and canny edge detector. The edge texture is very complicated at the falx

regions. It is also hard to segment the falx using intensity histograms. For example, the intensity histogram of the lower falx (Figure 1.3c) has only a single peak which corresponds to the brain matter. The intensity of the falx is hard to separate from the brain matter. Therefore, the thesis proposes a brain falx segmentation algorithm using Directional Single Connected Chain (DSCC). The result is promising. This is the first work to segment brain falx on traumatic brain injury CT images.

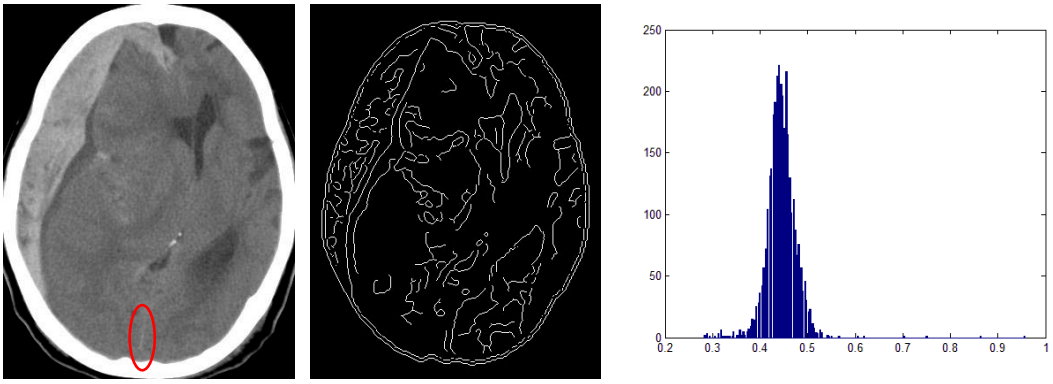

a *b* *c*

Figure 1.3. Left: The falx (circled). Middle: The edge map using Canny edge detector. Right: the intensity histogram of lower falx (circled area).

1.2.2 Contribution on clinical study

Firstly, the work proposes a new measurement for MLS quantification, namely, the area ratio. It complements the traditional measurement, the maximum distance. The measurement has been proposed to doctors for clinical study.

Secondly, based on the proposed midline shift tracing and quantification algorithm, a content-based information retrieval (CBIR) system of TBI brain CT images is built. The system will retrieve patient data not only based on

meta-information such as age, gender, name, admission date/time, etc. but also on abnormalities such as the midline shift amount, and the hemorrhage size, etc.

Thirdly, brain slice indexing helps doctors to retrieve images at the same height level (refer to Chapter 2 section 2.2.1) from large amount of different patient CT scans. It also helps doctors to retrieve images of the same height of one patient in multiple scans to monitor the evolution of the brain injury or the treatment process.

Fourthly, the work provides a large amount of quantified brain midline shift data. This fills the gap between prognostic research and raw image data and between clinical research and raw CT images. Moreover, the quantified data make the clinical MLS measurements consistent. It gives accurate and objective numbers instead of qualitative statement such as “large”, “small”, “significant”, etc. which are inconsistently and subjectively used by different doctors.

1.3 Overview of Problems and Solutions

The proposed algorithm automatically quantifies MLS from TBI CT images. Technically, given a series of TBI CT images (Appendix) from a single patient, the expected output is:

(a) The deformed midline traced and delineated.

(b) The quantification measurements of shifting amount of the MLS.

The proposed algorithm flow is shown in Figure 1.4. The input is firstly preprocessed. Then it is input to the AMM. The model has two components, the markers detection and the markers selection. The marker detection includes skull detection, ventricle detection and falx detection. The marker candidates from ventricle and falx detections are then input to the selection module. The midline is described by the selected markers and then quantified. The quantified value is finally output. Detail of each component will be explained systematically in later chapters.

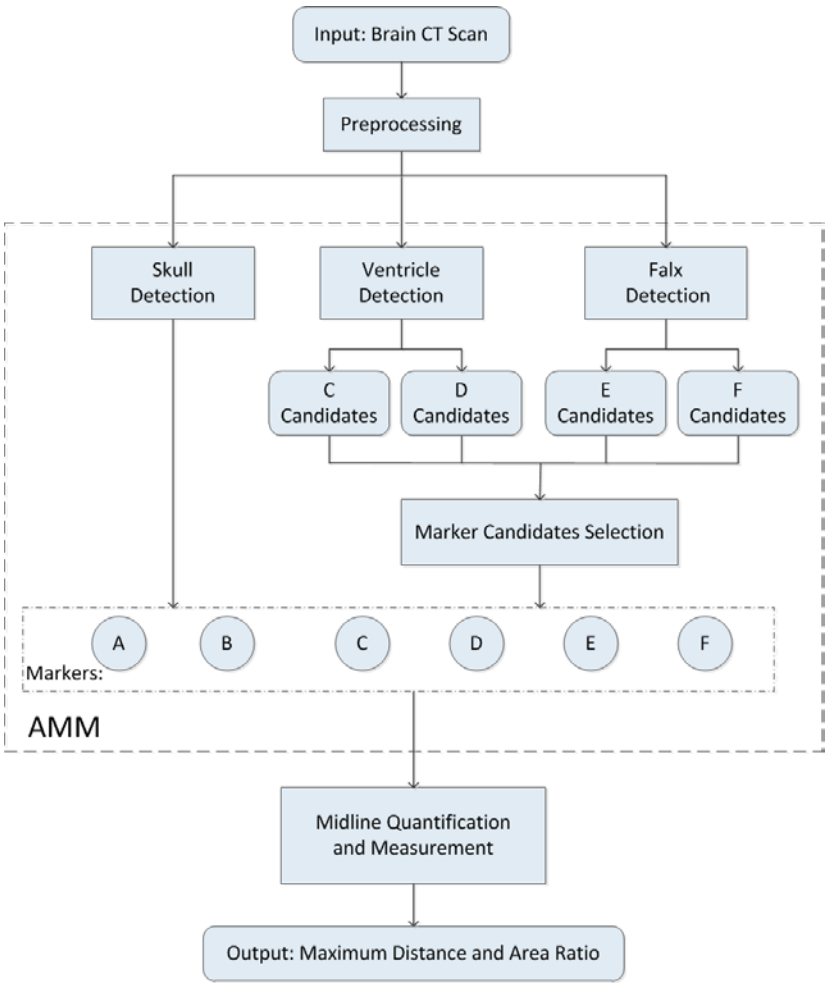

Figure 1.4. The proposed algorithm flow.

1.4 Thesis Structure

The thesis is organized into 8 chapters as follows.

Chapter 1 gives an introduction to the motivation and contribution.

Chapter 2 introduces background knowledge used in the thesis.

Chapter 3 reviews related work in brain midline shift detection.

Chapter 4 presents the preprocessing step in the main algorithm.

Chapter 5 presents the proposed model, the AMM for the midline tracing. The two components of the AMM, namely, the marker candidate detection and the marker candidate selection, are also presented in this chapter. Moreover, the quantification measurements of the midline shift are introduced.

Chapter 6 reports the experiments based on the proposed evaluation methods. Results are compared with all current midline shift detection methods.

Chapter 7 introduces further works carried out by the author, including work on brain slice indexing and on hemorrhage effect study.

Chapter 8 gives the conclusion of the thesis.

Chapter 2

BACKGROUND KNOWLEDGE

This thesis investigates the automatic quantification of brain midline shift from brain CT scan images. Before stepping further into the main part of the thesis, relevant medical background such as CT, and brain anatomical structure, brain traumas are introduced first in this chapter.

2.1 Computerized Axial Tomography

Modern neuroimaging may be one of the greatest stories in medicine. The commercial availability of computerized axial tomography (CT) in the early 1970s heralded remarkable advances in the area of radionuclide brain scanning. CT is now recognized as one of the greatest advances to support diagnosis since the discovery of X-rays. Since its development in 1972, CT quickly became established as the foremost, and often the only technique required in diagnosing brain pathology.

CT brain scan images are produced by computerized reconstruction of a slice of head tissues which has been analyzed by a moving X-ray beam. The patient lies comfortably on a bed with his head in the aperture of the gantry (Figure 2.1). This

contains the X-ray tube and detectors which generate digital information from each slice. This digital information is then processed by the computer to produce the images. Depending on the machine, processing data for each slice takes from 10 to 60 seconds, and a full routine examination takes about 20-60 minutes [Orrison95].

Figure 2.1. CT Scanner.

Particularly, in brain CT scans, each slice image represents a slice of brain tissue and the slices are presented in sequence from the bottom of the brain upwards. A slice is usually 5-10 mm thick. By reviewing a sequence of slices, one is able to build up a mental picture of the whole brain and 3-D CAD modules can be constructed. The standard position of the slices and their visual sequence are shown in Figure 2.2. Many machines are capable of scanning (or recalculating the data) into other planes, for example, sagittal or coronal. [Bradshaw87]

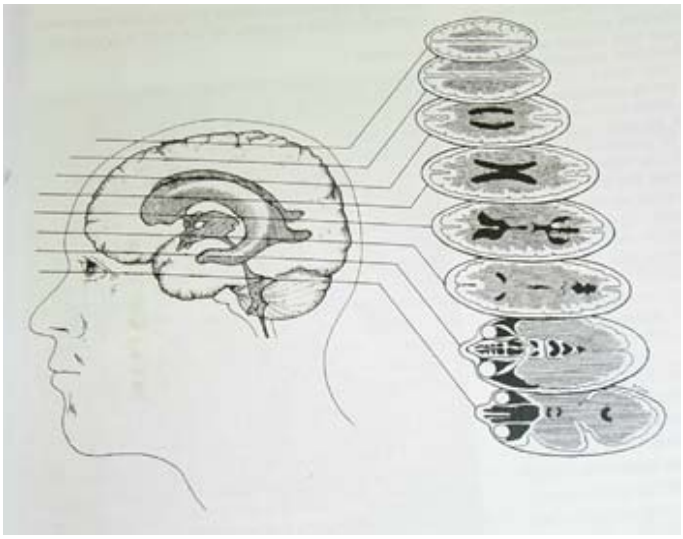

Figure 2.2. CT Slices. [Bradshaw87]

CT brain scan captures the different densities of air tissues and bones. Indeed this range is presented on most images in clinical use. Air is shown as black and bone as white, with all the intervening densities as varying shades of grey. These intensities are quantified with the "Hounsfield Unit", which was established by Godfrey Newbold Hounsfield, one of the principal engineers and developers of computed axial tomography. The Hounsfield unit (HU) is a linear scale quantifying the material. Mathematically, for a material X with linear attenuation coefficient μ, the corresponding HU value is given by the following formula:

$$HU_x = \frac{\mu_x - \mu_{H_2O}}{\mu_{H_2O} - \mu_{air}} \times 1000 \qquad (2.1)$$

The densities encountered in most scans are shown in Figure 2.3 (their approximate numerical values in Hounsfield units are given). Note that air and fat are difficult to distinguish visually, and so are calcification and bone. In this case, radiologists will check their Hounsfield unit value to differentiate them. Moreover,

the values of grayscales can be adjusted by varying the settings (known as window width and level) of the imaging systems. Typically, the brain CT scans use the brain window to see the blood clots and the bone window to see the fractures (Figure 2.4).

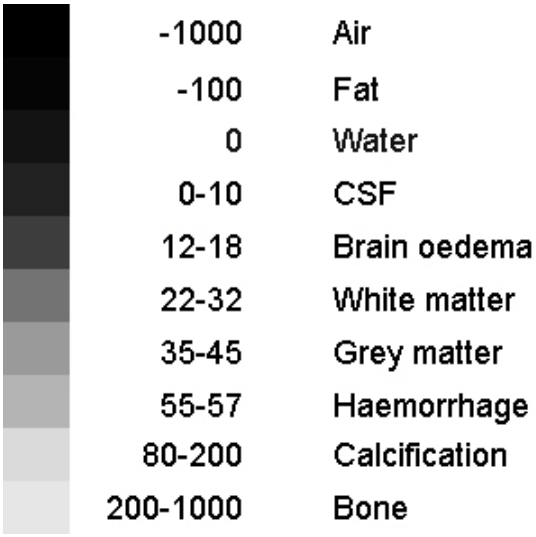

Figure 2.3 Hounsfield units for body tissues, lesions, water and air.

The intensity in Figure 2.3 gives valuable information for brain tissue segmentations. For example, skulls are bones and have HU 200-1000 according to Figure 2.3. The cerebrospinal fluid (CSF) is an organic liquid inside the brain space which has HU 0-10 according to Figure 2.3. Ventricles contain mostly CSF. Therefore, by intensity difference, we can separate skull and ventricles from other tissues.

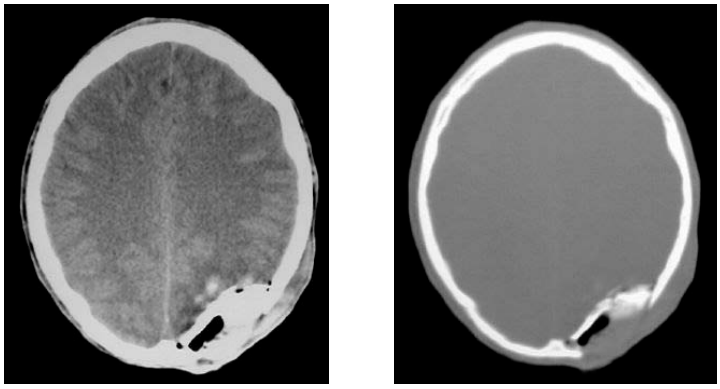

Figure 2.4. Brain window (left) vs. bone window (right).

2.2 Anatomical Structure

2.2.1 The six height levels

One axial brain CT scan consists of multiple 2D slices at different heights along the axial direction. An entire series of CT scans is illustrated in Appendix. Normally, there are 20 slices and the physical distance between each slice is around 5mm. Note that some slices have similar anatomical structure and appearance and can be grouped accordingly. For diagnostic purpose, the slices are normally grouped into 6 levels [Lin00] (Figure 2.5).

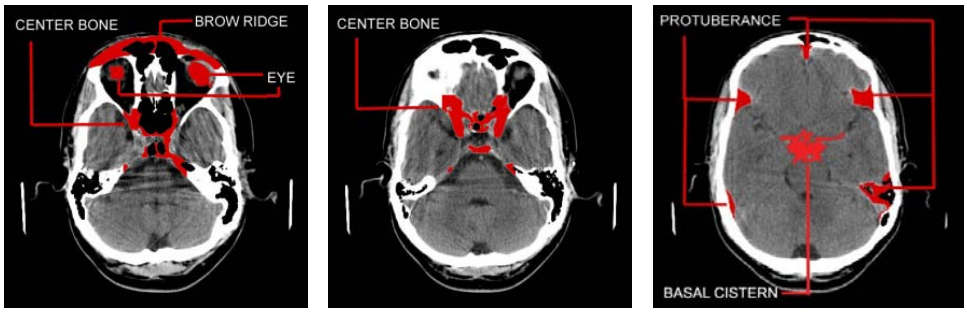

LEVEL 1 LEVEL 2 LEVEL 3

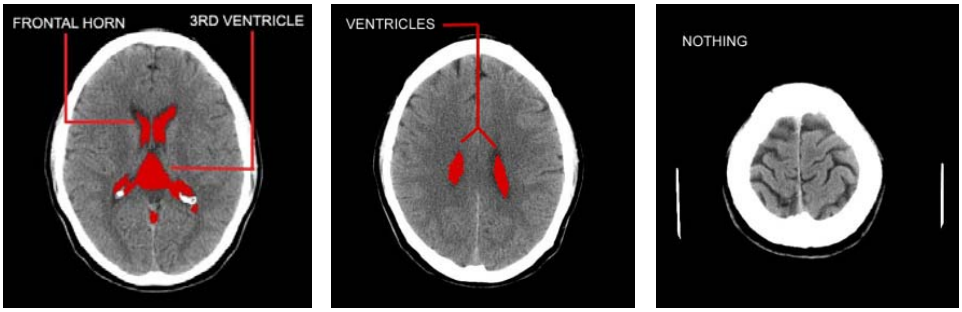

LEVEL 4 LEVEL 5 LEVEL 6

Figure 2.5. Anatomical structure of the slices.

Level 1 is the nasal cavity region; level 2 is the transition from the nasal cavity to the encephalic region; levels 3 to 5 are the encephalic region, which contains the most important slices for TBI diagnosis; level 6 is the top region. Particularly, level 3 has remarkable dents (marked in red) along inner contour of the skull and basal cistern at the center; level 4 contains the frontal horn and the third ventricle; level 5 is the transition from the encephalic region to the top region. We call these three levels *encephalic levels*. The purpose of separation and renaming of encephalic levels is that the models and algorithms proposed in later chapters mainly process encephalic levels instead of the entire scan series. Some anatomical feature landmarks used in our work are also shown in Figure 2.5.

2.2.2 The middle slice (MS)

One contribution of the thesis is proposing the concept of '*middle slice*'. Based on our observations on CT scans of hundreds of patients, it is observed that, in the encephalic region, the size of the bounding box of the skull varies following a regular pattern from the bottom slice upwards to the top slice. It firstly grows, and then shrinks (Figure 2.6).

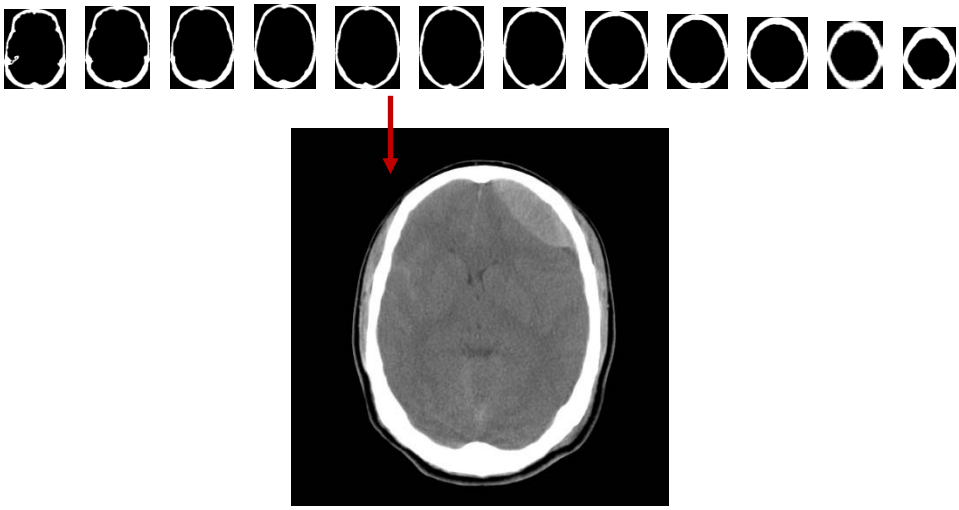

Figure 2.6. The bounding box of skulls through CT slices. Note that the fifth one has the maximum area, which corresponds to the lower image.

We denote the slice with maximum skull bounding box size as '*Middle Slice*' (*MS*) (Figure 2.7). Each CT scan series contains one MS. According to our observation on hundreds of CT scans[1], the MS has the following anatomical properties:

- *The bounding box of the skull has maximum area. (by definition).*
- *The skull is closed.*

[1] The data set is shown in Chapter 6 Section 6.1.1

- *The attachments of falx are present.*
- *The frontal horn and the 3rd ventricle are present.*

Note that the MS also falls in height level 4 in Figure 2.5.

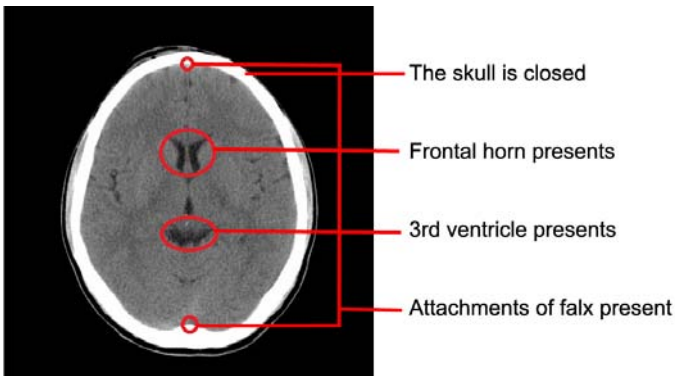

Figure 2.7. The middle slice (MS) from the sequence in Figure 2.6.

The MS is used in midline shift detection. Clinically, the midline shift is observed on the 4th level. It is because the deformation of anatomical tissues is largest in this level. Moreover, the midline shift markers used in clinical study are the attachments of falx, the frontal horn, and the third ventricle. They all appear on this middle slice. Thus to detect the midline shift in an entire scan series, one could pick the MS and do midline shift detection on the MS. This saves computational resources and is consistent to the clinical diagnosis.

2.2.3 The layers of the head and brain

As one of the most important organs, human brain is protected by many layers. As illustrated in Figure 2.8, the outside layer is scalp, where human hairs grow. Below the scalp is the skull, the bone protecting the brain. The brain also has multiple layers.

The outside layer is the dura matter; there are vessels on its surface and also beneath it. Below the dura, from outside inwards, there are layers called arachnoid, pia mater, and brain tissue [Element].

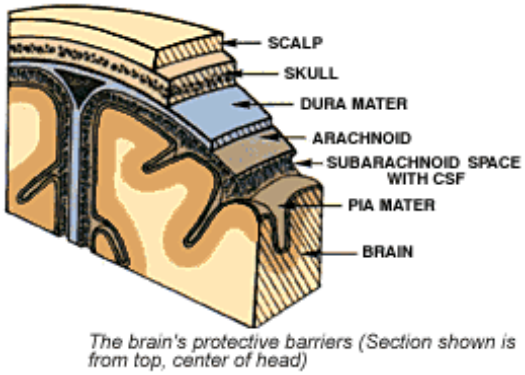

Figure 2.8. The brain layers.

2.3 Traumatic Brain Injury, Hemorrhage and Midline Shift

Traumatic brain injury is defined as damage to the brain resulting from external mechanical force, such as rapid acceleration or deceleration, impact, blast waves, or penetration by a projectile [Maas08]. Brain function is temporarily or permanently impaired and structural damage may or may not be detectable with current technology [Parikh07]. TBI is one of two subsets of acquired brain injury (brain damage that occurs after birth or non-congenital). The other subset is non-traumatic brain injury, which does not involve external mechanical force (examples include stroke and infection) [Chapman99][Collins02]. All traumatic brain injuries are head injuries, but the latter term may also refer to injury to other parts of the head.[Blissitt06][Hannay04] [Jennett98]. However, the terms “head injury” and “brain injury” are often used interchangeably [McCaffrey97].

The preferred radiological test in the emergency setting of TBI is CT [Barr07]. Magnetic resonance imaging (MRI) can show more detail than CT, and can add information about expected outcome in the long term [Valadka04]. It is more useful than CT for detecting injury characteristics such as diffuse axonal injury in the longer term [Maas08]. However, MRI is not used in the emergency setting for reasons including its relative inefficacy in detecting bleeds and fractures, its lengthy acquisition time, the inaccessibility of the patient in the machine, and its incompatibility with metal items used in emergency care [Valadka04]. Therefore, TBI patients are diagnosed using CT scans.

Hemorrhages are typical features of traumatic brain injuries. Hemorrhage is bleedings inside the brain. The thesis will mention three types of the hemorrhages, namely extradural hemorrhage (EDH), subdural hemorrhage (SDH), and intracerebral hemorrhage (ICH). These three hemorrhages are introduced briefly next as background knowledge for the later chapters. The introduction is based on tutorials provided in [Dowine].

Extradural hematomas

EDH arises between the inner layer of the skull and the dura matter. The expanding hematoma strips the dura from the skull. The bleeding is quite strong so that the hematoma is confined, giving rise to its characteristic biconvex shape with a well defined margin. The bleeding is usually acute and so high attenuation in CT images. EDH is caused by extremely strong strikes on the head. Based on prognostic

research, one large EDH is fatal. Therefore, there are extremely rare cases where multiple large EDHs are observed clinically. One example is shown in Figure 2.9.

Figure 2.9. Acute extradural hematoma (circled area).

Subdural hematomas

SDH arises between the dura and the arachnoid, often from ruptured veins crossing this space. The space enlarges as the brain tissue becomes atrophic and so subdural hematomas are more common in the elderly.

SDH appearance in CT images is similar to that of the extradural hematoma. Differentiating the two is not so important in the acute situation. The blood generates again high attenuation, but may spread more widely in the subdural space, with a crescent appearance and a more irregular inner margin. We may compare it with the EDH. The bleeding of EDH is more towards the center of the brain so it is a convex shape, while the bleeding of SDH is more along the skull so it is a concave shape. Similar to the EDH, acute SDH is caused by strong strike on the head. Based on prognostic research, one large SDH is deadly. Therefore, there are extremely rare

cases where multiple large SDHs are observed clinically. One example is shown in Figure 2.10.

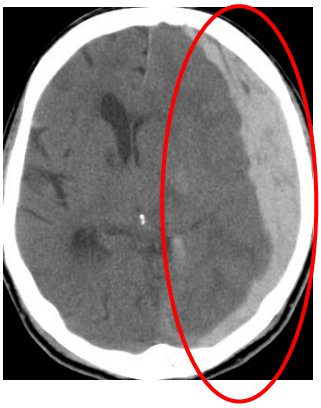

Figure 2.10. Subdural hematoma (circled area).

Intracerebral hemorrhage

ICH is also called hemorrhagic contusion. It is located inside the brain, hence surrounded by brain matters, and always has high attenuation. There can be multiple ICHs occurring inside the brain. One example is shown below (Figure 2.11).

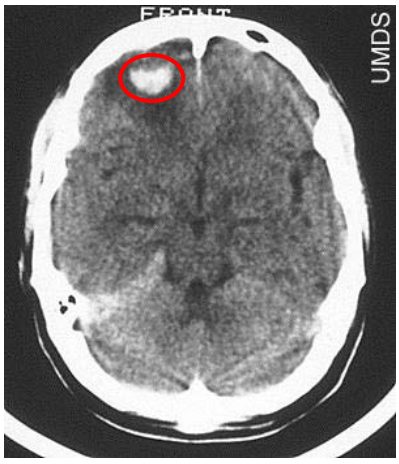

Figure 2.11. Intracerebral hemorrhage (circled area).

We have previously introduced the brain midline (Refer to Chapter 1 on page 4 and 5). Note that the midline will always pass through the centers of attachments of

falx and certain anatomical tissues (Figure 2.12b). For example, in slices at encephalic level 2 (level 4 in Figure 2.5), it always passes through the center of the frontal horn, and the center of the third ventricle (Figure 2.12b). These tissues are used as the 'midline shift markers' clinically. As the midline always passes through those markers, to trace the midline it makes sense to locate them. This is the anatomical marker model proposed in this thesis, which will be discussed in detail in Chapter 5.

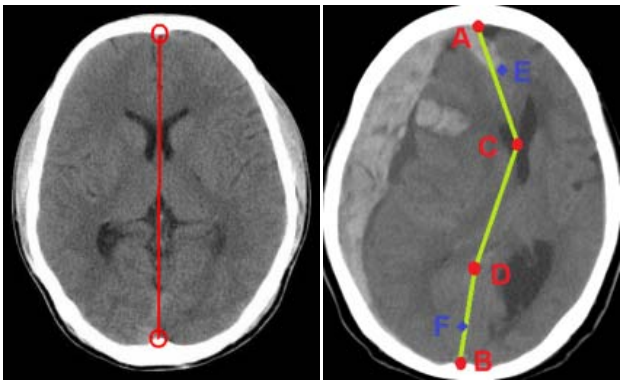

a ***b***

Figure 2.12.The midline shift. *a*: the IML; *b*: encephalic level.

There are strong relationships between hemorrhages and the midline shift, the cause of which is mainly the unbalanced pressure caused by the hemorrhage. Different types of hemorrhages have different effects. The bleeding point of the EDH is out side the dura, so the EDH is generally not large and the midline is generally not shifted significantly. In case of SDH, the bleeding point is under the dura and the bleeding direction is along the skull where little resistance stops the flooding of the blood. Hence the bleeding will accumulate and generally forms a large hemorrhage along the skull. The accumulated blood greatly increases the pressure of the corresponding region of the brain, with great effect on the midline shift. The bleeding of ICH is inside the brain and the location is unpredictable. Due to the protection of

the skull and brain matter, strikes on the head normally do not cause large bleeding inside the brain matters. Hence, ICHs are small in traumatic brain injury. They normally do not have effect on midline shift except for single large ICH occurring around the ideal midline.

2.4 Summary of the Chapter

This chapter has given a brief introduction to CT imaging, brain anatomical structure, traumatic brain injury, hemorrhages. It has also defined the brain midline shift and the middle slice, two crucial items for this work. Particularly, the brain anatomical structure and the relations between hemorrhage and the midline shift have been discussed.

Chapter 3

RELATED WORK ON MIDLINE SHIFT DETECTION

In this chapter, we review literatures on related topics. Firstly, the main topic, work on midline shift detection, is reviewed. Secondly, related work of intermediate steps is reviewed such as work on detection of attachments of falces and work on ventricle segmentation.

3.1 Work on Midline Shift Detection

Brain midline shift (MLS) is a significant factor in TBI diagnosis. It indicates the severity of injury and the chance of survival of patients [Quattrocchi91][Marshall91] [Gruen02][Maas08]. Automatic quantification of MLS helps to study the association between the amount of MLS and clinical outcomes such as mortality or morbidity. However, little work has been reported to measure MLS automatically. This is mainly due to two difficulties in this task. One is that the deformed brain midline is not a visible anatomical feature that can be segmented using conventional image segmentation algorithms. The other difficulty is that the brain structure may be arbitrarily distorted so the midline shift is unpredictable. Based on the literature review, there are only two papers presently addressing the problems of MLS detection:

the symmetry model [Liao06] [Liao10], and the ventricle shape matching model [Chen10].

3.1.1 The Symmetry Model

The symmetry model is proposed by Liao et al. [Liao06][Liao10]. In Liao's method, the deformed midline is modeled as a quadratic Bezier curve. The quadratic Bezier curve is defined by 3 points, $\boldsymbol{P_1}$, $\boldsymbol{P_2}$, and $\boldsymbol{P_3}$, particularly $\boldsymbol{A}$, $\boldsymbol{B}$, and $\boldsymbol{C}$ in Figure 3.1. The task is to compute the 3 control points $\boldsymbol{A}$, $\boldsymbol{B}$, and $\boldsymbol{C}$. Each point has two coordinates, x and y. Hence we have 6 parameters to determine, $\boldsymbol{A}$ (a_x, a_y), $\boldsymbol{B}$ (b_x, b_y), and $\boldsymbol{C}$ (c_x, c_y). However, notice that ending points $\boldsymbol{A}$ and $\boldsymbol{C}$ always reside on the IML, which is defined as the intersection between the slice and the ideal middle sagittal plane (IMSP). Forcing the falx segments to overlap with the IML will align the midline along the coronal direction and make $\boldsymbol{A}$ and $\boldsymbol{C}$ have the same x value, which is also the same as the x value of the falx. Thus, assuming the falx and the vertical axis are located, only 4 parameters need to be estimated, a_y, b_x, b_y, and c_y. According to the symmetry of the brain, the points should be located at the place such that the deformed curve is still the symmetrical axis of the brain (Figure 3.1). Practically, a symmetry score is constructed to estimate the 4 parameters, so that the result value of the 4 parameters should maximize the symmetry.

A symmetry map is used for computing the symmetry scores. The score is defined as the weighted sum of squared difference of the 48 pixels at each side of the IML is calculated for each brain pixel. This corresponds to about 2.4cm laterally and

usually covers anatomical structures such as frontal horns and 3rd ventricle around the midline. Mathematically, we have the following symmetry function

$$S_{i,j} = \sum \left(\left(I_{i+k,j} - I_{i-k,j} \right)^2 \times \frac{48 - k}{48} \right), 1 \leq k \leq 47 \quad (3.1)$$

where $S_{i,j}$ is the symmetry score, $I_{i,j}$ is the pixel located at position (i, j), and k is the distance from the pixel to the IML. The symmetry map is calculated on the brain content without skull. With the symmetry map in hand, the task now is to estimating the parameters a_y, b_x, b_y, and c_y. The target function is minimizing the summed score of each point of the deformed midline on symmetry map. One point of the deformed midline is found for each Y coordinate. If the value of Y lies within the range of the control points of the Bezier curve, interpolation is used to find the corresponding X coordinate. Otherwise, X is set to the IML. A genetic algorithm is used for the search.

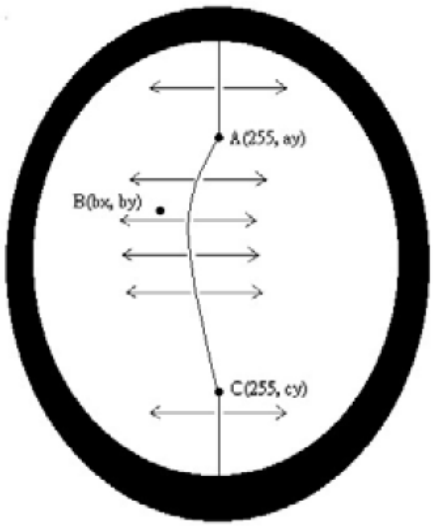

Figure 3.1: The symmetry model: the midline shift is defined as a quadratic Bezier curve. [Liao06]

The algorithm finds automatically the midline shift successfully in a number of brain CT images (experimental results are shown in Chapter 6 Section 6.2.1), which

was not reported before. It makes use of the brain symmetrical structure rather than attempting to extract the midline using conventional segmentation algorithm used on other brain tissues.

However, the method fails in brain CT images of patients with single large spontaneous ICH around center of the brain. In contrast to the good results where hemorrhages often appear on the surface of the brain, spontaneous ICH often occurs around the IML. This is the case in which overall symmetry is destroyed. The algorithm fails on such case because the model assumes the symmetry exists despite of lesions (Figure 3.2).

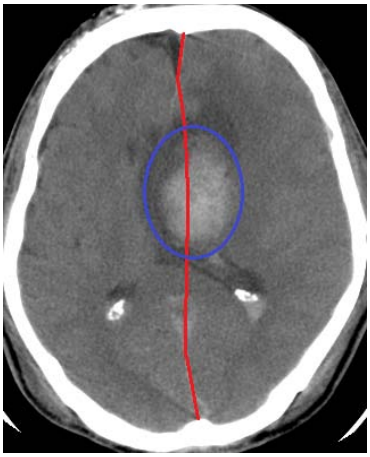

Figure 3.2. Large ICH around the IML

Besides, the algorithm is developed solely on single 2D slice. It requires expert to manually go through each 2D slice and select certain slice with expected pathological information. Thus it is not fully automatic.

High computational cost comes from the exhaustive search of the control points of the Bezier curve. (A running time comparison is shown in Chapter 6, Section 6.2.1) This makes the method not practical to be used in real-time retrieval tasks.

3.1.2 The Ventricle Shape Matching Model

The ventricle shape matching model is proposed by Chen et al. [Chen10] to compute the deformation field of ventricle contours across CT images, which is an extension of their ventricle segmentation work in 2009 [Chen09]. The segmented ventricles are matched to the ventricle shape template to get the deformed vector fields around the ventricles (Figure 3.3). Finally the midline is deformed according to the deformation vector fields.

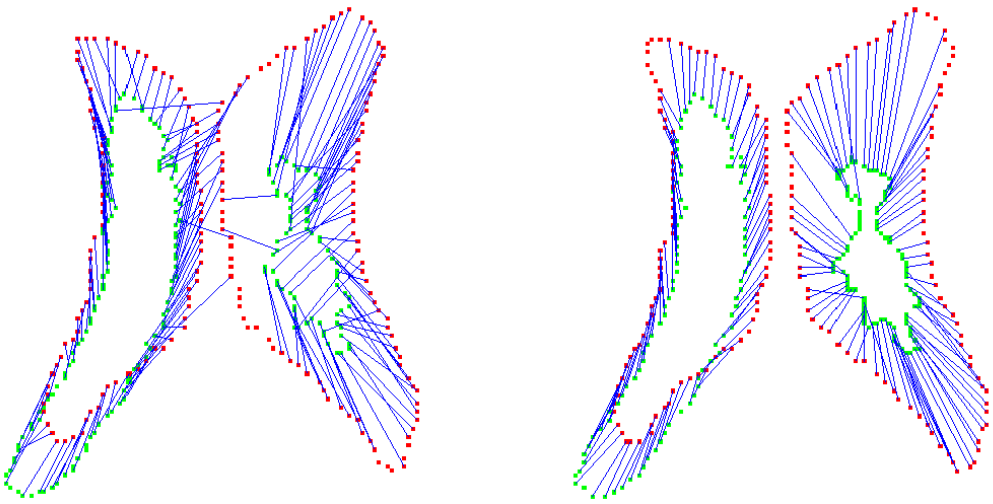

Figure 3.3. The shape matching of ventricles.

Chen uses “success rate” to evaluate the algorithm performance. The success rate is similar with “recall” or “sensitivity” which describes the ability of the algorithm to successfully identify the positive cases. Chen’s method effectively traces the

deformed midline with success rate 87.9% on patients presenting 5mm midline shift with 2.25mm tolerance.

However, the method fails on large brain deformation cases where ventricles are compressed or absent on the image. Specifically, in the case of brain herniation [Barr07], the 3rd ventricle disappears on the image (Figure 3.4). The method will wrongly segment the ventricle at right side of the image as the 3rd ventricle, thus the midline is wrongly deformed.

Figure 3.4. The missing of the 3rd ventricle.

3.2 Work on Detection of Attachments of Falces

Several algorithms have been proposed to address the problem of detection of attachments of falces. Liu et al. [Liu97] compute the two points in order to calculate the ideal midline. They measure the symmetry of the skull by rotating the entire scan series from -45 to +45 degrees with a 0.5-degree step. The symmetry is measured by the difference of pixel intensities between the left and right half of the skull. The rotation angle yields the smallest difference (most symmetrical) is chosen to rotate the entire scan. The center line of the bounding box of the skull is then the straight line

where the IML is located. Points ***A*** and ***B*** are thus the intersection points of the IML and the inner contour of the skull. It is time consuming because it operates on the entire series of scans.

Liao et al. [Liao06] define the two centers of the attachments of the falx to be the points along the inner contour where the skull is thickest. This is an invalid assumption. For example, from Figure 5.2, we see that on the upper left part of the skull, around -30 degrees, the skull is thicker than the part where ***A*** is located.

Both proposed algorithms fail to capture the features of the centers of attachments of the falces, which are protuberances along the skull inner contour. Therefore, we propose an algorithm based on the extractions of the protuberance points. (Please refer to Chapter 5 Section 5.2.1 for algorithm details)

3.3 Work on Ventricle Segmentation

Many studies have been carried out on brain ventricle segmentation. However, most of the methods focus on MR brain images rather than CT images. Typical ventricle segmentation methods in MR brain images include the thresholding methods [Worth98], region growing methods [Sonka96] [Schnack01] [Xia04] [Liu.Jm09], knowledge based methods [Xia04] [Liu.Jm09], data clustering approach [Pham00], model based methods such as atlas warping [Holden10], shape deformation [Baillard00] [Kaus01] [Shen01], and hybrid approaches [Liu.Jm07] [Liu.Jm08]. As remarked by [Lauric97] [Liu.Jm10], there is very limited on ventricle segmentations on brain CT images. This is because of the following difficulties. Firstly, the CT

images contain much more noise than MR images and also have much lower contrast. As introduced in Chapter 1, Section 1.2.1, the intensity of brain tissues are hard to separate from each other. Secondly, anatomic variations in the shape and size of the ventricles are quite large [Liu.Jm10]. Thirdly, random traumatic brain injuries bring arbitrary distortions of the brain. Thus the ventricles are arbitrarily deformed. This gives rise to problems in designing a similarity function or probabilistic atlas to segment the ventricles. Due to these difficulties, it is hard to apply the segmentation techniques of MR images directly on CT images [Liu.Jm10]. We review five major approaches for brain CT image segmentation: (a) the active contour approach, (b) the threshold and region growing approach, (c) the knowledge based approach, (d) the data clustering approach, and (e) the hybrid approach.

3.3.1 The active contour approach

The first active contour model, also called “snake”, was initially proposed by Kass et al. [Kass88]. The idea is to model the image as a 2D function mapping the positions to the intensities and model the contours as peak or trough, which corresponds to the local maxima or minima of the function. An active contour, called the “snake”, is initialized near the contours and tries to minimize the energy of the function moving towards the peak or trough. Xu et al. improved the snake and proposed an improved model, the “Gradient Vector Flow (GVF)” [Xu97] [Xu98] in 1997. It adds a momentum to avoid the snake being trapped into local maxima or minima. Snakes are widely applied on image segmentation tasks. Maksimovic et al. use snakes to segment brain tissues and do 3D reconstructions [Maksimovic00].

Snakes are widely used in human tissue segmentation in medical imaging. However, their use is not fully automatic because it requires manual input to initialize the snake's shape and location. Moreover, snakes are computed by iteratively finding the local minima and maxima of a complex energy function. This process can be very time consuming. In our problem, we need the algorithm to be fully automatic and efficient to (a) be embedded into the system as an intermediate step, and (b) support online queries. Therefore, the active contour approach is generally not proper in our case.

3.3.2 The threshold and region growing approach

The idea of the threshold and region growing method is straightforward. It uses thresholds on the image intensities to group pixels with similar gray levels. It then uses region growing to further group pixels with spatial constrains. Deleo et al. [Deleo85] can be considered as the first attempt to segment tissues from CT images. They use hard threshold to separate skull, brain matters, and CSF regions. Obviously, the hard threshold is not robust to handle the various cases. Therefore various methods have been proposed to make the threshold dynamic and adaptive. Ruttimann et al. [Ruttimann93] propose an automated thresholding method to segment brain cerebrospinal fluid (CSF). The threshold is obtained from the statistics of the intensity histogram. Hu et al. [Hu05] propose a method based on double thresholding and brain mask propagation. A reference image from atlas with skull removed is chosen as the brain mask. Then a high threshold is determined by fuzzy C-means clustering on the mask. A low threshold is determined from the statistics of the intensity histogram of

the mask. The thresholding and region growing method is efficient. However, all the work is proposed on normal scans. The methods are hard to be applied on cases of severe trauma, where the ventricles are largely deformed. Therefore, they are not applicable on our severe traumatic brain injury cases.

3.3.3 The knowledge-based approach

The knowledge-based approach uses expert knowledge to describe ventricles anatomical property, such as the position, shape, and color. Li et al. [Li95] designs a generic blackboard system to organize tissue location information. The system loads a raw image and breaks the images into low level features, such as points, lines, and regions, so that each image contains multiple tissues and each tissue comprises multiple points, lines and regions. The tissues are then recognized based on the combination of the low level features according to rules. The knowledge-based approach is too complicated to be embedded in the TBI CT image analysis algorithms as an intermediate step, especially real-time online framework such as a TBI CT image retrieval system. The complexity of the algorithm comes from the complexity of knowledge representation and large amount of features used. Moreover, the knowledge is not able to predict the arbitrary distortion of the brain. Hence it is not applicable on severe trauma cases.

3.3.4 The data clustering approach

An image can be viewed as a collection of pixels. The ultimate goal is to classify each pixel into groups, i.e. segmenting regions. The first such algorithm was proposed

by Loncaric et al. [Loncaric97]. They use K-mean clustering and neural network to classify the pixels. Another typical work on ventricle segmentation using data clustering approach was proposed by Chen et al. [Chen09]. They first segment all types of tissues using a Gaussian mixture model (GMM) [Greenspan06]. Then template matching is used to detect the ventricle regions. The main drawback of the data clustering methods is the problem of initialization. The method is sensitive to the initial input of the clustering model. For example, K-mean requires the user to input initial cluster centers, and GMM requires the user to predefine the number of clusters before processing. Therefore, pre-processing and post-processing are normally required in clustering. For example, Loncaric [Loncaric97] use rule-based labeling after the ventricle segmentation. In this approach, both approaches do not handle large brain distortion. This limitation of Loncaric's work [Loncaric97] comes from using rule-based labeling, where the rules are constructed using knowledge on standard CT scans. The limitation of Chen's work [Chen09] comes from the template they use, which is generated from normal MR scans. The clustering approach is applicable to our case but requires robust post-processing to handle the severe brain distortions.

3.3.5 The hybrid approach

Recently, Liu et al. [Liu.Jm10] proposed a hybrid approach using domain knowledge on the anatomy, shape variation, and intensity distribution of the ventricles in brain CT images for ventricle segmentation. This is the first work for automatic segmentation of the ventricular system from CT scans [Liu.Jm10]. The system is not only able to segment ventricles from a single CT slice, but also from the entire brain

volume. In their method, a region of interest (ROI) is firstly identified through CSF thresholding. Ventricles inside the ROI are then segmented using shape-template matching. The method is automatic and robust. It gives best performance on brain ventricle segmentation on CT images presently [Liu.Jm10]. However, this work is not applicable to our case. This is due to the following two reasons. Firstly, the work uses a model-based method. It is important to make sure the model contour of the ventricle falls near the corresponding ventricle region, so that the related ventricle is covered in the ROI after contour expansion. An expansion parameter, *d*, is empirically set to 6mm. But in order to deal with large deformation, one may need a larger value of *d*. That will make the ROI include more non-ventricle region and decrease the ventricle segmentation performance. On the other hand, in our case, the significant midline shift is defined as larger than 5mm, and most cases have midline shift around 1cm or even larger. Recall that the midline shifts together with the ventricles. This means that in our case, the ventricle distortion is generally around or larger than 1cm. Therefore, using the same settings of the algorithm, [Liu.Jm10] is unable to find the correct contour of largely deformed ventricles (Figure 3.5). Secondly, this method is too complicated and time consuming to apply as an intermediate step of our model. According to the report, it takes 10 seconds to segment ventricles of one patient, while our proposed ventricle candidate segmentation method takes less than 3 seconds for each patient as shown in later sections. Thirdly, the goal of [Liu.Jm10] is different from ours. Theirs is the first work to automatically segment the ventricular system from CT images. On the other hand, ours is to find ventricle candidate regions instead

of segmenting the exact ventricle region. This allows for more tolerance to large deformation cases.

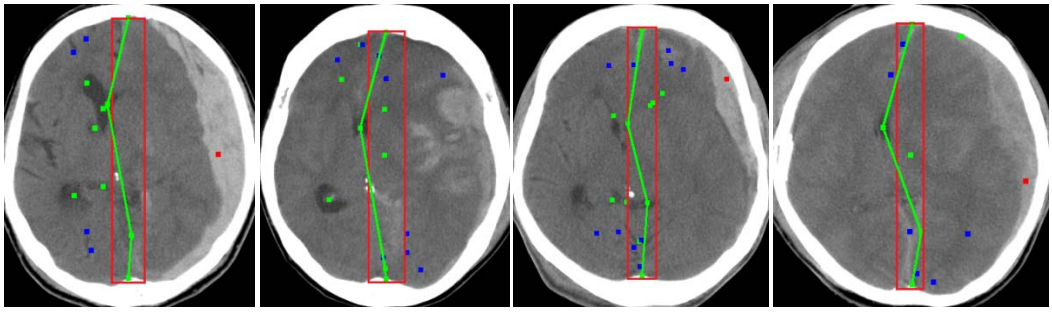

Figure 3.5. The large ventricle distortion. The green line is the midline traced by our proposed algorithm. The red box is the expanding range of 6mm of Liu's method. We can see the frontal horns are largely displaced and out of the range.

In conclusion, current ventricle segmentation methods from brain CT images suffer from at least one problem which makes them not directly applicable as an intermediate step in our model. The problems are: (a) not fully automatic; (b) not robust to handle large brain distortion. Moreover, in our case, it is not necessary to exactly segment the frontal horn and the third ventricles. As introduced in the following sections, rough segmentation with multiple candidates output is enough. The candidates are further selected in the marker selection step.

3.4 Summary of the Chapter

This chapter reviewed current works on brain midline shift detection algorithms and also works related to the intermediate steps. Based on the literature review, there are current only two methods proposed on the midline shift detection algorithms. Both of them suffered at least one of following problems: (a) not fully automatic; (b) time consuming; (c) unable to handle unsymmetrical cases; (d) unable to handle cases with

missing ventricles. Therefore, in order to solve these problems and fulfill the research gap, we propose a novel midline shift quantification and measurement method in this thesis.

There are many approaches proposed on ventricle segmentations. However, current proposed techniques are either not fully automatic or not robust to handle large brain distortion. Therefore, in order to solve our problem, we propose a fully-automatic and robust method to roughly segment the ventricles using GMM and candidates selection algorithm. Details of the proposed methods are discussed in Chapter 5.

Chapter 4

PREPROCESSING

In this chapter, the preprocessing step of the proposed algorithm will be introduced. The preprocessing step takes the input, which is a series of brain CT scans from a single patient, and outputs the Middle Slice (MS), the probability map of ventricles (PMV), the bone map, the blood map, and the cerebrospinal fluid (CSF) map. Specifically, the preprocessing module has two components, the encephalic region separation and the MS detection.

4.1 The Encephalic Region Separation and Intensity Maps

The purpose of the separation of the encephalic region is to focus the analysis on the encephalic region, because clinical brain trauma diagnoses focus on this region. After the separation, the CT images are grouped into two groups. Referring to Chapter 2, Section 2.2.1, the encephalic region contains images from levels 3 to 5; the non-encephalic region contain images of the nasal cavity (level 1 and 2) and the top of the brain (level 6). The separation is done by employing wavelet transform (WT) and

texture analysis techniques. We introduce the basics of WT first, and then we show our algorithm of separation.

4.1.1 Wavelet transform

The Wavelet transform (WT) has been widely applied in image processing, especially texture analysis. The following introduces the basics of the WT.

In signal processing, one signal has two types of descriptions, in the time domain and in the frequency domain. Signals are expressed in the time domain in their raw format: the signal is measured as a function of time. However, this way of representing signals does not make explicit frequency information, i.e., the rate of the signal varying. Therefore, frequency domain representation of signal was born. The frequency spectrum captures how signal changes.

The Fourier transform (FT) effectively transforms a signal from its time domain representation to the frequency one and vice versa. This is achieved by expressing the signal as (possibly infinite) linear combinations of parametric basis functions. For example, if a signal is so regular that it is able to be expressed by only single function component after it is transformed from time domain to frequency spectrum, its frequency spectrum will be a single pulse. This means that it changes regularly with constant frequency. On the other hand, if a signal is so irregular that it is expressed as endless function components after the transformation, its frequency spectrum will

contain complicated and countless pulses showing that it changes irregularly with various frequencies.

The WT applies the same idea as the Fourier transform: it provides a time-frequency transformation. Moreover, it is capable to represent time and frequency information simultaneously. This makes it superior to the FT. By WT, a time-domain signal is decomposed into a high frequency component and a low frequency component. Each component can be decomposed further. Thus we can use WT to split one signal into different frequencies and still preserve its temporal information.

An image is a 2D signal. Using WT, we get high frequency components of the image and low frequency components. The high frequency components capture the textures. The low frequency components are quantized image where they contain major contents with pixels values down sampled.

More details of WT and its time frequency representation and property can be found in [Mallat89] and [Chui92].

4.1.2 The separation algorithm

From Section 2.2.1 we know that the texture of nasal cavity region is much more complex than that of the brain region. Texture is a good feature to distinguish them. The WT is able to separate textures and the homogeneous intensity field of the image. [Liu.R.ICPR08] Hence, we can describe the texture of the CT images using the coefficients of the high frequency components of the wavelet transform.

The first step is to decompose the image four times using the simplest wavelet - Haar wavelet transforms [Haar10] and then reconstruct the signal by only using the detail coefficients and obtain a texture map (Figure 4.1).

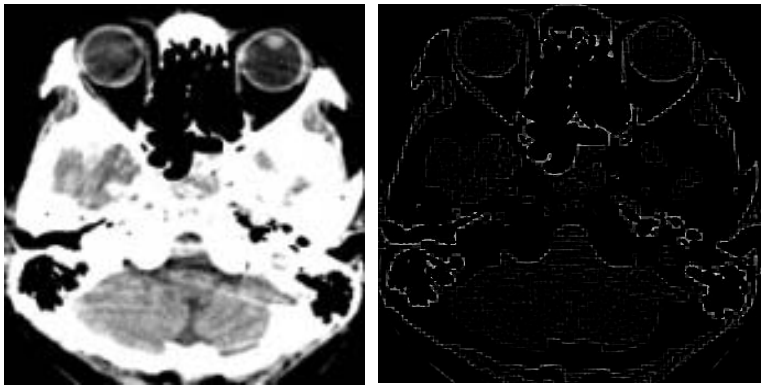

Figure 4.1. Left: Brain CT Image. Right: Texture map.

Secondly, we calculate the histogram of the intensity distribution, and record 4 measurements: (a) the arithmetic mean, (b) the standard deviation, the skewness and the kurtosis [Kenney62] of the distribution.

Thirdly, we employ a variation of Haralick's model of texture descriptors [Haralick73] and add features vector such as entropy, energy, contrast, homogeneity, variance, maximum probability and the correlation. (Refer Equation 4.1 – 4.9) Mathematically, given a size of *M* by *N* image *I (i, j)* and denoting μ to be the mean and *ó* to be the variance of the intensities, those information are captured in (Equation 4.1 - 4.9) below.

$$Entropy = -\sum_{i}^{M}\sum_{j}^{N} I(i,j)\log\big(I(i,j)\big) \tag{4.1}$$

$$Energy = \sum_{i}^{M}\sum_{j}^{N} I^2(i,j) \tag{4.2}$$

$$Contrast = \sum_{i}^{M}\sum_{j}^{N} (i-j)^2 I(i,j) \tag{4.3}$$

$$Homogeneity = \sum_{i}^{M}\sum_{j}^{N} \frac{I(i,j)}{1+|i-j|} \tag{4.4}$$

$$Variance = \frac{1}{2}\sum_{i}^{M}\sum_{j}^{N} \left((i-\mu)^2 I(i,j) + (j-\mu)^2 I(i,j)\right) \tag{4.5}$$

$$Maximum = \max_{i,j} I(i,j) \tag{4.6}$$

$$Inverse\ Different\ Moment = \sum_{i}^{M}\sum_{j}^{N} \frac{I(i,j)}{|i-j|^k} \tag{4.7}$$

$$Cluster\ Tendency = \sum_{i}^{M}\sum_{j}^{N} (i+j-2\mu)^k I(i,j) \tag{4.8}$$

$$Correlation = \sum_{i}^{M}\sum_{j}^{N} \frac{(i-\mu)(j-\mu)I(i,j)}{\sigma^2} \tag{4.9}$$

Lastly, we use SVM with a linear kernel to learn the model.

4.1.3 The experimental result: Separation

The encephalic region separation is evaluated from a dataset consisting of 493 patients, totally 11011 images. Each patient has 20 to 30 slices. Moreover, not all slices follow a sequential order. Different patients have different scanning starting or ending positions, and different scanning angles.

The algorithm is implemented on a PC with 2.33 GHz Pentium 4 CPU using MATLAB. The average runtime per image is 0.26s. The ground truth is marked by

professional doctors. Using ten-fold cross validation, the recall is 89.48% and the precision is 96.27%.

This work[1] effectively separates the nasal cavity slices and the encephalic slices. The separation can be further used in the brain indexing task.

4.1.4 The intensity maps

Medical images contain valuable anatomical information. The regions of different appearance represent different tissues. To detect anatomical features in TBI CT images, we firstly do a rough segmentation of different tissue regions based on intensities. The regions are skulls, hemorrhage regions, brain matters and CSF. Because the intensity values are densely distributed (Figure 4.2a), it is hard to segment the regions with hard thresholds. However, the low frequency components obtained in the previous steps from wavelet decomposition have discretized intensity levels (Figure 4.2b). This is because that the wavelet effectively captures the majority intensities and eliminates the heterogeneous components.

[1] The work is published in [Liu.R.ICPR.08].

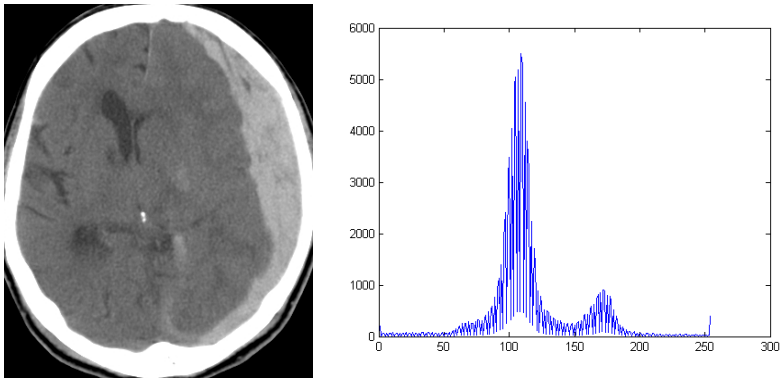

a

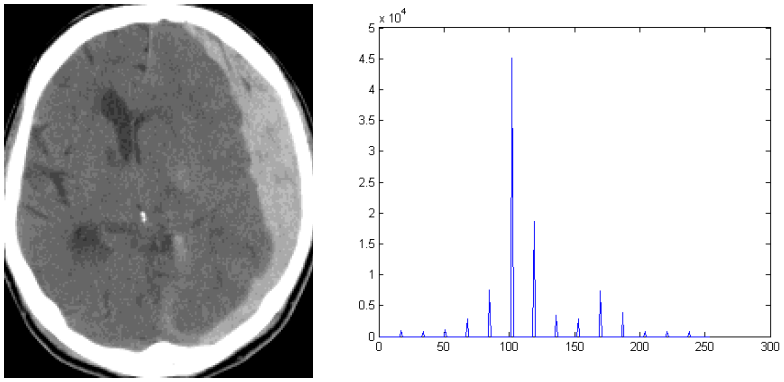

b

Figure 4.2. Brain regions segmentation. a: left: original image, right: the continuous intensity histogram; b: left: image reconstructed using the approximate coefficients, right: the discretized histogram.

Then thresholds are made on the discretized images to get the bone map (skull image), CSF map (CSF image), and blood map (hemorrhage image) respectively (Figure 4.3).

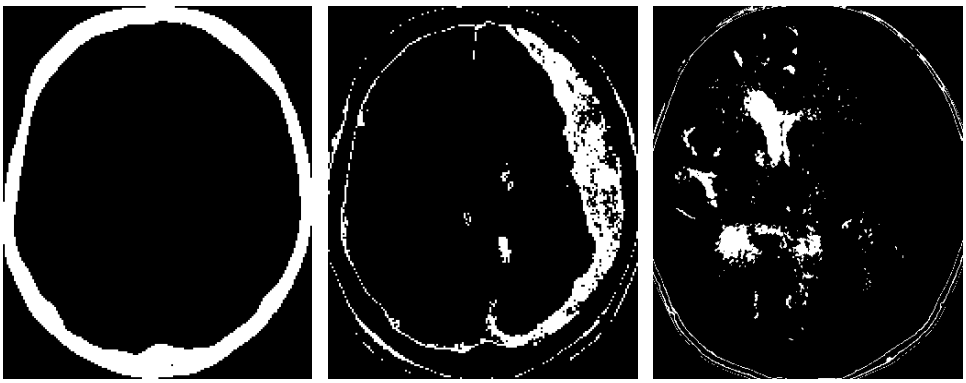

Figure 4.3. Results of tissue region segmentation using wavelet method: Left: Skull; Middle: CSF; Right: Blood.

4.2 Middle Slice Detection

The input is an entire series of one patient's CT scans. Clinically, the midline shift occurs at height level 4. One good representative slice among all level 4 slices is the Middle Slice (MS) because it contains all markers of the brain midline shift, the centers of attachments of falx, the frontal horn, and the third ventricle. Therefore, we shall pick the MS out of the entire scan, and detect and quantify the midline shift based on the MS.

The MS is determined by examining two features: the size of the bounding box of the skull and the probability of the slice contains frontal horn and lateral ventricle.

The bounding box of the skull is computed from the bone map separated from the previous step. The size of the bounding box of the skull is then the multiplication of the skull height with the skull width.

To compute the probability of the slice containing frontal horn and lateral ventricle, we build a posterior probability map of ventricle (PMV) (Figure 4.4). The PMV is the average image with frontal horns and lateral ventricles manually labeled. Totally 100 images are manually selected to be labeled so that they include various MLS cases. The label images are binary images where the labeled regions have pixel value one and other places zero. The map is constructed by adding all labeled images and normalize the summed image so that its pixel values are all from zero to one. Therefore, the brighter regions of the probability map indicate higher numbers of images with ventricles in the regions and thus higher probability that ventricles are

present. Then we compute the similarity of the PMV and the CSF map of current slice using (Equation 4.10). Note that the more similar the CSF map to the PMV, the higher similar score obtained, thus the higher chance the slice contains the frontal horn and the third ventricle.

$$\text{Similarity} = \sum_{x,y \in \text{MS}} \text{CSF}(x,y)\text{PMV}(x,y) \tag{4.10}$$

Figure 4.4. The probability map of ventricle.

Finally, the size of the bounding box, denoted as *S*, and the convolution score, denoted as *p*, through all slices, are normalized between 0 and 1. The MS is thus the slice has largest value of $S + wp$ within the encephalic region, where *w* is a weighting factor and is set to 9 empirically.

4.3 Summary of the Chapter

This chapter introduced the preprocessing step of the proposed midline shift quantification algorithm. The preprocessing step is the first step of the proposed algorithm. It takes raw input images, extracts the encephalic slices, and outputs the images and maps used for the main part of the algorithm. Specifically, the input of the

preprocessing step is the entire series of one patient's brain CT scans. The outputs are the bone map, the CSF map, the blood map, the probability map, and the middle slice.

Chapter 5

THE BRAIN MIDLINE SHIFT QUANTIFICATION

The preprocessing step outputs the middle slice (MS) and several maps. The MS is then input to the main part of the proposed algorithm. In this chapter, we firstly introduce the proposed anatomical marker model (AMM). Then we present the main algorithm based on this model. Specifically, the algorithm contains two parts, the marker candidate detection and the marker candidate selection.

5.1 The Anatomical Marker Model

Recall that no matter how large the midline shift is, it always passes through the centers of attachments of the falces (Figure 5.1), and certain anatomical landmarks, which are the "*midline shift markers*". Hence to trace a deformed midline (DML), it is crucial to locate those midline shift markers.

Based on this observation, we propose AMM for tracing the DML on the MS.

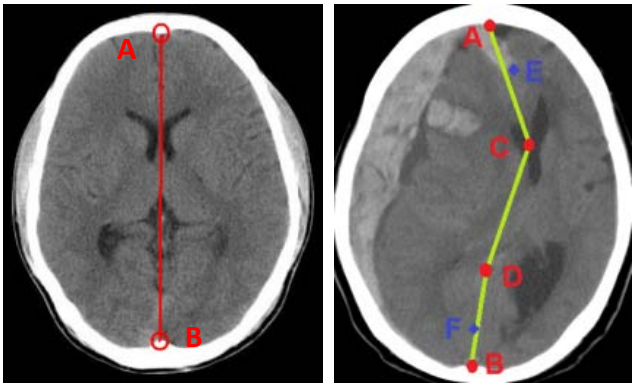

a *b*

Figure 5.1. The anatomical marker model. *a*: the IML; *b*: the DML and markers.

Refer to Figure 5.1. We define the two *centers of attachments of falces* to be ***A, B***. Thus the ideal midline (IML) is the line segments ***AB***. In case of DML, we define the center of the *frontal horn*[1] to be ***C***. Define the center of the *third ventricle*[1] to be ***D***. DML in this level is then defined as the polyline ***A-C-D-B*** (Figure 5.1b). Moreover, the frontal falx starts at point ***A*** and ends at point ***E***. The lateral falx starts at points ***B*** and ends at point ***F*** (Figure 5.1b). Points ***E*** and ***F*** are used as auxiliary points for deciding locations of ***C*** and ***D***. We shall see the usages of these two auxiliary points in detail in Section 5.3.4. Therefore, to trace the midline, the problem is to accurately locate those markers ***A*** to ***F***.

5.2 Marker Candidate Detection

To make the marker detection robust, we first detect the marker candidates using various segmentation algorithms. Then we select the correct candidates based on the spatial constrains. In this section three algorithms are proposed to get markers and

[1] Please refer to Section 2.2.1 “Anatomical Structure” Figure 2.5, level 4.

marker candidates. Specifically, the markers ***A*** and ***B*** are obtained from skull analysis. The marker candidates ***C*** and ***D*** are computed from possible ventricular region detection. The candidates for auxiliary markers ***E*** and ***F*** are calculated from falx extraction. In addition, hemorrhages are segmented for the selection process later.

5.2.1 Detection of attachments of falces (markers A and B)

The markers ***A*** and ***B*** are the centers of the attachments of the falces :(a) The central protuberance point in the upper skull boundary, denoted as ***A***. (b) The central protuberance point in the lower skull boundary, denoted as ***B***.

To locate the protuberance, we trace the inner skull boundary contour and find the sharpest turning point (point with the biggest curvature) along the contour. The skull profile is obtained from the bone map in preprocessing step. We then do an exhaustive search to find the point with maximum curvature in the upper (for point ***A***) or lower (for point ***B***) part on the inner skull boundary. We do not need to search the entire boundary as the protuberances are always located around the most upper and most lower parts of the skull in the image. Thus, the search is limited to a -30 to +30 degrees sector scan with a 0.5-degree step along the lower or upper parts of the inner skull boundary (Figure 5.2 Left). Curvature here is computed as magnitude of the change of edge geometrical gradient (Figure 5.2 Right). To deal with the discrete problem, five neighboring points is used to compute the gradient.

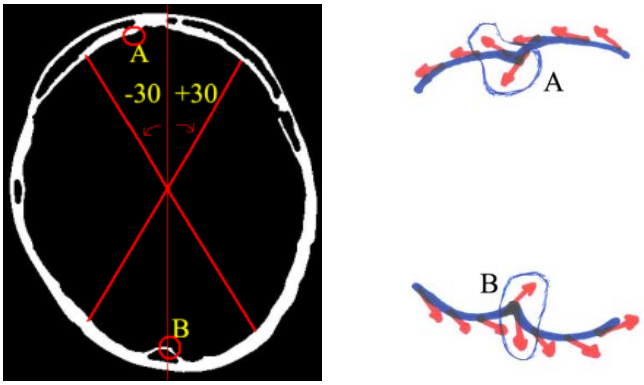

Figure 5.2. Protuberance points detection. Left: Sector scan search for point A and B; Right: change of the Gradient around point A, B.

The detection is evaluated in Chapter 7 section 7.1.2.

5.2.2 Detection of ventricles (markers C and D)

Markers ***C*** and ***D*** are the centers of the frontal horn and the third ventricle respectively. Referring to Figure 5.3 below, the frontal horn (marker ***C***) is located at the upper half of the brain, and the 3rd ventricle (marker ***D***) at the lower half of the brain. Matter inside the ventricles is CSF. It appears as dark regions in the brain CT images, and it is modeled as regions with low intensity values. Note that some low intensity regions may not be ventricles but chronic hematomas or large fissures. They must be pruned. The challenge of this task comes from the following aspects. Firstly, CT images are low contrast and contain much noise. Secondly, for the midline shift cases, the brain is normally largely distorted. Thus the ventricles are arbitrarily deformed to a great extent. Therefore, it is hard to segment the ventricle using standard model-driven methods.

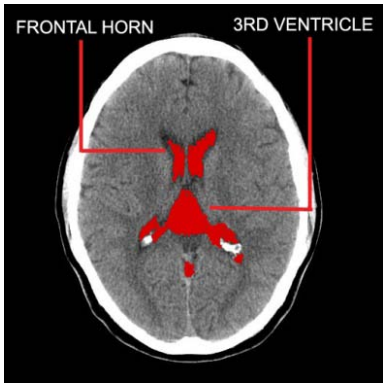

Figure 5.3. Brain ventricle.

We propose a ventricle candidate segmentation algorithm using Gaussian mixture models (GMM) with spatial feature learning. Instead of segmenting the exact ventricle, the algorithm identifies possible ventricle regions. One advantage of using GMM to segment ventricles is that the method is fully automatic and does not need the user to provide the starting points, unlike the active contour model. Therefore, one GMM model is used as an intermediate step.

Generally, GMM assumes the entire image is a mixed Gaussian distribution of pixel data. Each data point has 3 dimensions [x, y, i], where x and y are image coordinates and i is the intensity value. The parameters of the mixed distribution are learnt through EM algorithm [Dempster77]. Mathematically, suppose the mixed distribution is $\boldsymbol{D}$, then $\boldsymbol{D}$ is composed of multiple Gaussians $\boldsymbol{G}_j$ with different weights w_j:

$$D = \sum_j w_j G_j(x, y, i) \tag{5.1}$$

Each pixel data **p** has probability p_j under every Gaussian $\boldsymbol{G}_j$. We say that pixel **p** belongs to Gaussian $\boldsymbol{G}_j$ if its probability p_j under $\boldsymbol{G}_j$ is the maximum among all Gaussians. In this way, if we have n Gaussians, all pixels are able to be classified into n class where each class is a Gaussian distribution. In our case, we set number of Gaussians to be 6 empirically so that expected clusters are: one cluster for the frontal horn, one cluster for the third ventricle, one cluster for the possible blood regions, one cluster for the possible other CSF regions, and two clusters handling noise.

The image is firstly smoothed by standard Gaussian filter [Szeliski10]. Then the CSF map is masked on the image so the masked image only contains CSF pixels.

GMM is then applied to the masked image to segment the ventricles. As shown in Figure 5.4, each color represents one group of pixels clustered by GMM.

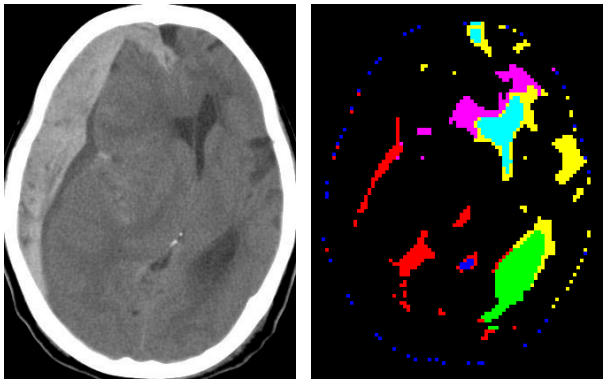

Figure 5.4. The GMM segmentation result.

The segmented regions image contains ventricles and noise regions (Figure 5.5). Our next step is to eliminate noise. The noise regions are typically of two types and pruned by connected component analysis according to the following two rules: (a) Single-pixel regions are considered as piecewise noise. By experiments, regions less

than 16 pixels are pruned; (b) Surrounding regions are regions wrapping around the ventricles. They are considered as noise. They are not ventricles because the ventricles are normally a solid region filled by CSF.

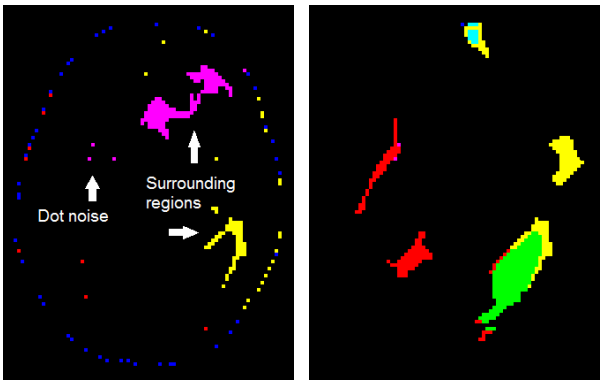

Figure 5.5. Noise region pruning.

They are thus pruned using solidity. Solidity is defined as the ratio of number of pixels over the area of the convex hull [Barber06]. By experiments, regions with solidity less than 0.3 are pruned.

Moreover, the ventricles segmented may not be the lateral ventricle body or frontal horn as we expected. They may be regions of large Sylvain fissures, temporal ventricles or chronic hematomas. Such regions are pruned by employing the PMV. For each segmented regions ***R***, a probability ***p*** of being the frontal horn or the third ventricle is calculated using (Equation 5.2):

$$p = \frac{1}{n}\sum_{x,y\in R} PMV(x,y)\text{sign}\big(R(x,y)\big) \qquad (5.2)$$

where ***n*** is the number of pixels in region ***R***. The sign(x) function returns 1 if x > 0 and 0 otherwise.

Finally, we pick the top five highest probability candidate regions (Figure 5.6 right).

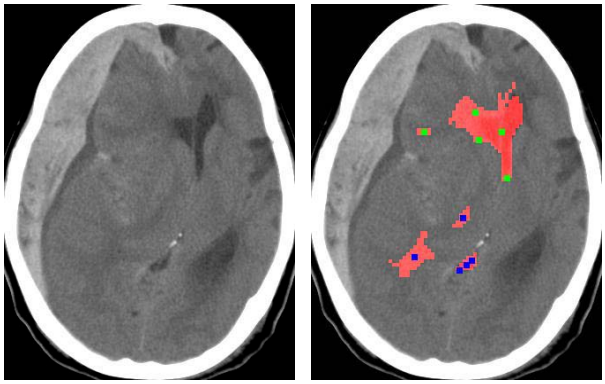

Figure 5.6. The ventricle detection results after convolution.

The purpose of picking multiple candidates is to make the midline shift detection algorithm robust. Because brain injury may unexpectedly deform the brain structure, it is impossible to define the best candidate using hard criteria without incorporating contextual information such as location of other anatomical landmarks. The selection of the best candidate will be introduced in Section 5.3.

The detection is evaluated in Chapter 6, Section 6.1.2.

5.2.3 Detection of auxiliary markers E and F

Markers ***E*** and ***F*** are the two end points of the brain falces. Specifically, ***E*** is the lower end point of the upper falx, and ***F*** is the upper end point of the lower falx. Referring to the six height levels (Figure 2.5), brain falces are present in the height 4^{th} and 5^{th} levels only. There are two falces, the frontal falx and the lateral falx. They are modeled as two straight line segments located at the upper central and lower central

parts of the brain respectively (Figure 5.7). Therefore, the problem of brain falx segmentation is to extract the two line segments from brain CT images. Since falces always shift with the deformed brain midline, successful extraction of the falx will help to trace the deformed midline. The challenge to segment a brain falx comes from its weak appearance in CT scans. As shown in Figure 5.7, left, the falx is hard to visualize. The boundary is not clearly defined and the endpoints of the falx are blurred and faint somewhere in the brain matter. Therefore, a successful falx extraction algorithm should be able to trace the falx in noisy and low contrast images. Moreover, the algorithm should be robust to severe pathological deformation and at the same time efficient, so that it can be applied online. To our best knowledge, there are currently no algorithms to extract brain falces robustly from CT images in the literature.

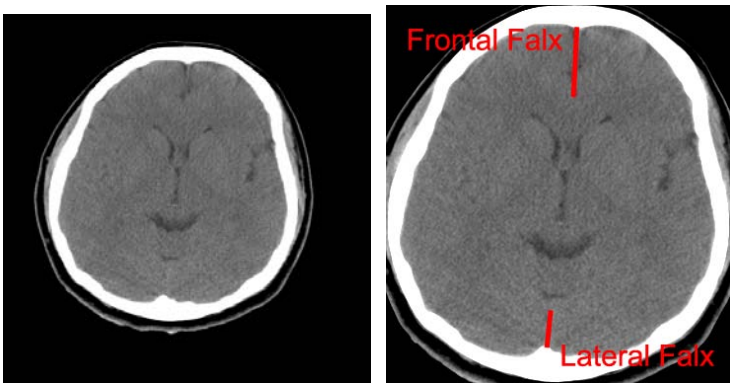

Figure 5.7. The falces. Left: original image; Right: falces marked.

We propose an algorithm that employs vectorization [Ramachandran80] to analyze line segments obtained from the edge map of the image. The vectorization method is known as directional single connected chain (DSCC) [Zheng02]. Section

5.2.3.1 firstly introduces the DSCC model, in section 5.2.3.2 we apply DSCC on the edge map of brain CT image to extract falces. Results will be shown at the end of Section 5.2.3.2.

5.2.3.1 Directional single connected chain

Traditional straight line extraction methods are Hough transformation and vectorization methods [Ramachandran80]. Hough transformation [Duda72] does not require connectivity, unlike the vectorization method. However, because of the difficulty in computing the start and end point of the lines, Hough transformation has a high computational cost. One well-known vectorization algorithm is the directional single connected chain (DSCC) [Zheng02].

DSCC is applied on binary images. DSCC is composed by "run-lengths", and it can be horizontal or vertical. A horizontal (vertical) chain is decided by doing a linear regression of the middle points of its run-lengths, and the line has a slope degree < (≥) $\pi/4$. A horizontal chain contains vertical run-lengths (Figure 5.8(b)) and a vertical chain contains horizontal run-lengths (Figure 5.8(c)).

A vertical run-length is defined as

$$R_i(x_i, ys_i, ye_i) = \{(x,y) | \forall p(x,y) = 1, x = x_i, y \in [ys_i, ye_i] \; and \; p(x_i, ys_i - 1) = p(x_i, ye_i + 1) = 0\} \quad (5.3)$$

where $p(x, y)$ is the intensity of pixel with image coordinates (x, y), 1 is black (foreground), 0 is white (background). This run-length starts from (x_i, ys_i) and ends at (x_i, ye_i). In a horizontal chain C_h, (Figure 5.8(b)) every vertical run-length R_i is arranged in a horizontal sequence, and any two run-lengths, R_i and R_{i+1} connected horizontally. Except for the run-lengths at both ends of the chain, R_l and R_m, any R_i has one and only one run-length R_j connected on each side. For the left side of R_l and the right side of R_m, either there is no run-length or there are more than one run-lengths connected. The connection here refers to 8-neighbour connection. Also, the run-length in the chain should have length within some range. The range is set between half of the average length and twice of the average length. Otherwise, the chain is considered to be broken. The horizontal run-length is defined similarly as the vertical run-length described above. For a horizontal run-length R_i,

$$R_i(y_i, xs_i, xe_i) = \{(x,y)|\forall p(x,y) = 1, y = y_i, x \in [xs_i, xe_i] \; and \; p(xs_i - 1, y_i) = p(xe_i + 1, y_i) = 0\} \quad (5.4)$$

This run-length starts from (xs_i, y_i) and ends at (xe_i, y_i). Similarly, a vertical chain C_v is formed by horizontal run lengths (Figure 5.8(c)).

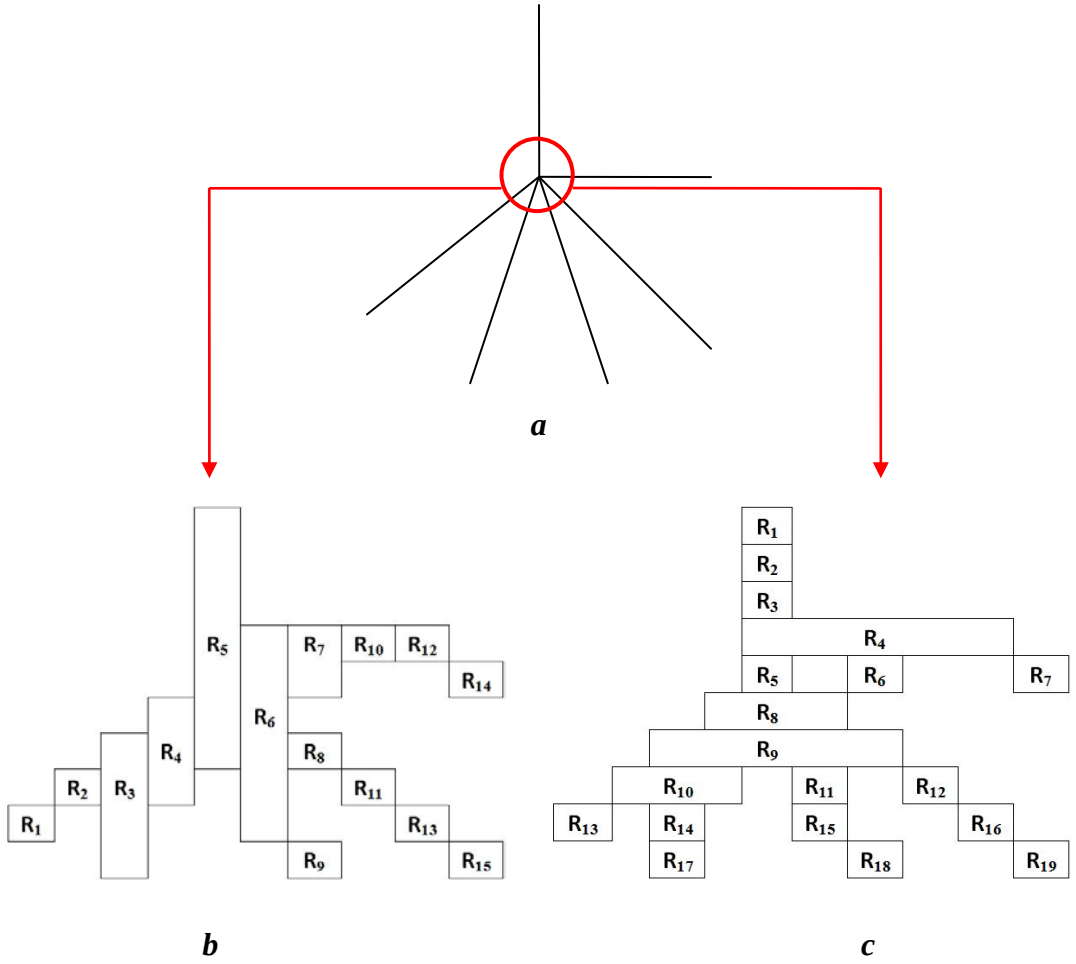

Figure 5.8. The run-lengths and DSCCs. *a*: real lines, ROI: red circled; *b*: enlarged: vertical run-lengths in the circled area in *a*; horizontal chains: C_1={R_1,R_2}; C_2={R_3,R_4}; C_3={R_5,R_6}; C_4={R_7,R_{10},R_{12},R_{14}}; C_5={R_8,R_{11},R_{13},R_{15}}; C_6={R_9}; *c*: enlarged: horizontal run-lengths in the circled area in *a*; vertical chains: C_1={R_1,R_2,R_3}; C_2={R_4}; C_3={R_5}; C_4={R_6}; C_5={R_7}; C_6={R_8,R_9}; C_7={R_{10}}; C_8={R_{11},R_{15},R_{18}}; C_9={R_{12},R_{16},R_{19}}; C_{10}={R_{13}}; C_{11}={R_{14},R_{17}}.

In our early work[2] on document image process, we used DSCC to extract straight lines and curves from scientific charts.

5.2.3.2 Falx extraction using DSCC

In this section, DSCC is applied to segment the falces, both frontal and lateral. Both falces are detected from the edge map of the image.

The image is firstly smoothed by standard Gaussian filter [Szeliski10]. Then the CSF map is masked on the image so the masked image only contains CSF pixels.

Canny edge detector [Canny86] is applied on the filtered image to obtain the edge map firstly (Figure 5.9).

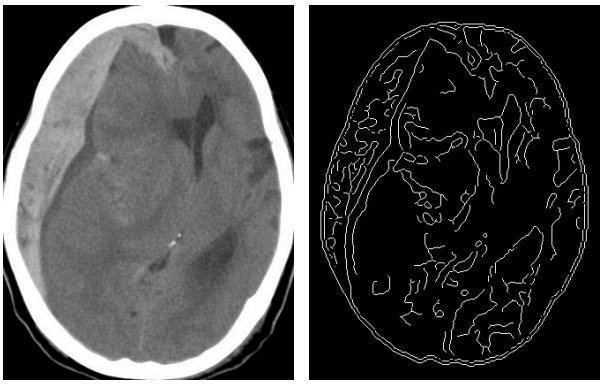

Figure 5.9. Left: The filtered image. Right: The edge map.

The edge map is then smoothed using morphological operators such as open and close [Forsyth02]. The frontal and lateral falces locate at the central part of the upper and lower half of the image respectively. Therefore, to make the computation more

[2] The work has been published in [Liu.R.ICDAR.07].

efficient, we apply an ROI on the image to restrict the falces searching range (Figure 5.10).

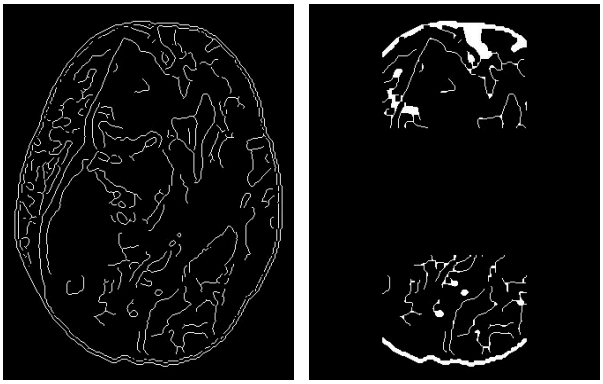

Figure 5.10. Left: The edge map. Right: The ROI of smoothed edge map.

In the windowed edge map, we call each connected component a segment. Falces may contain multiple segments; segments may have irregular shapes; the falx and the skull may be connected together. DSCC is used to solve these problems. We firstly decompose the image into DSCC chains. Then for each chain we fit a straight line segments (Figure 5.11).

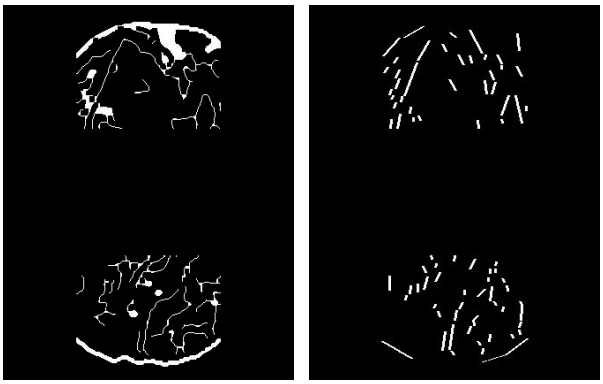

Figure 5.11. The DSCC chains fitted.

We then process the line segments by the following three rules (Figure 5.12): (a) Remove line segments that only have less than five run-lengths as they are very likely

to be piecewise noise; (b) Remove line segments with slope less than 45 degrees as falces tend to be vertical in CT images; (c) Join nearby line segments which have distance less than 20 pixels and with slope difference less than 10 degrees, since they are treated as the same line segment. The numbers in this step are obtained from experiments.

Figure 5.12. DSCC after postprocess.

Finally we pick the top 5 longest line segments with one end point near the skull point ***A*** to be frontal falx candidates. We also pick the top 5 longest line segments with one end near skull point ***B*** to be lateral falx candidates (Figure 5.13). The expected falces are among these candidates. The candidates will be further processed as auxiliary markers in the midline shift detection model introduced in the next chapter. The purpose of picking multiple candidates and selecting the best candidate in the later stage is to improve algorithm robustness. The best candidate will be selected by incorporating the spatial information of other anatomical landmarks. This is the first work to successfully extract the falx from brain CT images.

The detection is evaluated in Chapter 6, Section 6.1.2.

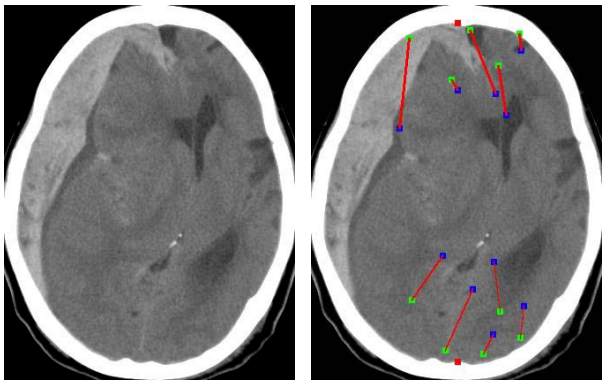

Figure 5.13. Final results of falx extraction. Left: Input image. Right: Output candidates falces (red line segments starting from green points and ending at blue points), Red points are points A and B obtained in Section 5.2.1

5.2.4 Hemorrhage Detection

There is a strong relationship between hemorrhages and the midline. A hemorrhage is useful to select midline marker candidates. Hemorrhage regions are blood clots. The blood clot in acute hemorrhage is relatively fresh. Hence they appear as bright regions in the brain CT images. The blood clot in chronic hemorrhage is relatively aged, and the blood is diluted by CSFs. Hence it appears as dark regions in the brain CT images, which have similar intensity with ventricles. The major difference between the chronic hemorrhage regions and ventricle regions is that ventricles are normally located around certain places as they are anatomical human tissues. However, hemorrhages can occur at any part of the brain. Therefore, it is not proper to use a location probability map to get the hemorrhages. Fortunately, hemorrhages can be identified from their intensities. The acute hemorrhages have unique high intensity values. Although chronic ones have the same intensities as that of the ventricles, they can be handled after the ventricles have been identified.

Here we propose a hemorrhage segmentation algorithm based on background removal. The proposed segmentation algorithm consists of three steps. Step 1 removes the gray and white brain matter. Step 2 uses a wavelet decomposition to reduce noise and sets a threshold automatically to identify the hemorrhage regions. The last step generates a binary image locating the hemorrhage regions.

Algorithm Summary

Input: A CT brain image with skull removed, denoted as T_0 (Figure 5.14).

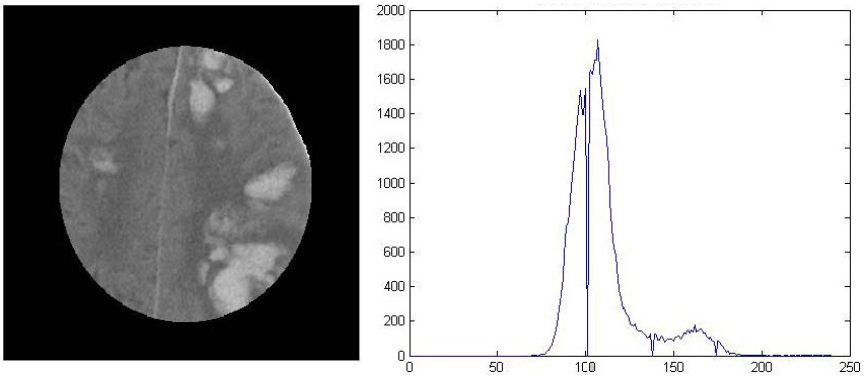

Figure 5.14. Image T_0 – the inner-skull region; left: image; right: intensity histogram. (Horizontal axis: intensity, Vertical axis: number of pixels)

Step 1: Remove the gray and white matter

Most parts of the content inside the skull are the gray and white matter. In the histogram of intensity of T_0, the peaks correspond to the gray and white matter (Figure 5.14). Hence, a simple subtraction of the peak intensity from T_0 will give us an image with the gray and white matter removed. We call the image after the subtraction T_1 (Figure 5.15).

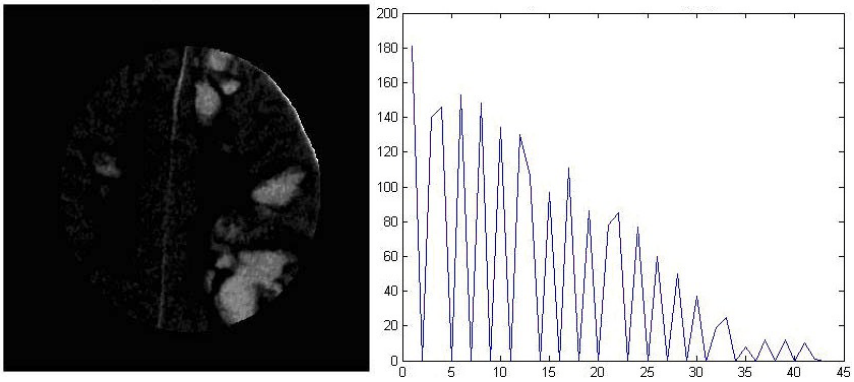

Figure 5.15. Image T_1, gray matter removed; left: the image; right: intensity histogram. (Horizontal axis: intensity, Vertical axis: number of pixels)

Step 3: Reduce noise

From Figure 5.15, left, we can see that there are noise as white dots or tiny fragments in T_1, because we subtract only a single intensity value from various parts of the brain matter. A wavelet noise filter is used to reduce the noise. We finally get the image with noise reduced and more distinguishable hemorrhage regions. We denote the result image T_2 (Figure 5.16).

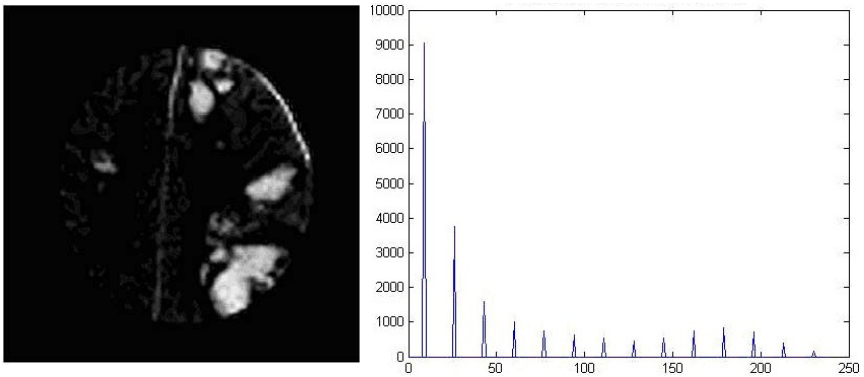

Figure 5.16. Image T_2, noise reduced; left: image; right: intensity histogram. (Horizontal axis: intensity, Vertical axis: number of pixels)

Step 4: Generate a binary image of hemorrhage

After the preprocessing, we can define thresholds according to the intensity distribution of image T_2. We set the hemorrhage threshold to be the value corresponding to the middle of the spikes obtained from the wavelet transform. (Figure 5.16 right) Finally we get a binary image T_3 (Figure 5.17). The largest hemorrhage is picked from the binary image to estimate the hemorrhage effect, for further candidate selection (Refer Section 5.3).

Figure 5.17. Image T_3, each white pixel group represents a possible hemorrhage region of the image.

This work[3] successfully segments the hemorrhage regions. The regions can be used to compute the hemorrhage effect, which is introduced in Chapter 6.

5.3 Marker Candidate Selection

From the previous steps, we have obtained markers ***A*** and ***B***; 5 candidates of markers ***C*** and ***D*** and 5 candidates of auxiliary points ***E*** and ***F***. Note that ***C*** and ***D*** candidates may be absent due to the deformation of certain ventricles. We select these

[3] This work has been published in [Gong.T.PRIB.07] and [Li.S.SPIE.10].

candidates by learning the spatial relationships from ground truth data. The data profile is introduced in Chapter 6, Section 6.1.1.

5.3.1 Pruning the candidates

To make the selection faster and more accurate, we firstly prune the marker candidates according to anatomical and pathological constraints.

Firstly, we apply an ROI on the image to restrict the candidates searching range. The ROI will remove the candidates locating at the most left 1/4 and most right 1/4 parts of the image.

Secondly, recall that the midline shift is due to the pushing behavior of the hemorrhage. If the hemorrhage locates at the left side the candidates of $\boldsymbol{C}$ is expected to be pushed to the right and vice versa. Therefore we prune the candidates of $\boldsymbol{C}$ which locates at the same side of the hemorrhage.

After the pruning step, the candidates of $\boldsymbol{C}$ are restricted to the central half of the image located in the opposite direction of the hemorrhage.

5.3.2 The spatial relationship features

The spatial relationships among the markers are characterized by geometrical. Since a large hemorrhage affects the spatial relationships among the markers, the shape and size of hemorrhage are also included in the spatial relationship features.

Before stepping into the detail of the algorithm, we give an intuitive overview of the spatial relationship features in Figure 5.18 below.

Refer to Figure 5.18, where the hemorrhage lies on the left of the DML. We define the following notations. $\angle BAC$ is the angle formed by line segments AB and AC at point A. $\angle ABD$ is the angle formed by line segments AB and BD at point B. $|AC|$ is the distance from point A to C. $|BD|$ is the distance from point B to D. The hemorrhage ellipse H is an ellipse fitted into the hemorrhage region. Note that the angles and distances are all positive values. We do not consider directions here. The above notation applies also for a mirror image of Figure 5.18 when the hemorrhage lies on the right of the DML.

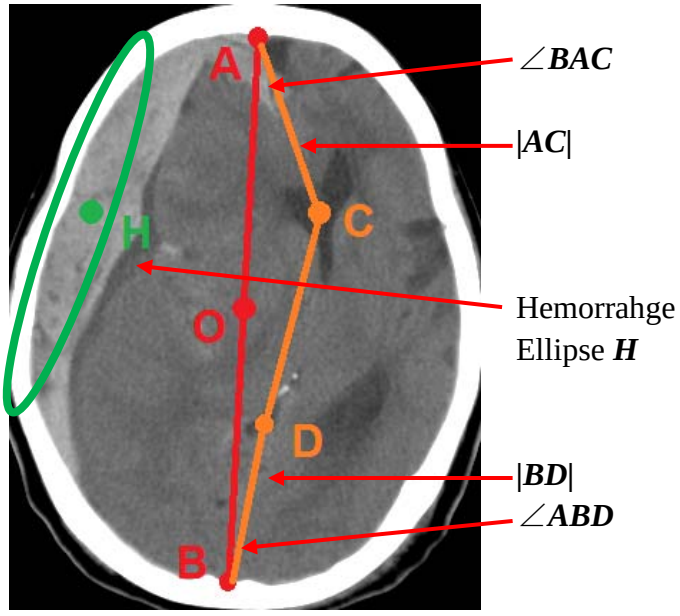

Figure 5.18. Spatial relationships illustration.

Hemorrhages do affect the midline shift. Hence, we should include the effect of hemorrhage to learn the spatial relationships among markers. This effect is mainly a

pushing behavior of the hemorrahge affected by (a) the thickness of the hemorrhage, and (b) the shape of the hemorrhage.

The thickness of the hemorrhage is measured by the length of the minor radius of the ellipse fit on the hemorrhage. The thicker the hemorrhage is, the larger its minor radius is. Therefore, we first fit an ellipse on the contour of the hemorrhage using directed ellipse fitting [Fitzgibbon99]. We then calculate its minor radius and denote it $\boldsymbol{b}$.

The shape of the hemorrhage is expressed by the solidity (defined in Section 5.2.2.2) of the hemorrhage region. This is because hemorrhages are typically of regular shapes: round, cresent, and some shape in between. Note that the radii measured by the ellipse fitting are different from the radii of the raw hemorrhage region where the shape of the hemorrhage is convex. The solidity adjusts this difference. For example, if the hemorrhage is concave, the radii of the ellipse fitted and the radii of the hemorrhage are almost equal. Then the solidity is close to one with no adjustments. On the other hand, if the hemorrhage is convex, the radii of the ellipse fitted will be larger than the radii of the hemorrhage itself. Then the solidity is less than one and has adjustment effect. We denote the solidity $\boldsymbol{s}$.

We combine both measurements to quantify the hemorrhage effect $\boldsymbol{HE}$ using a weighted minor radii length defined by $\boldsymbol{HE = s \cdot b}$.

There are two assumptions for the hemorrhage effect. Firstly, the location of the hemorrhage is not included in the hemorrhage effect. Recall that whether the hemorrhage locates at the left or the right half of the brain is already considered in the pruning step. Therefore, we do not consider the side of the hemorrhage here. According to our hemorrhage effect study which will be discussed in Chapter 7, Section 7.2, the location of the hemorrhage has little effect on the midline shift.

Secondly, as introduced in Chapter 2 Section 2.3, it is extremely rare that there are more than one such large hemorrhage that results in siginificant MLS clinically. Often multiple large hemorrhages result in the death of the. Hence, in case of multiple hemorrhages, only the largest hemorrhage is picked. We assume that the rest can be ignored in the present study.

5.3.3 Learning the spatial relationships among the markers

For all candidates of marker $\boldsymbol{C}$, we want to find the best candidate according to the spatial relationship distribution. Formally, we denote the hemorrhage effect feature with $\boldsymbol{HE}$, the spatial feature of the ith candidate of $\boldsymbol{C}$ to be $\boldsymbol{C_i}$, and the spatial feature of the ith candidate of $\boldsymbol{D}$ to be $\boldsymbol{D_i}$. We would like to find the best candidate among all candidates of $\boldsymbol{C}$ by maximizing the probability p:

$$\boldsymbol{C}_{best} = \arg\max_{0 \le i \le 5} \left(p\left(\boldsymbol{C_i} | \boldsymbol{D}_j, \boldsymbol{HE}\right)\right) \tag{5.5}$$

The probability p is learnt from ground truth data containing 200 partients, total 2479 images. Each image has a feature vector containing 5 parameters:

(a) The spatial feature of point $\boldsymbol{C}$, $\angle \boldsymbol{BAC}$ and $|\boldsymbol{AC}|$.

(b) The spatial feature of point $\boldsymbol{D}$, $\angle \boldsymbol{ABD}$ and $|\boldsymbol{BD}|$.

(c) The hemorrhage effect $\boldsymbol{HE}$.

The joint distribution of the 5 variables of all training data forms an unknown multivariate distribution. We model this distribution as a Gaussian mixture model (GMM).

There is a challenge to the probability learning due to limited volume of data. In clinical practice, there are few patients with significant midline shift than normal or insignificant shift patients (Figure 5.19). There are two problems with the data profile.

Firstly, the data is imbalanced. From the data profile in Figure 5.19, we can see that there are 61% cases with insignificant MLS while MLS in each level is around 9%. The question now is: do we need to rebalance the data sets? The answer is negative because of the following two reasons. Firstly, the data set is randomly selected from the entire population of TBI patients. Thus it reflects the clinical patients' distributions. Rebalancing the data either downsample the majority data, which are insignificant MLS cases, or upsample the minority data, which are siginificant MLS cases by duplication or synthesis [Yin10]. Either way changes the prior probability, such as $p(\boldsymbol{HE})$, $p(|\boldsymbol{AC}|)$, and $p(|\boldsymbol{BD}|)$ used in the Equation (5.7) and (5.9). The distribution then cannot represent the population any more. Because the prior probability in the model is different from the one in the population, the model is ill learnt and problematic to apply clinically. Secondly, rebalancing the data does improve the performance of classifiers [Yin10]. However, our goal is not classification but model the probability distributions of the 5 MLS parameters

modeling spatial relationships. It should be no problem if the true costs and class distributions are known precisely when learning the probability distributions. As remarked by [Provost00], rebalancing is not always applicable or helpful in some machine learning tasks. Our present work is one example. Our data obtained clinically reflects the true distributions of the patients from hospital.

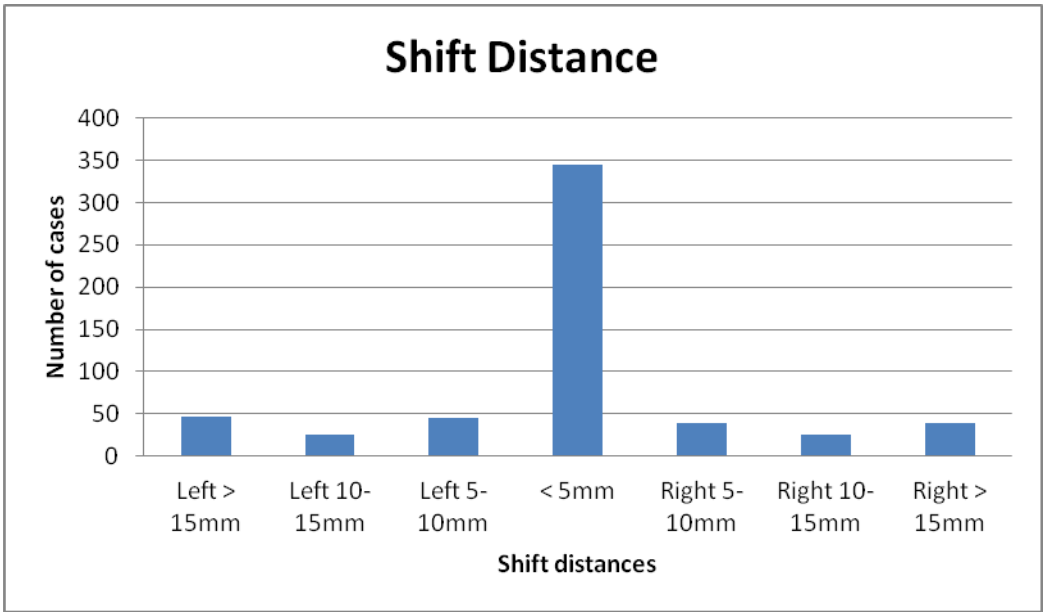

Figure 5.19. Profile of the midline shift distances.

Secondly, the datasize of the significant MLS is small. This will cause overfitting for high dimensional probability models. To avoid the overfitting problem on the limited number of data, we further decompose the joint distribution according to the cause of the midline shift based on anatomical constraints.

1st Anatomical Constrain*: the frontal horn and the third ventricle are deformed by the hemorrhage effect. The effects between the two tissues are neglectable (i.e, Marker* ***C*** *and* ***D*** *are conditionally independent given* ***HE****).*

2nd Anatomical Constrain*: the distance from the frontal horn (or the third ventricle) to the skull propertuberance is only determined by the anatomical structure of the brain. It is independent from the hemorrhage effect (i.e, |**AC**| is independent from **HE**, so is |**BD**|).*

3rd Anatomical Constrain*: The distance of the frontal horn (or the third ventricle)is independent from the angle it deivates from the normal position due to the hemorrhage effect (i.e, ∠**BAC** and |**AC**| are indpendent, so are ∠**ABD** and |**BD**|).*

Based on the 1st constraint, $\boldsymbol{C}$ and $\boldsymbol{D}$ are conditionally independent given $\boldsymbol{HE}$. Therefore, the probability p in Equation (5.5) can be computed by:

$$p(\boldsymbol{C_i}|\boldsymbol{D_j}, \boldsymbol{HE}) = p(\boldsymbol{C_i}|\boldsymbol{HE}) = p(\angle \boldsymbol{BAC}, |\boldsymbol{AC}| \ | \ \boldsymbol{HE}) \tag{5.6}$$

By 2nd constraint, the length |$\boldsymbol{AC}$| is independent from the hemorrhage effect. It is determined by the anatomiacal nature of the brain. By Assumption C, the length |$\boldsymbol{AC}$| is independent from the angle $\angle \boldsymbol{BAC}$. Therefore, the probability Equation (5.6) can be further refined as

$$p(\boldsymbol{C_i}|\boldsymbol{D_j}, \boldsymbol{HE}) = \ p(|\boldsymbol{AC}| \ | \ \boldsymbol{HE}) \times p(\angle \boldsymbol{BAC}|\boldsymbol{HE}) = \frac{p(|\boldsymbol{AC}|) \times p(\angle \boldsymbol{BAC}, \boldsymbol{HE})}{p(\boldsymbol{HE})} \tag{5.7}$$

By decomposition, the dimension of the Equation (5.5), which contains five paramaters, is reduced from 5 to 2 (Equation 5.7). Therefore, learning from limited significant MLS data is achieved. Similarly, the best candidate of $\boldsymbol{D}$ is calculated as

$$\boldsymbol{D}_{best} = \arg\max_{0 \le i \le 5} \left(p(\boldsymbol{D_i}|\boldsymbol{C}_j, \boldsymbol{HE}) \right) \tag{5.8}$$

The probability of spatial features of $\boldsymbol{D}$ can be computed by:

$$p(\boldsymbol{D_i}|\boldsymbol{C_j}, \boldsymbol{HE}) = \frac{p(|\boldsymbol{BD}|) \times p(\angle \boldsymbol{ABD}, \boldsymbol{HE})}{p(\boldsymbol{HE})} \tag{5.9}$$

Finally, we take the candidate among all candidates of $\boldsymbol{C}$ and $\boldsymbol{D}$, which gives the highest probability calculated from Equation (5.7) and (5.9) respetively.

5.3.4 Missing candidates

There is still a problem that there may be cases in which no candidate of point $\boldsymbol{C}$ or $\boldsymbol{D}$ is found during the marker detection phase. This could happen if there is significantly large deformation of the brain that the ventricles are compressed and fail to present in the images. We solve this problem by employing auxiliary points $\boldsymbol{E}$ and $\boldsymbol{F}$ which are the end points of the falces.

From observation, the end of the falx is near the ventricle. Because we do not know whether valid candidates of $\boldsymbol{C}$ or $\boldsymbol{D}$ will be detected, we simply treat the candidates of $\boldsymbol{E}$ ($\boldsymbol{F}$) to be the candidates of $\boldsymbol{C}$ ($\boldsymbol{D}$). Thus we combine the $\boldsymbol{E}$ ($\boldsymbol{F}$) candidates to the $\boldsymbol{C}$ ($\boldsymbol{D}$) candidates list. Obviously, the combinination introduces errors. Therefore, we discourage the combination by penalizations. Recall that the best candidate is selected because it gives the highest spatial probability. The penalization is achieved by multiplying a penalty factor to discount the spatial probability learnt using $\boldsymbol{E}$ ($\boldsymbol{F}$) candidates instead of candidates of $\boldsymbol{C}$ ($\boldsymbol{D}$). The factor is learnt empirically, so that if there is a proper $\boldsymbol{C}$ ($\boldsymbol{D}$) candidate, the algorithm will not select any of the $\boldsymbol{E}$ ($\boldsymbol{F}$) candidate. Moreover, if all the $\boldsymbol{C}$ ($\boldsymbol{D}$) candidates are outliers,

the algorithm will pick the best ***E*** (***F***) candidate to replace ***C*** (***D***). We shall see from the experimental results in next section that the algorithm successfully handles the missing third ventricle case, which previous methods can not handle.

Finally, we connect all the best candidates to delineate the deformed midline. (Figure 5.20)

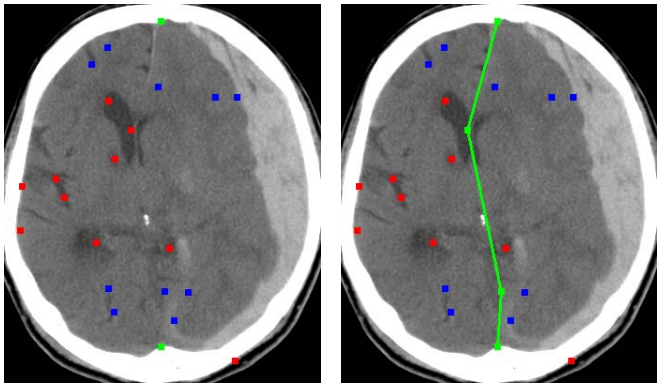

a **b**

Figure 5.20. Final result: a: all the candidates; b: the best candidates and the traced midline

5.4 Quantification of the Midline Shift

In previous steps, we have traced the deformed midline in TBI CT images. The next step is to quantify the amount of the shift.

A traditional measurement is the maximum distance by which the DML deviates from the IML. The maximum distance measurement is normally used daily in clinics. It is the largest distance of all points on the deformed midline (DML) to the ideal midline (IML). The sign of the distance indicates the direction of shift. Negative sign indicates shift to the left while positive sign indicates shift to the right (Figure 5.21, parameter ***d***).

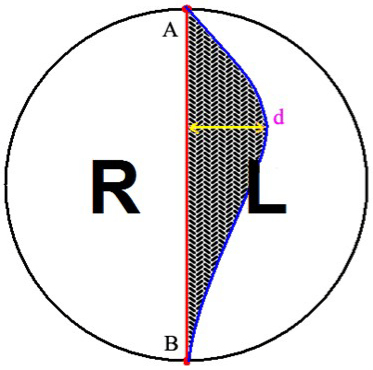

L	*Left brain hemisphere*
R	*Right brain hemisphere*
*Straight line **AB***	*Ideal midline (**IML**)*
*Curved line **AB***	*Deformed midline (**DML**)*
d	*Maximum distance*
Shaded area	***A***
Original area ratio	***L/R = 1***
Current area ratio	***(L-A)/(R+A) < 1***

Figure 5.21. MLS quantification measurements.

However, the maximum distance only captures the shift at one single point. It does not consider other points and the shape of the deformed midline. For example, consider the two cases in Figure 5.22: both MLS shown in the left and right illustrations have same maximum distance deformed. However, they have different shapes and different deformations at the lower part. The right case has deformed more than the left case by the area shaded in the checker-board pattern. Hence, we also proposed the area ratio measurement instead of maximum distance alone. The deformed midline divides the brain into two halves. The ratio between the volumes of the two halves can be used as a measurement of the shifting amount. In the case shown in Figure 5.22, although the MLS in both images have same maximum distance ***d***, the deformed areas of both MLS are different and they are captured by the area ratio measurement.

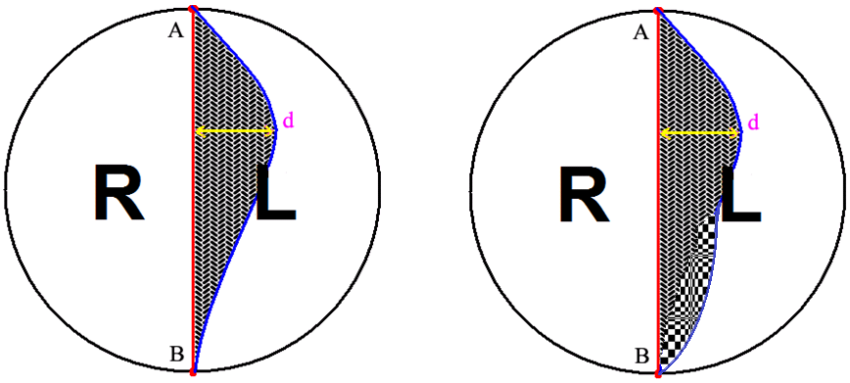

Figure 5.22. Two cases with the same maximum distance but different area ratios.

The area ratio measurement has been proposed to doctors for clinical study and practice and waiting for feedbacks.

5.5 Summary of the Chapter

In this chapter, we have proposed an anatomical marker model to model the brain midline shift, and algorithms are developed based on the model. The model takes as input the middle slice. It outputs markers ***A*** and ***B***, at most 5 candidates of markers ***C***, ***D*** and auxiliary markers ***E*** and ***F*** respectively. Note that there may not be any candidates detected. The hemorrhage is also a factor affecting the candidate selections. It is also considered in the selection process.

The selection process selects the best candidates for markers ***C*** and ***D***, which are centers of the frontal horn and the third ventricle. The process is fully automatic and robust against arbitrary brain distortions. In the extreme case that the ventricle is absent in the image, it is not possible to segment the ventricle using any segmentation

algorithm. The approximation using falx endpoints is still able to estimate the location of the ventricle.

The deformed midline traced by the anatomical marker model is then quantified using two measurements: the maximum shift distance and the area ratio.

We also propose a novel technique to locate the brain falx in brain CT images. Brain falx is an important anatomical feature for TBI diagnosis. However to our best knowledge, there is no algorithm currently available to extract brain falx. The proposed algorithm is the first falx segmentation algorithm for brain CT images.

Importantly, the proposed algorithm successfully uses spatial relationships on midline shift detection, and imaginary object on CT images. The leant probability of the spatial relationships makes the algorithm robust to various brain distortions. The learning also helps in the ventricle and falx identification.

Chapter 6

EXPERIMENTAL EVALUATION

In previous chapters, we have introduced our proposed method of tracing and quantification of the deformed midline in TBI CT images. In this chapter, experiments have been carried out to show that the proposed MLS tracing method outperforms current methods in literature. We also show that the proposed method is able to handle cases in which the state-of-the-art methods fail. Moreover, a patient retrieval system is constructed as an application of the proposed algorithm.

The chapter is organized as follows. Firstly, we show the performance of one MLS tracing method using quantative measurements. Secondly, we compare our methods with the state-of-the-art methods. Thirdly, we discuss cases in which our method succeeds while other methods fail. Finally, we show a patient retrieval system as an application of the proposed algorithm.

6.1 Performance of the Proposed Algorithm

In this section, we show the performance of the proposed MLS quantification algorithm and compare it with the performance of the algorithms in the literature. Firstly, we shall show the performance of the detection of each marker in AMM.

Then quantitive results of our proposed algorithm using our proposed quantification measurements are presented.

6.1.1 Experimental dataset description

The experimental data set contains totally 565 patients with 7040 brain CT images (slices). Each patient has around 12 scan slices. Each CT image has resolution 512 by 512, with each pixel covering 0.5mm.

The patients have traumatic brain injury with MLS to different extent. The profile of the data regarding to various amount of midline shift distances is illustrated in Figure 6.1 below.

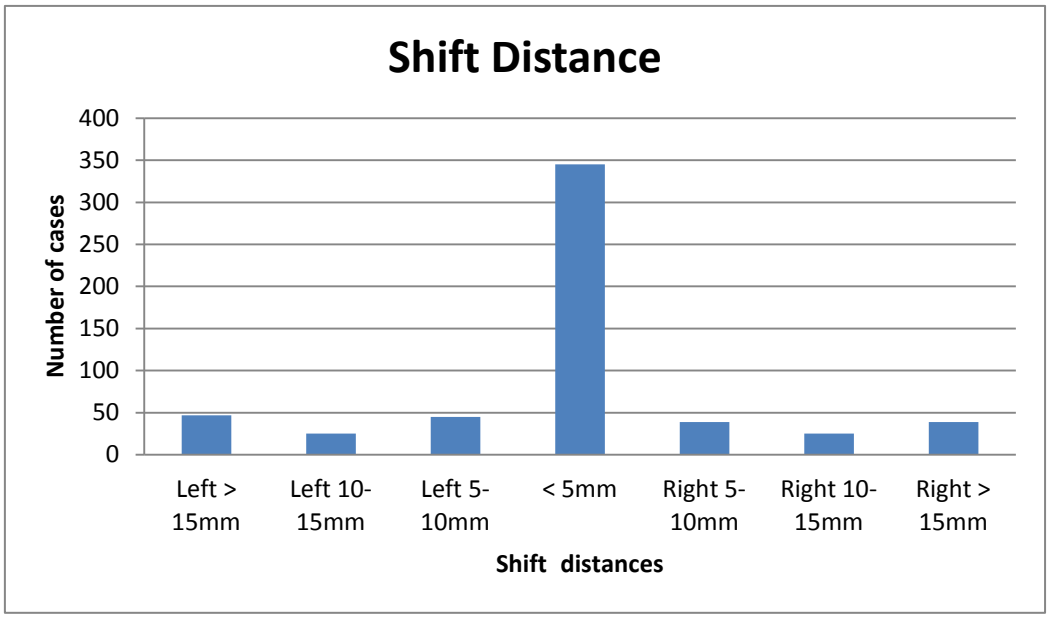

Figure 6.1. Profile of the midline shift distances.

Note that most patients have either no shift or slight shift within 5mm, due to the high mortality of patients with significant MLS in clinical admission.

The data were collected from the National Neuroscience Institute and Tan Tock Seng Hospital during 2007 to 2009. All patients were admitted return 2002 and 2006. Due to legal issues, the patients' identities are anonymized.

6.1.2 Evaluations of detection of individual markers

The proposed algorithm detects marker ***A*** and ***B***, candidates of markers ***C***, ***D***, ***E***, and ***F***. To evaluate the performance of the detection algorithm, we calculate the Euclidean distance between the marker detected by the algorithm and the ground truths marker with 5 pixels' tolerance. For candidates detection evaluation, if any of the candidate has distance to the ground truth point less than 5 pixels, the candidate is considered successfully detected. We then measure the sensitivity of the detection algorithm by the "success rate", which equals to the number of successfully detected cases divided by the total number of cases. The performance is then shown below (Table 6.1).

Table 6.1. The sensitivity of detection algorithms.

Markers	***A***	***B***	***C***	***D***	***E***	***F***
Success Rate	75.22%	86.90%	98.41%	95.75%	93.63%	92.39%

6.1.3 Experimental results using proposed measurements

We evaluate the performance of our proposed MLS tracing algorithm using the two criteria proposed in Chapter 5, namely, the volume ratio and the maximum

distance of the MLS. Therefore, we conduct our experiments in a way that each test image has two pairs of values for evaluation: the estimated value versus the ground truth value of volume ratio, and the estimated maximum distance versus the ground truth maximum distance. The ground truth data are generated from deformed midline marked by professional radiologists. We compute the MLS estimation error as the absolute difference between the estimated value and the ground truth value for each criterion. The distance is expressed in millimeters. The distributions of the errors are shown in Figure 6.2 and evaluated using mean and standard deviation in Table 6.2.

Table 6.2. The experimental results statistics.

	Mean	**Standard deviation**
Area ratio error	0.0765	0.0883
Maximum distance error	4.7317mm	5.1408mm

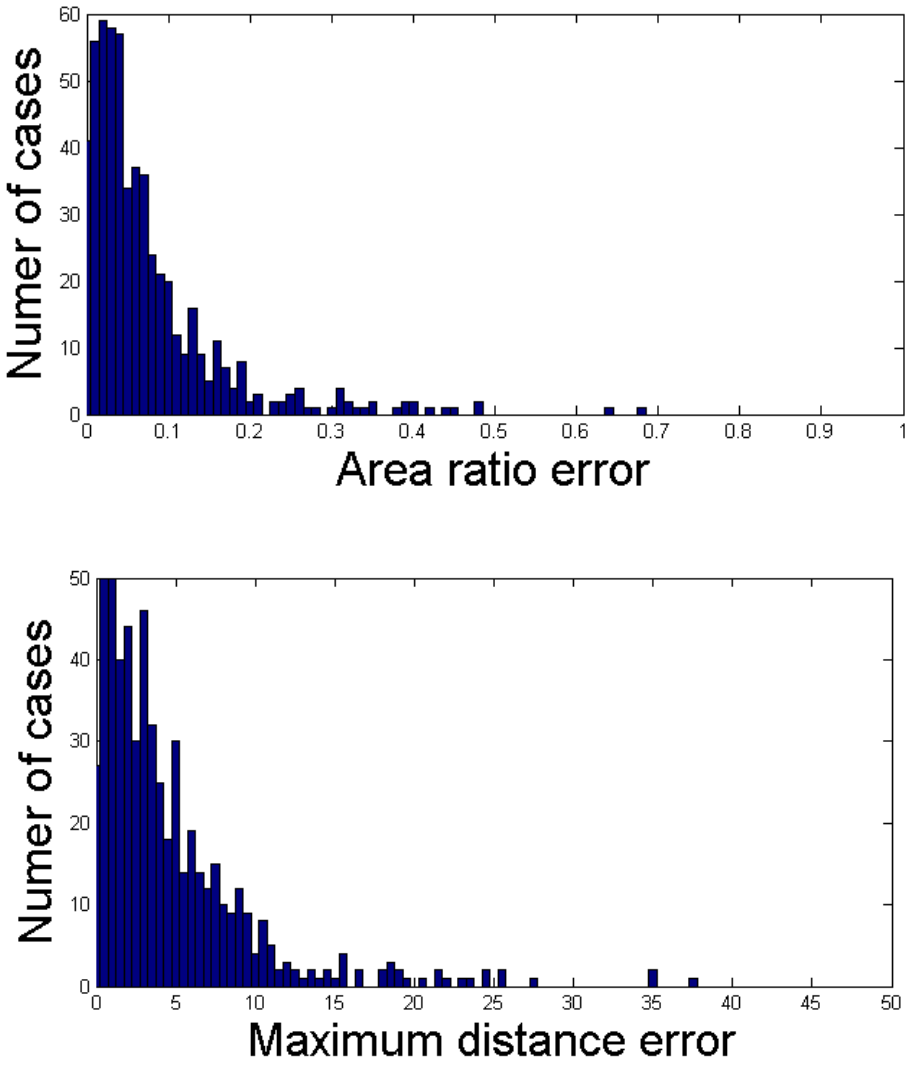

Figure 6.2. The error distributions of the MLS quantification results using the proposed algorithm.

From Figure 6.2 we see that the error distribution has approximately a half normal distribution shape. 80% erros are distributed within 0.1 for area ratio and 5mm for the maximum distance.

The running time is 7.93 seconds per patient and 0.57 seconds per image. The complexity of the algorithm is O(*mn*) where *m* is the number of patients and *n* is the average number of slices per patients.

Some detection results are shown below (Figure 6.3).

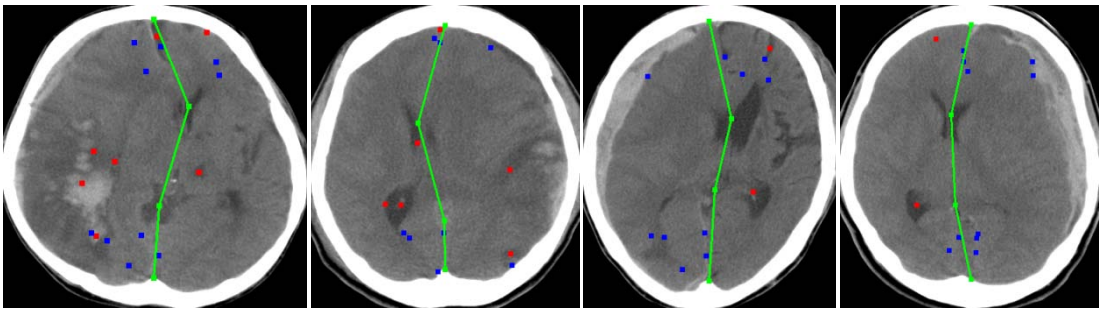

Figure 6.3. Sample results of MLS quantification

6.1.4 Results analysis and discussion

In this section, we shall analyze the errors and failure cases.

The small error within a few pixels mainly comes from the ventricle candidate point generation. The methods simply pick the center of the ventricle region as the candidate point. However, in some cases of deformed ventricle, the center of the anatomical ventricles is different from the geometrical ventricle regions. As shown in the circled area in Figure 6.4, the frontal horn is deformed. The areas segmented are marked as red regions. The centers are marked as green dots. We see that the center is misplaced more on right side. The correct candidate point should between the left and right parts of the frontal horn (Figure 6.4, blue star). Fortunately, this difference is not large. Empirically, the difference is within two or three pixels. The difference can be improved by employing shape analysis on the ventricle regions. However, it will sacrify computational time. Our suggestion is that the shape analysis method will be only employed when doctors want to extensively analyze single case. Otherwise, the

method will only pick the center of the ventricle regions as candidates to save computational time on large amount of cases. This difference is also one of the reasons of the underperformance of the algorithm on the insignificant cases where MLS is within several pixels.

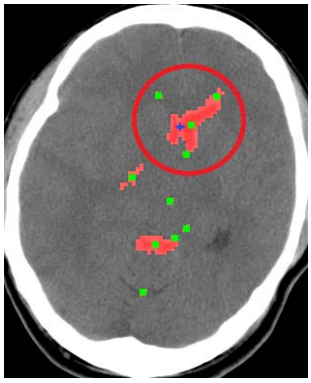

Figure 6.4. Ventricle center: anatomical vs. geometrical.

Some failures are due to the failure of normalizing the image and locating the skull points ***A*** and ***B***. From Figure 6.5, we see that the skull is rotated. Thus the skull points ***A*** and ***B*** (red points) are wrongly calculated. So does the ideal midline ***AB***. Because ***A*** and ***B*** are wrongly calculated, the spatial relations of other candidates with ***A*** and ***B*** are not valid any more. Thus the algorithm fails to select the correct candidate points.

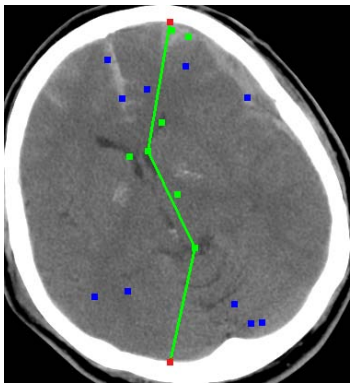

Figure 6.5. Failure to calculate the skull points.

We know that the midline shift is mainly due to the pushing behavior of the hemorrhages. However, in some clinical cases, even large hemorrhage may not shift the midline. For example, in Figure 6.6, an intracerebral hemorrhage is correctly identified, with its center marked as a red point in the upper half of the image. The candidate points are also selected (green points). By learning from the training data, the hemorrhage will push the midline toward the right of the image. Thus it selects the candidates fulfilling this pushing effect. However, as there is actually no shift presented, the correct candidate should be the golden point locating at the central part of the image.

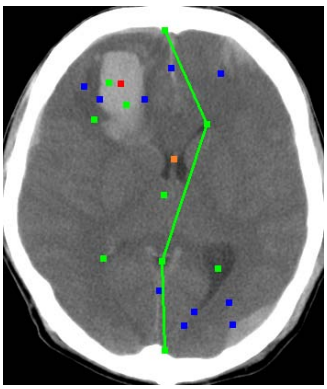

Figure 6.6. Hemorrhage fails to shift the midline.

6.2 Experimental Results Comparison

6.2.1 Comparison with the symmetry model

We have compared our method with Liao's symmetrical model [Liao06] (see Chapter 3, Section 3.1) following Liao's experimental design.

Liao's experiments [Liao06] were run on 81 images. The images were manually picked from CT scan series of patients with MLS. The result reported by Liao et al. includes sensitivity to retrieve midline shift larger than 5mm, which they call "success rate". The sensitivity is the ratio of the positive cases identified.

To make the experimental results convincing, we implement Liao's method and test it on our data set and use the same evaluation metric. Within the same data set as described in Section 6.1.1, the success rate under Liao's method reaches 94.09%, while ours is 95.91% which is 1.82% higher.

Another comparison factor is the running time. Running both algorithms on the same computer, our running time is 7.93 per patient, while Liao's method is about three minutes per patient. This is mainly due to the genetic algorithm takes longer time to converge to local optima. Ours is around 22 times faster than Liao's method.

Moreover, Liao's method cannot handle the cases that the symmetrical structure is destroyed by large intracranial hemorrhage (ICH), while our method is able to handle such case. This is discussed in Section 6.2.4.1.

6.2.2 Comparison with the ventricle shape matching model

We have compared our method with Chen's ventricle shape matching model [Chen10] (see Chapter 3, section 3. 2) following Chen's experimental design. Here we shall show the indirect and direct comparison results.

Chen's method [Chen10] operates on data of 264 images from 40 patients while our dataset contains 7040 images from 565 patients.

For comparison, we implement Chen's model was tested it on our data set. Chen also uses Liao's evaluation metric, known as the "success rate", which is the sensitivity to retrieve patients with MLS larger than 5mm. In addition, Chen gives a tolerance threshold of 2.25mm. Within the same data set and using the same evaluation metric, the sensitivity of Chen's method reaches 91.36%, while ours is 95.91%.

Another comparison factor is the running time. Running both algorithms on the same computer, our running time is 7.93 per patient and 0.57 seconds per image, which is three times faster than Chen's model. The longer computational time in Chen's method is mainly spent on the shape matching process, which is mainly a registration process.

Moreover, Chen's model cannot handle the case of missing ventricles, while our method is able to trace the midline even the ventricles are in large deformation or even disappeared. This is discussed in Section 6.2.4.2.

6.2.3 Comparison using the proposed evaluation criteria

We have also done comparisons of all the three methods (Liao's [Liao06], Chen's [Chen10], and ours) using our proposed evaluation criteria, i.e, the area ratio and the maximum distance. The result statistics are illustrated in Table 6.3 and Figure 6.7. The error distributions are shown in Figure 6.8 and 6.10. Figure 6.8 displays the comparison of the distribution of maximum distance error generated by the three methods. Figure 6.9 illustrates the comparison of the distribution of area ratio error generated by the three methods.

Table 6.3. The results comparison of all the three methods.

	Area ratio		Maximum distance	
	Mean	**Standard deviation**	**Mean**	**Standard deviation**
Liao's method	0.2083	0.3111	14.07mm	16.67mm
Chen's method	0.1109	0.1495	7.093mm	10.35mm
Our method	0.0766	0.0883	4.738mm	5.141mm

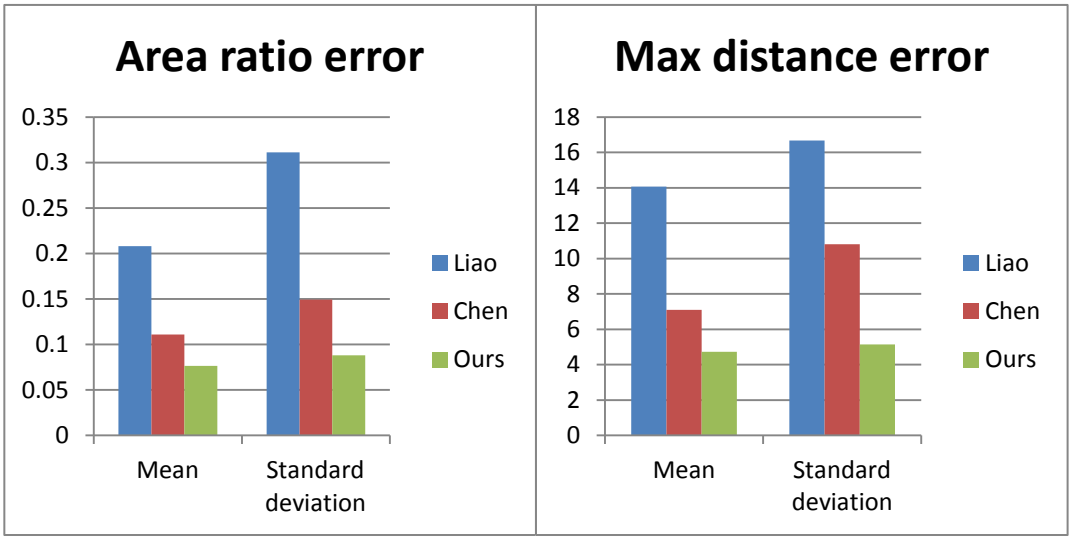

Figure 6.7. Comparison of all methods.

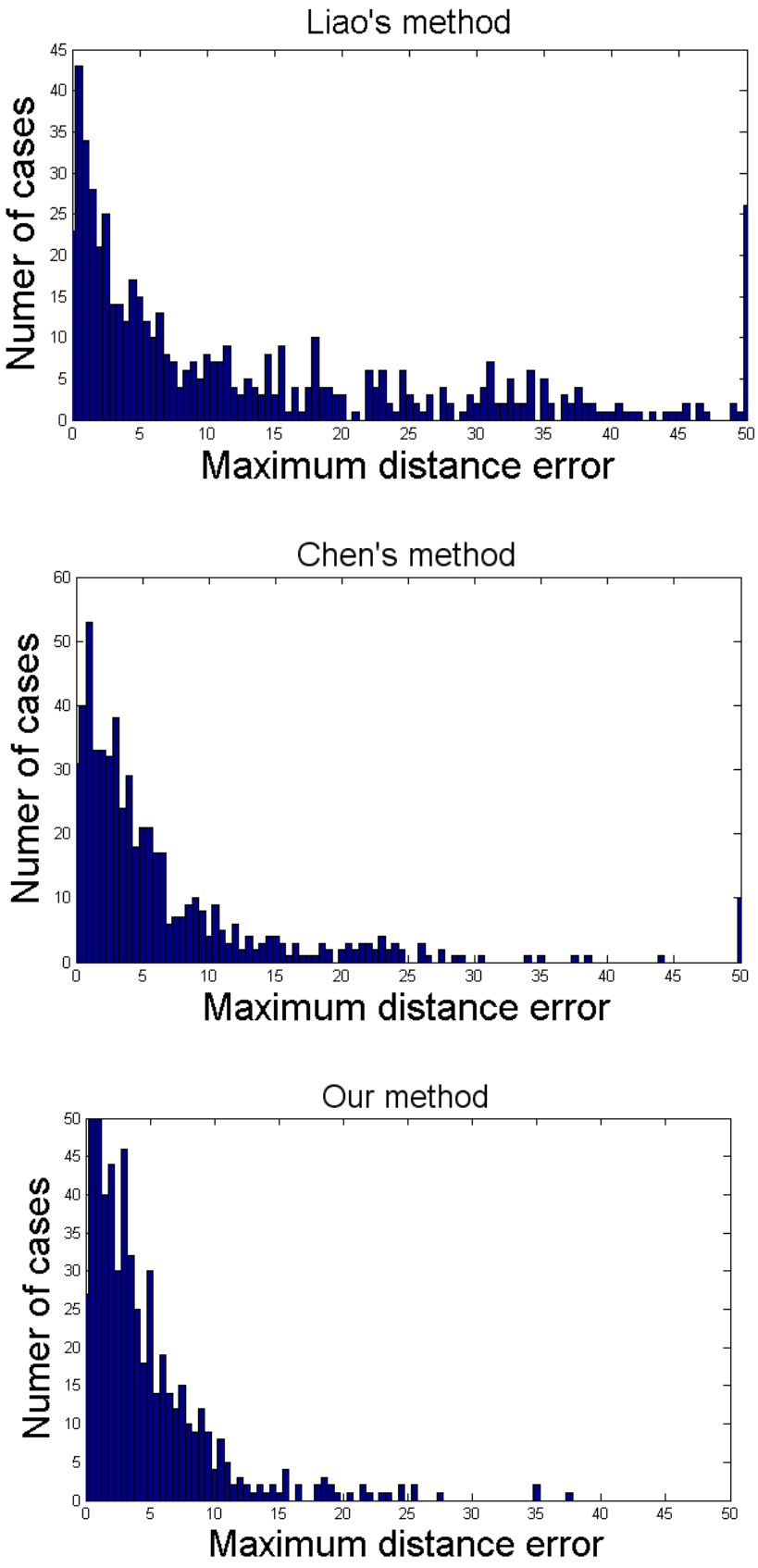

Figure 6.8. Comparison of the distribution of maximum distance error.

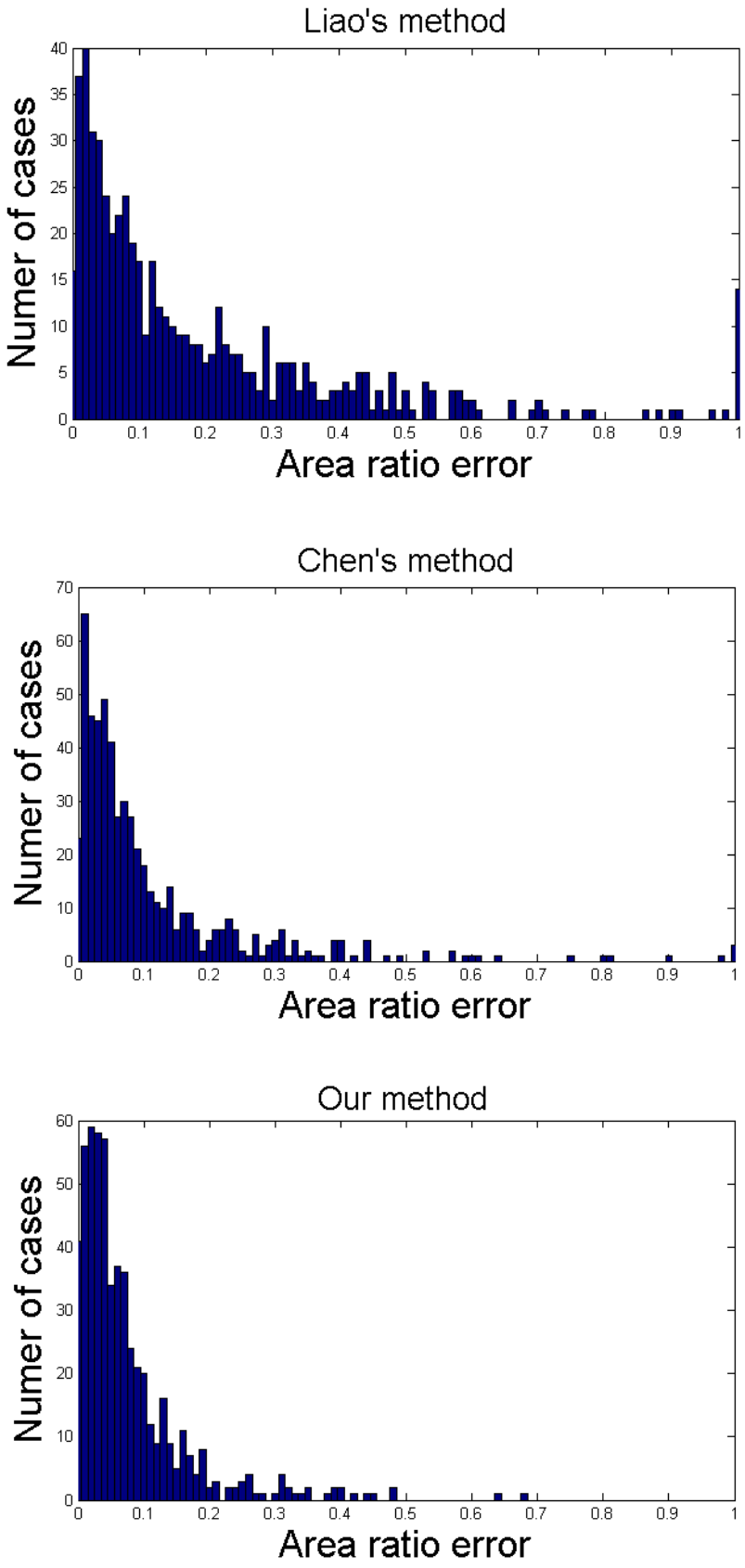

Figure 6.9. Comparison of the distribution of volume ratio error.

To test the significance of our algorithm, we have run a pair-wise hypothesis test (t-test) [Fisher25] on the means of errors obtained from both measurements. The purpose of the test is to check whether our method significantly reduces the errors comparing with Liao's and Chen's method, between automatic and manual quantification of MLS using the two measurements, namely, the area ratio and the maximum distance. The test should be single-tail on the left because we test whether our errors are less than the comparing methods. We use 5% significant level. Therefore, the critical *t* value should be 1.645. Thus we conclude the error reduction is significant. The computed statistics are shown in Table 6.4 below.

Table 6.4. The statistics of the hypothesis testing.

	Area ratio	**Max distance**
Compare with Liao's method	2.5160	12.8925
Compare with Chen's method	1.6441	4.2599

From Table 6.4 we see that, regarding to the maximum distance measurement, our method significantly reduced the error comparing with Liao's method and the Chen's method. Regarding to the area ratio measurement, our method improves the results comparing with Liao's method but reaches comparable performance with Chen's method (Fail to reject null hypothesis).

6.2.4 Comparison on difficult cases

The proposed algorithm can handle special MLS cases which the state-of-the-art algorithms fail to handle. We call those special cases “difficult”. In this section, we shall discuss the two types of hard cases which previous algorithms fail to handle.

6.2.4.1 Non-symmetric brain structure

Large ICH may destroy the symmetrical structure of the brain (Figure 6.10). Spontaneous ICH occurs mostly around the midline at the basal ganglia, and the ventricles are also frequently involved. Moreover, large MLS will also deform the brain severely and cause the loss of symmetry (Figure 6.10).

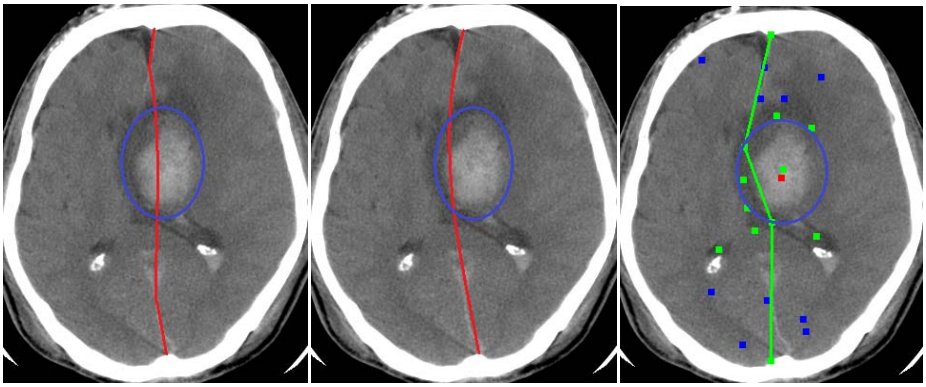

Figure 6.10. MLS tracing in non-symmetrical brain. Left: Liao’s result; Middle: Chen’s result; Right: our result; Circled area: large ICHs.

Hence, Liao’s method based on the symmetrical brain structure fails on this case. Our method is based on anatomical structure rather than the symmetrical structure. Hence, our method is still able to trace the midline under non-symmetrical brain (Figure 6.10, green lines).

6.2.4.2 Absent ventricle

Severe brain injury may cause large deformation of the brain. Ventricles may be compressed and fail to present on the CT scans (Figure 6.11). Chen's method does not consider cases in which one side of the lateral ventricle is missing or the ventricles are not visible [Chen10]. Because the method traces midline based on ventricles segmented, it fails to detect midline in such cases.

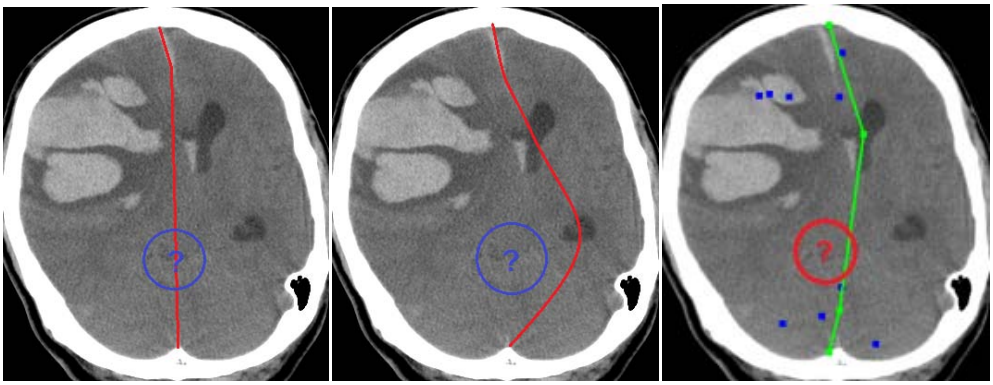

Figure 6.11. Missing ventricles. Left: Liao's result (fail to detect); Middle: Chen's result; Right: our result; Circled area: Missing the third ventricle

Our proposed algorithm estimates the absent ventricles from the falx. It uses the end points of falx as candidates to estimate the missing ventricle centers (Figure 6.11).

From Figure 6.11, we see that the question marks circled in red represent the missing ventricles. The green dots are centers of the ventricle regions segmented and the blue dots are the ending points of the falx. We see that the algorithm fails to segment the ventricles as there are no green dots. However, it uses ending points of falx to estimate the center of the third ventricles.

6.3 Application: A Patient Data Retrieval System

Nowadays, a huge amount of CT images is produced in modern hospitals. For example, the Neuroradiology Service at the National Neuroscience Institute (NNI), Tan Tock Seng Hospital, performed over a thousand CT scans, with each scan consisting of around 20 slices, in the two-year period of 2003 to 2005 as a result of hospital admission for mild head injuries. This provides us with a gold mine which contains precious knowledge valuable to us to discover for medical study. However, today, the CT scan images are in the standard DICOM (Digital Imaging and Communication in Medicine). They are displayed and retrieved via PACS (Picture Archives and Communication Systems), which can only be retrieved by patient ID or patient name, which are stored in the DICOM header. Hence to retrieve an image based on anomaly without the patient name or ID is a hard task. Effective and efficient content-based retrieval techniques are required to access the huge amount of data. In this chapter, we build a patient data retrieval system based on symptoms such as hemorrhage position and size, and midline shift amount, and other Meta-data such as patients' age, gender, admission information and outcomes.

6.3.1 The System Framework

The architecture of the patient data retrieval system is illustrated in Figure 6.12.

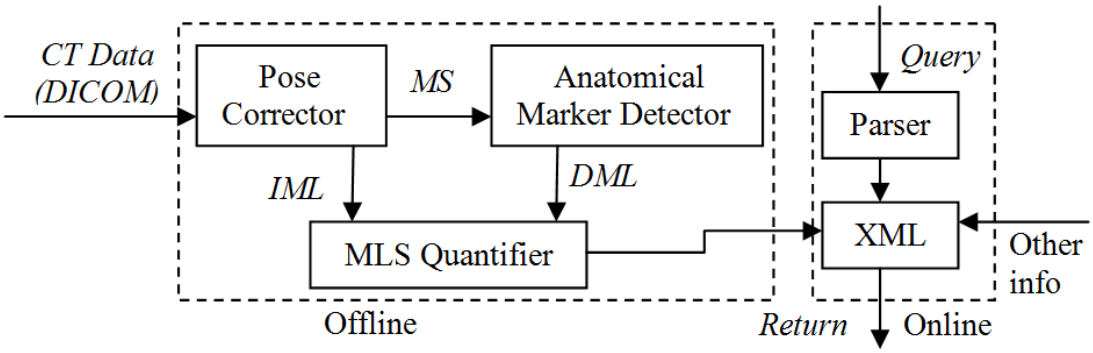

Figure 6.12. The structure of the proposed retrieval system.

Generally, the system processes each patient's CT data offline, where it traces and quantifies the MLS, and constructs XML document for retrieval purpose. The retrieval process is achieved through Xquery on the XML documents outputted offline.

The offline processing has three components, namely, the Pose Corrector (slice indexing, explained in Chapter 4), the Anatomical Marker Detector (AMM model, anatomical feature detection and selection, explained in Chapter 5), and the MLS Quantifier (MLS quantification, explained in Chapter 5). The input CT data are in DICOM format. Since the size and scanning angle vary among patients, the system first passes the input data into the pose corrector. The corrector computes and picks out the MS, and does a pose correction on the MS. During the pose correction, the IML is found. The corrector will output the slices around MS to the detector, and output the IML to the quantifier. The detector detects anatomical markers based on those slices. The DML is then described by the anatomical markers in the detector and outputted to the quantifier. With the IML and DML, two measurements are employed by the quantifier to quantify the MLS, namely, area ratio and maximum distance of deformation. These two measurements are then output to an XML file for retrieval.

A sample XML is shown below:

```
<Patient id="12345">
   <DOB>19290315</DOB>
   <AGE>74</AGE>
   <SEX>MALE</SEX>
   <DATE>20040119</DATE>
   <TIME>093028</TIME>
   <OUTCOME>
      <Death_date>NA</Death_date>
      <Death_time>NA</Death_time>
      ...
     </OUTCOME>
     <MLS>
          <Direction>LEFT</Direction>
          <Area_ratio>1.1081</Area_ratio>
          <Max_dist>2.2608</Max_dist>
     </MLS>
</Patient>
<Patient id="22222">
```

As we can see in the above example, the system also integrates other information such as patient's age, clinical outcomes such as death information, etc. in the XML. Each patient currently has attributes such as date of birth, age, gender, scanning date and time, outcome information and the MLS information. Query can be made based on any of these attributes. The attributes are extendible. For example, users may also input other attributes such as discharge information in the outcome information. In the online processing, text queries are passed to a query parser and transformed to an Xquery.

We ask specialists to give 3 typical queries on the system. The queries are illustrated in Table 6.5. Some results are shown in experiment part in Section 5.

Each query is parsed into an Xquery and processed using standard XML query methods. Here we choose XML because it efficiently supports reverse query (i.e. query the roots based on information of leaves in the XML tree data structure).

Table 6.5. Sample queries.

	Query
1	Patients without significant MLS (less than 5mm)
2	Patients with MLS larger than 1cm to the right.
3	Surviving patients with MLS to the left larger than 1cm scanned in 2005.

6.3.2 System Performance

The queries are evaluated following Chen's proposed evaluation criteria [Chen10], which uses 2.25mm tolerance in the maximum distance measurement. The performances on the three queries in the previous section are shown in Table 6.6.

Table 6.6. Query results.

	Q1	**Q2**	**Q3**	**Avg.**
Recall	1.0000	1.0000	0.9934	**0.9978**
Precision	0.6106	0.8071	0.8025	**0.7401**
F-score	0.7582	0.8932	0.8878	**0.8464**

The results are promising in all measurements such as recall, precision, and F-score. We can see that the results present a higher recall than precision. The system tends to give more false positives. However, false positives are generally preferred in clinical study as further post-processing is normally required by doctors. This is because:

(a) Legal issue. A normal patient is diagnosed to be abnormal will not suffer from the disease and surely will not die. However, an abnormal patient is diagnosed to be normal will miss the healing opportunity and this may be fatal. A fatal case can destroy a doctor's future due to a lawsuit.

(b) Humanity issue. People normally will not miss any chances to survive. Even the chance is a false positive.

Therefore, the high recall is normally preferred in the medical retrieval system.

Currently there is no such kind of benchmark on the retrieval of patients' information based on the MLS. Although Liao et al. [Liao06] and Chen et al. [Chen10] have given the "success rate" which is the sensitivity, they do not give F-score and specificity. This is the first work of its kind, the results are promising and we envisage that it will lead to further work in the community.

Some sample query results are shown in Figure 6.13 below.

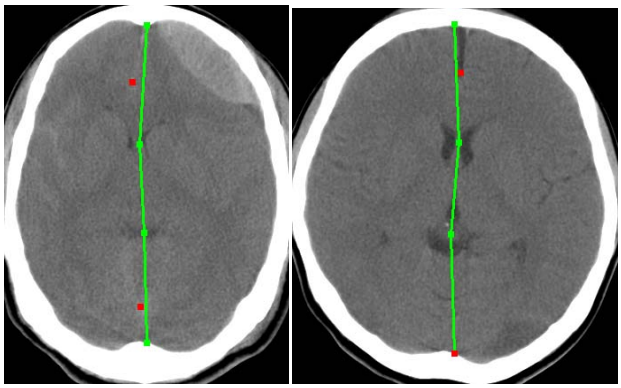

Sample results of query 1

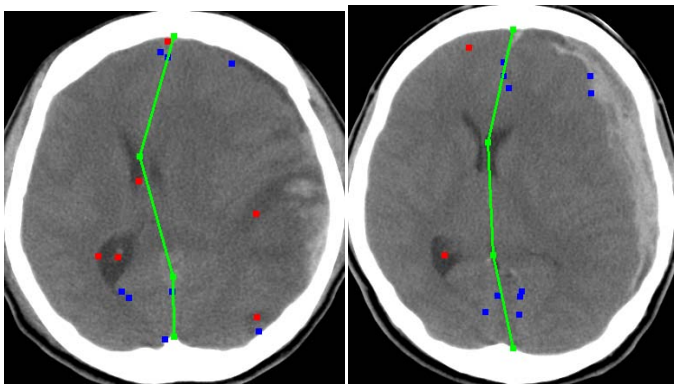

Sample results of query 2

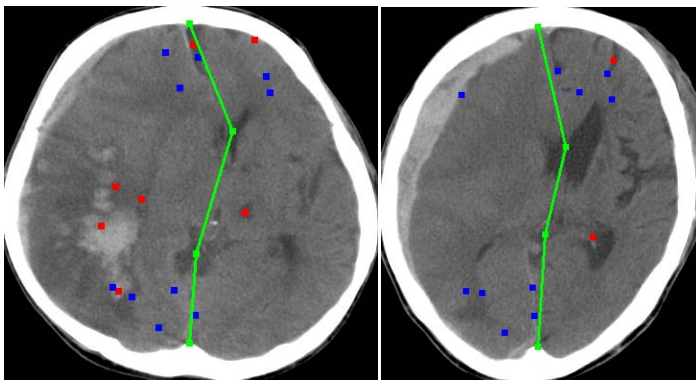

Sample results of query 3

Figure 6.13. Sample query results.

6.5 Summary of the Chapter

This chapter has presented the experimental results on the proposed algorithms. The results show that the proposed MLS tracing method outperforms current methods

in literature. Moreover, the results show that the proposed method is able to handle cases in which the state-of-the-art methods fail.

A patients' data retrieval system is constructed based on the proposed brain midline shift quantification algorithm. Unlike the current system, the system can retrieve patients' information not only based on patients' name or id, but also the symptoms such as hemorrhage position and size, and midline shift amount, and other Meta data such as patients' age, gender, admission information and outcomes. The system is expected to facilitate current clinical study and prognostic research.

Chapter 7

FURTHER WORKS

We have done some further works to extend or support the proposed algorithm. In this chapter, two items are discussed. The first one is brain slice indexing, which is an extension of the middle slice selection in the preprocessing step. The other is the study of the hemorrhage effect. The study supports the hemorrhage effect parameter used in the marker candidate selection algorithm (Chapter 5, Section 5.3).

7.1 Brain Slice Indexing

One axial brain CT scan consists of multiple 2D slices of different heights along the axial direction (Appendix). Practically, these slices are sometime disordered and unaligned. In cases of re-scanning, even the ordering of the slices is not correct. In computer-assisted diagnosis (CAD), correctly ordering and aligning the slices is an important preprocessing step before further pathological feature analysis. Such ordering and aligning process is called *the indexing of brain slices* (or sections) [Gefen08]. Moreover, with the increased amount of medical image data, content-based image retrieval (CBIR) has been proposed as a promising approach in

the new-generation hospital database management system [Műller04]. In CBIR, queries are often made by providing image examples. Indexing of slices is important if a single CT slice is provided by the user as a query example.

7.1.1 Related work on the indexing of brain CT slices

Current work in the literature for indexing of slices from brain imaging is based on image registration [Gefen08]. Work exists on MR images [Kim00] [Liu.J04]. Specifically, Kim et al. [Kim00] perform non-rigid registration of postmortem brain slices to MRI volume. In their method, a polynomial transformation was used to parametrically represent the deformation field. Later in 2004, Liu et al. [Liu.J04] proposes a non-linear deformable registration method for ultrasound spatial compounding. In their method, they apply a multi-resolution cubic B-spline registration to determine global and local nonlinear deformations following rigid registration from a position sensor. Then 2D slice images are divided into partly overlapped sub-images to estimate the residual local deformations. However, very limited work has been found presently to index brain CT slices. The most relevant work is proposed by Gefen et al. in 2008 [Gefen08] on mice brain CT scans rather than human brain. Their method is to register 2D image into a 3-D atlas. The tasks was carried out in two main steps, namely, image to planar surface matching (IPSM) and image to curved surface matching (ICSM). The first step (IPSM) is to find a slice in the 3D atlas that best matched the section to be indexed through affine registration. The normalized mutual information (NMI) score [Studholme99] [Pluim03] is used to

measure the similarity of the matching. The affine registration parameters are then computed through maximizing the NMI by genetic algorithm [Whitley93]. Once a matching image from atlas is found, the algorithm further refines the alignment by searching for a better matching image through ICSM. In this step, the atlas volume is deformed according to a 3-D displacement field such that the voxels overlay the indexing slice resulting on a new image. The displacement field is computed through maximizing a local 3-D similarity between (a) the atlas volume and (b) the volume extended from the indexing slice.

However, the registration process is usually too slow to be used in real-time CAD or CBIR system due to the non-linear deformation procedures involved. A fast method for indexing is urgently in need. In another aspect, indexing slices is generally a pre-processing step of further image study. Precise alignment of multiple slices is not necessary in most diagnosis or image retrieval tasks. A real-time CAD or CBIR system can adopt a fast indexing method with correctly ordered but only roughly aligned slices. Therefore, we need a fast algorithm to index brain slice into correct height levels operating on human brain CT scans.

In this thesis, we define the indexing of brain CT slices as follows. Given an arbitrary brain CT slice, we want to decide the height level of the slices. So the slice is “indexed” to certain height level for retrieval. The height level is one of the six levels introduced in Chapter 2 Section 2.2.1. Therefore, the indexing of brain CT slices can be viewed as a classification problem, in which each height level of the six is a class.

The method proposed for the indexing of brain CT slices mainly comprises two steps. Firstly, the same preprocessing step as introduced in Chapter 4 is used to obtain the middle slice (MS) and separate the encephalic region with the non-encephalic region (Chapter 4 section 4.1). Secondly, within each region, we further classify slices into different height levels in the region. Since the preprocessing step has already been introduced in Chapter 4, only the second step is presented in this section. Specifically, the second step contains three sub-steps: (a) feature extraction in the encephalic region; (b) feature extraction in the non-encephalic region; and (c) classification.

7.1.2 Feature extraction in the encephalic region

The encephalic region is from height level 3 to 5 (see Chapter 2, Section 2.2.1). We extract five features from slices in this region to further classify images in this region to different levels. These features are described as follows.

Feature 1: The size of the basal cistern.

The basal cistern is a wide cavity below the ventricle (Figure 7.1a). For calculation, it is located at the central block of $\boldsymbol{I}$ if we divide $\boldsymbol{I}$ into 3 by 3 blocks evenly. The area of basal cistern is calculated as the amount of CSF (cerebrospinal fluid) pixels inside this region. CSF pixels have intensity value 80~120. Because the total amount of CSF varies among different age groups, we calculate the ratio of the basal cistern area and the total area of CSF in the slice as the size of the basal cistern.

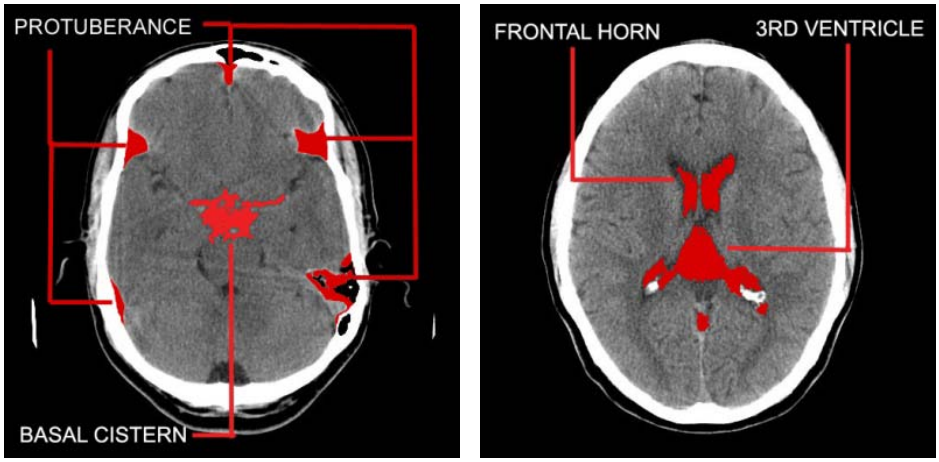

Figure 7.1. The anatomical structure of the encephalic region.

Feature 2: The size of the frontal horn.

The frontal horn is the front part of the lateral ventricle. It appears as ‘a horn of a bull (Figure 7.1b). For calculation, we define the frontal horn window as the lower 1/2 part of upper half of ***I***. The frontal horn area is computed as the amount of CSF pixels in the frontal horn window. The size of the frontal horn is calculated as the ratio of the frontal horn area and the total CSF area in the slice.

Feature 3: The size of the skull.

The area of the skull is the area bounded by the outer skull boundary. Because the area of the skull varies among different patients, we compute the ratio between the skull area and the skull area in the MS of the patient as the size of the skull in the slice. Recall that the MS is obtained from beginning using methods proposed in Chapter 4.

Feature 4: The size of protuberances along the inner contour of the skull.

The skull has protuberances inward around height level 3 (Figure 7.1a). To measure the size of the protuberances, we first calculate the inner contour of the skull, denoted as ***C***. We also calculate the convex hall ***H*** of the contour using Q-hull algorithm [Barber96]. Then we compute the ratio of the area bounded by ***C*** and ***H*** as measurement of the size of the protuberances. The larger the protuberances are, the smaller area ***C*** has, and thus the smaller ratio obtained.

Feature 5: The correlation with the MS.

We calculate the correlation of the slice with the MS. The higher the correlation is, the more similar the two slices are. Thus the slice is more probable to be at height level 4.

The feature distribution histograms on 802 slices of the 3 levels are plotted in Figure 7.2. There are 82 slices in level 3, 302 slices in level 4, and 418 slices in level 5. We see that the three lines representing the three levels have different peak for all features. For example, for feature 5, level 3 has peak around feature value 0.8, while level 4 has peak around feature value 0.9, and level 5 has peak around feature value 0.3-0.6.

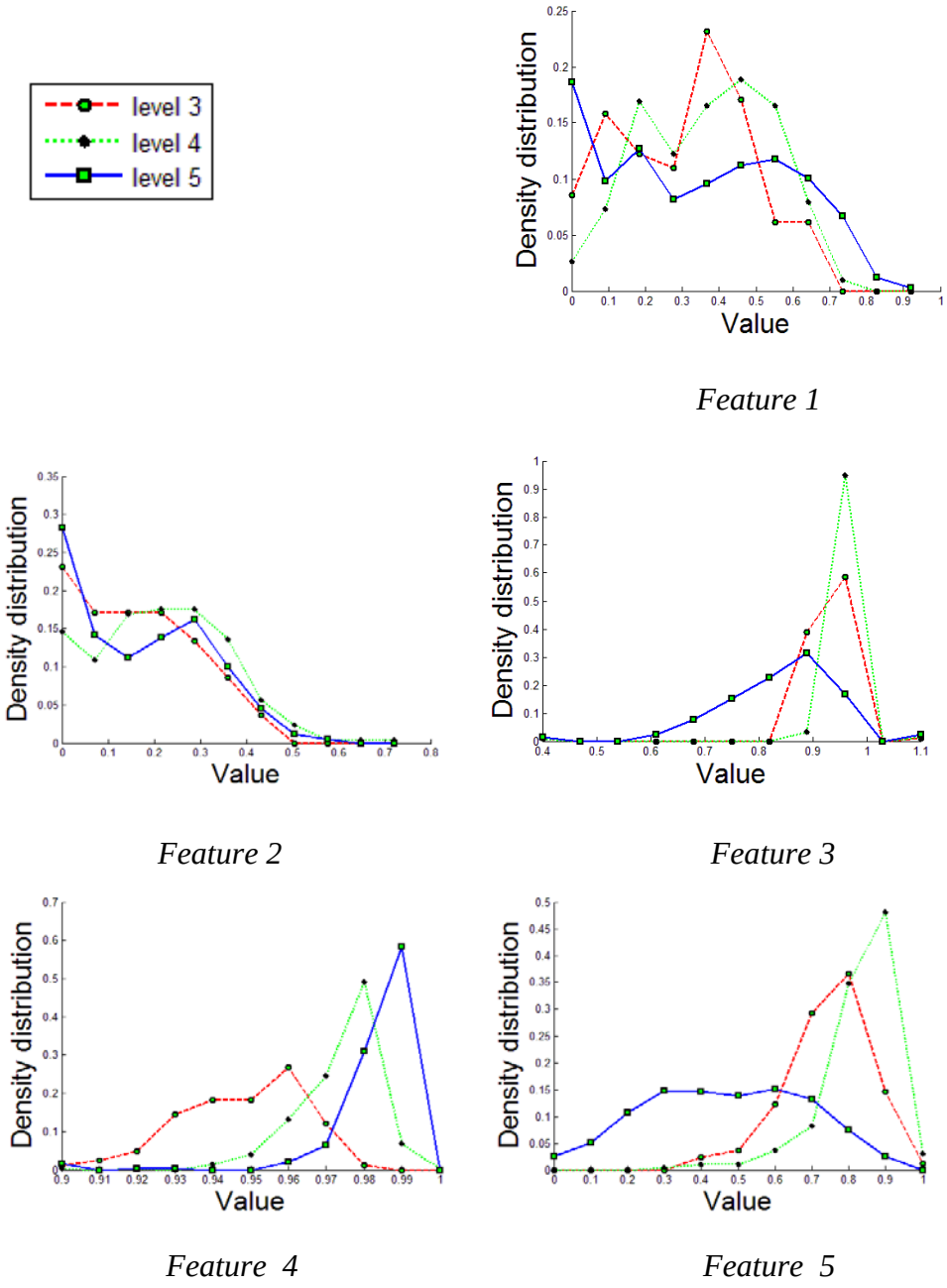

Figure 7.2. Feature histograms of encephalic region.

7.1.3 Features extraction in the non-encephalic region

The non-encephalic region contains height levels 1, 2, and 6. To separate these three levels, we extract three features according to their anatomical and image characteristics. The features are calculated as follows.

Feature 1: The area of the bounding box of the bone image.

The bone image is obtained by thresholding the slice using highest intensity value. The bounding box of the bone image is the smallest image that contains all the bone pixels.

Feature 2: The area of CSF in the eye region.

The eye region is defined as the upper 1/3 part of ***I***. The amount of CSF pixels in the eye region is computed. CSF pixel has HU 0~15.

Feature 3: The area of bone in the eye region

Similar to feature 2, the area of bone in the eye region is computed as the number of bone pixels in the eye region.

The feature distribution histograms on 757 slices of 3 levels are plotted in Figure 8.3. There are 251 slices in level 1, 195 slices in level 2, and 311 slices in level 6.

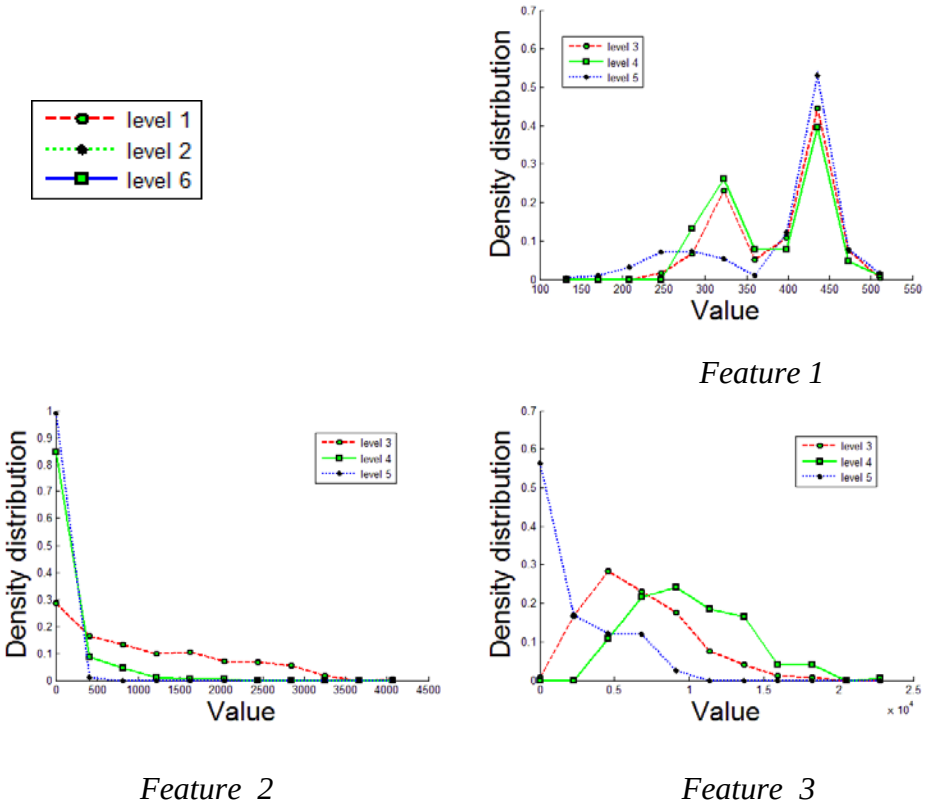

Feature 1

Feature 2 *Feature 3*

Figure 7.3. Feature histograms of non-encephalic region.

7.1.4 Classification

For classification in the encephalic region, we gather the five features into a 5 by 1 feature vector. For classification in the non-encephalic region, we gather the three features into a 3 by 1 feature vector. Based on these feature vectors, the two classification processes are done by SVM with linear kernel.

7.1.5 Experiments

The proposed indexing method is evaluated using CT images from 80 study cases. Each study case has around 20 CT slices. There are totally 1559 slices. Each slice belongs to one of six height levels. There are 251 slices in level 1, 195 slices in

level 2, 82 slices in level 3, 302 slices in level 4, 418 slices in level 5, and 311 slices in level 6. All experiments are done in 10-fold cross validation using MATLAB. We record the performance in all the 6 levels as shown in Table 7.1. The average runtime is 7.59 seconds for each study case and 0.38 seconds for classifying each test slice using Pentium 4GHZ CPU. Some indexed image results are shown in Figure 7.4.

Table 8.1. Results of the proposed indexing method.

Level	Precision	Recall	Accuracy	F-score
1	84.76%	70.92%	86.13%	77.22%
2	62.07%	73.85%	81.64%	67.45%
3	80.68%	57.72%	85.71%	67.30%
4	72.83%	83.44%	85.09%	77.78%
5	81.98%	87.08%	86.13%	84.45%
6	90.16%	91.32%	92.34%	90.73%
Overall	**79.73%**	**81.42%**	**86.58%**	**80.22%**

From the Table, we can see that our indexing algorithm is able to classify 80% the images into correct height level. The errors normally come from the transition levels, for example, level 3, and images at the boundary of the height levels because they share common anatomical information from both neighboring levels.

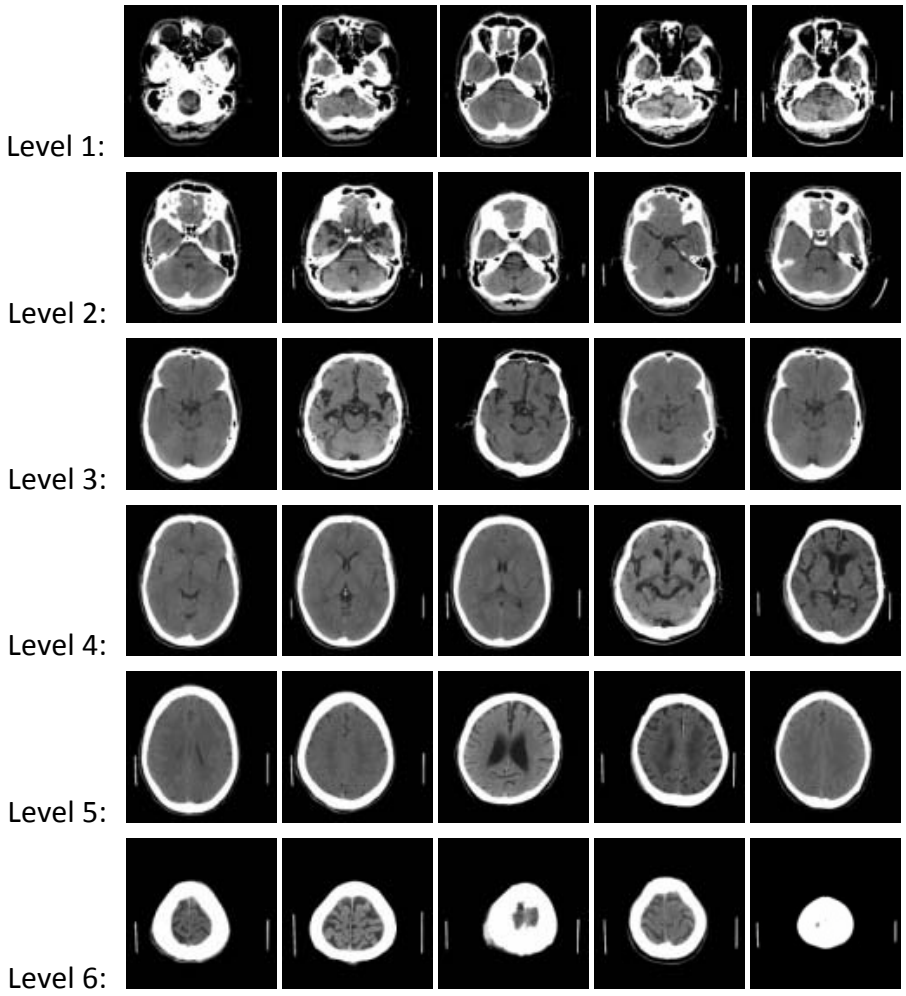

Figure 7.4. Sample results

7.2 Study of the Hemorrhage Effect

In this section, we study the hemorrhage effect. The effect is applied in the marker candidate selection as an important feature. Firstly, we show our observations on the linear relationship of the hemorrhage and the midline shift. Secondly, we propose a Hemorrhage-Midline shift (H-MLS) model to investigate the relationship. Thirdly, we study the relationship using the H-MLS model. Finally, we give our experimental results and show that the linear relationship of the hemorrhage and the brain midline holds.

7.2.1 The observations of the linear relationship of the hemorrhage and the brain midline shift

We manually marked hemorrhage regions and midlines of 200 traumatic brain injury patients. We plot (a) the size of the hemorrhage versus (b) the midline shift amount (Refer Chapter 6, Section 5.4 “maximum distance”). We observe that there is a linear relationship between the size of the hemorrhage and the midline shift distance (Figure 7.5). The larger the hemorrhage is, the more “pushing power” it has, and thus the larger distance it “pushes” the midline, i.e, the larger midline shifts.

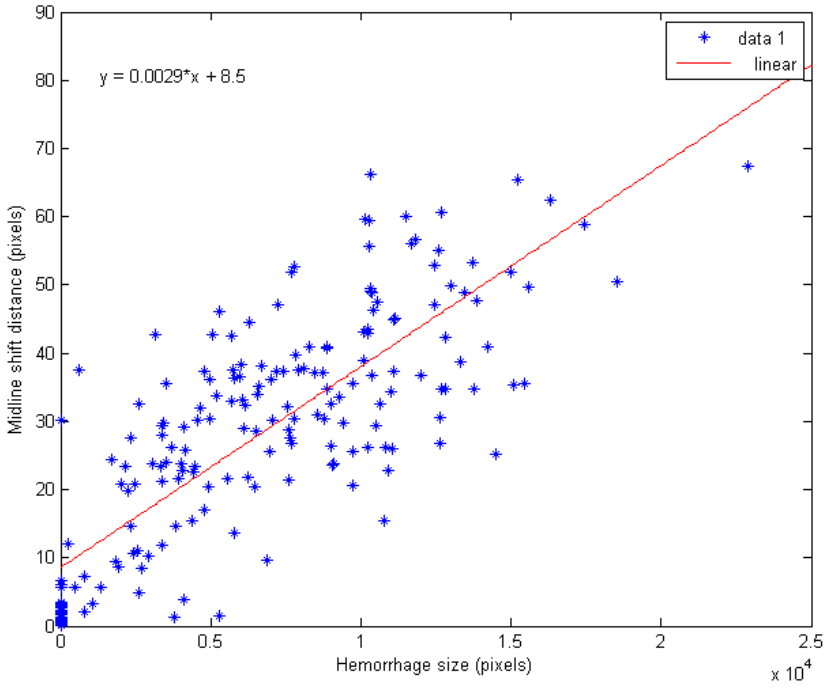

Figure 7.5. Plot of the hemorrhage size and the midline shift distance.

7.2.2 The H-MLS model

Based on the observation and the cause of the MLS introduced in previous section, we propose the H-MLS model to investigate the linear hemorrhage effect.

From large number of CT images presenting MLS (Figure 7.6), we observe that, generally, the amount of midline shift caused by hemorrhage is influenced by the following factors:

(a) The size of the hemorrhage: the larger the size is, the larger the amount of midline shifts.

(b) The distance between the hemorrhages to the IML: the longer the distance is, the smaller the amount of midline shift.

(c) The midline elastic property: points on the IML further apart from the skull are easier to be displaced.

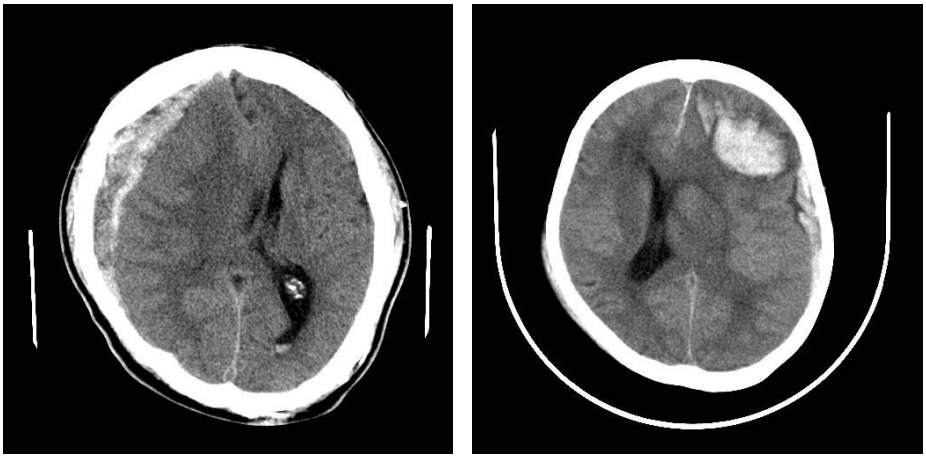

Figure 7.6. Examples of brain CT images presenting MLS caused by hemorrhages.

From these observations, we build up a heuristic model, to model the influence of the various factors on the amount of midline shift.

In our H-MLS model, each hemorrhage ***H*** is represented as an ellipse ***E*** that best fits the hemorrhage boundary (Figure 7.7). For each point ***P*** on ***E***, we trace a ray ***R*** from ***P*** along the normal direction **N** at ***P***. If ray ***R*** intersects the ***IML*** at point ***B***, it is

called an effective ray, which means it affects the deformation of the midline. Denote the intersection of effective ray ***R*** with the deformed midline (DML) as ***B'***. Extend ***R*** backward to let it intersect with ***E*** at ***P'***. Therefore, the amount of midline shift of point ***B*** is the image distance between ***B*** and ***B'***, denoted as $d = |\boldsymbol{BB'}|$.

We assume the amount of midline shift of each point ***B*** on the ***IML*** is related to the effective ray ***R*** passing through it. On each effective ray ***R***, we use $r = |\boldsymbol{PP'}|$ to measure the size of the hemorrhage, and use $s = |\boldsymbol{BP}|$ to measure the distance between the hemorrhage and the ***IML***. Let ***M*** be the middle point of the ***IML***, then $\ddot{a} = |\boldsymbol{BM}|$ measures the position of ***B*** on the ***IML***.

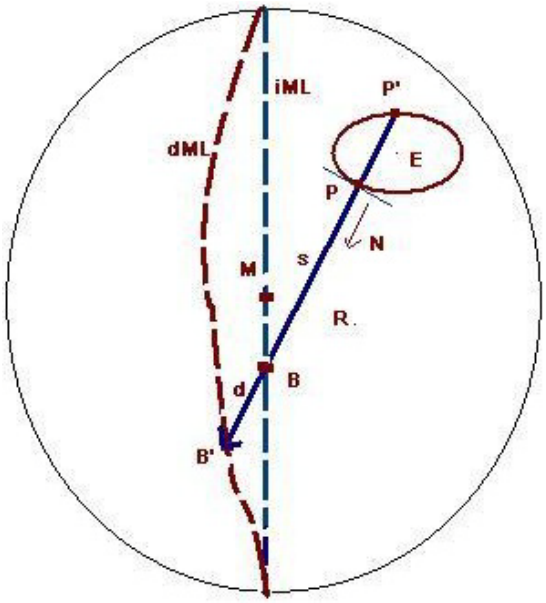

Figure 7.7. The H-MLS model.

Including an error term to handle noises, then the H-MLS model is constructed as a simple linear equation:

$$d = ar + bs + c\delta + error \tag{7.1}$$

Given a number of points ***B*** on the ***IML***, the corresponding effective ray ***R*** (thus corresponding *r*, *s*) and the amount of midline shift *d*, the coefficient *a*, *b* and *c* in Equation (7.1) can be solved using the linear regression method. Therefore, our H-MLS model is identified by a linear regression which models the relationship between intracranial hemorrhage and the MLS caused by it.

7.2.3 Study using the H-MLS model

We study the relationships between the hemorrhage and the midline by simply estimating the deformed midline based on the H-MLS model proposed in Section 7.2.2. Then we calculate the difference between the estimated midline and the ground truth midline. The study consists of three steps.

Firstly, we segment the hemorrhage using a segmentation method proposed in Chapter 5 Section 5.2.4.

Secondly, we fit an ellipse ***E*** into the boundary of the hemorrhage ***H*** segmented out in Step 1. Ray ***R*** is traced from each point ***P*** on ***E***. For each effective ray ***R***, compute the corresponding point ***B*** on ***IML***, and the corresponding *r*, *s* and *ä*. (Figure 7.7)

Thirdly, given the H-MLS model, use Equation (7.1) to compute the amount of midline shift *d* for each point ***B*** on ***IML*** which is also on the effective ray. Thus a corresponding point ***B'*** on the predicted ***DML*** is found for each ***B***. After connecting

the points ***B'*** and applying a simple curve smoothing process, we get the predicted ***DML***.

7.2.4 Experimental results

We then compare the predicted DML in previous section to the ground truth midline. Because the algorithm calculates the midline point wise, i.e., it predicts each point on the midline and forms the midline using those points, the experiments are also constructed in a point level.

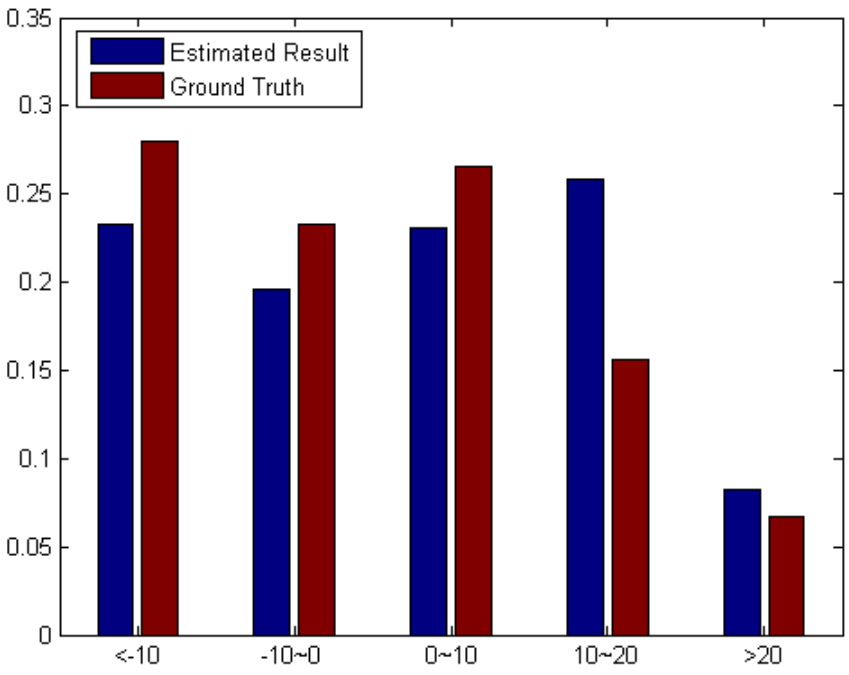

Figure 7.8. The histogram of midline points deformation distance (in pixel) distribution.

We have performed experiments on 11 CT images with 423 midline points using 10-fold cross validation. To present an overall result of all the 11 test images, a normalized histogram of the midline points deformation distance (in pixel)

distribution is shown in Figure 7.8. There are 5 bins in the histogram. Each bin indicates different distance between the estimated midline (marked ground truth midline) and the IML. Negative means the shifting direction is to the left of the IML and positive means to the right. The histograms for the ground truth and for the estimated result are generally consistent.

The parameters obtained from the regression is $d = 39.4790*r - 0.1082*s - 0.0772\delta - 0.1591$. It indicates that there is a strong relationship between the size of the hemorrhage and the midline shift distance. It also shows that the location, decided by the distance s and the position δ, has much less effect on the midline shift comparing with the size.

7.3 Summary of the Chapter

This chapter has introduced the work on brain slice indexing, and the study on hemorrhage effect.

The work on brain slice indexing[1] effectively orders and aligns the slices. The indexing is achieved using classification approach based on the anatomical features of the image. The work is useful as a preprocessing step for further processing of brain CT images. With the height level known, one can process a 2D image in a 3D level. The indexing work also helps doctors to order the slice automatically. Moreover, with the index, doctors are able to search slices within one height level in a large amount of patients.

[1] The work has been published in [Liu.R.ICIP.10]

The work on hemorrhage study[2] suggests that the linear hemorrhage effect holds. It also shows that the location has much less effect on the midline shift comparing with the size. We have also proposed this observation to doctors and it shall be studied clinically.

[2] This work is published in [Liu.R.ICIP.09]

Chapter 8

CONCLUSION

8.1 Summary of the Challenges

The main challenges of the brain midline shift quantification are three. Firstly, the midline is not a human tissue, but an imaginary center line dividing the brain normally into equal halves. Hence it cannot be segmented using its appearance. Secondly, because of noise and low contrast between soft tissues, brain tissues such as ventricles and brain matters are displayed with weakly defined boundaries. Thus it is difficult to identify the brain's anatomical structures using traditional intensity based method. Thirdly, because the traumatic brain injury is unpredictable, the damages can happen at random location of the brain with arbitrary level of severity. Thus the brain structure is arbitrarily distorted. As a result, it is problematic to design a similarity function or probabilistic atlas to cope with these unpredictable variations and abnormalities. Moreover, there is a very limited literature on midline detection.

In addition, there is a challenge on the segmentation of the brain falx. The falx appears weakly in CT images. It is hard to extract it using standard segmentation or

edge detection algorithms. No work have been reported to segment the falx in CT images according to our literature review.

8.2 Summary of Work and Contributions

Firstly, the thesis has proposes an anatomical marker model (AMM) and a novel algorithm using a candidate selection approach to automatically quantify the midline shift. The experimental results show that the proposed algorithm effectively traces and quantifies the midline shift. Compared with the only current two methods, the proposed method reduces quantification error significantly. Moreover, the run time of the proposed method outperforms current methods.

Secondly, the thesis proposes a method for segmentation of the brain falx from brain CT images using directed single connected chains (DSCC). This is the first work proposed on segmentation of brain falces.

Thirdly, the thesis proposes a probabilistic spatial relationship learning model to improve the robustness of midline shift markers detection, and of falx segmentation in brain CT images.

Fourthly, a MLS quantification measurement is proposed to complement current MLS measurement, namely, the area ratio. It also has been proposed to doctors for clinical practice.

Fifthly, the thesis proposes a patient's data retrieval system based on the MLS quantification results. Doctors are able to retrieve patients based on not only the

patients' meta information such as age, gender, and etc., but also on pathological information such as hemorrhage size, midline shift and etc..

Lastly, a fast brain indexing method is proposed. The efficient run time of the method makes method able to be embedded in online brain CT image applications as a preprocessing step.

8.3 Future Work

8.3.1 Improving the current algorithm

More sophisticated shape analysis algorithm may be also employed (a) on the skull to improve the accuracy of locating skull points ***A*** and ***B***; (b) on the ventricle regions to improve the accuracy of location candidate points ***C*** and ***D*** in the AMM model.

8.3.2 Extending the current algorithm

Further work can extend the current algorithms based on the midline traced and quantified by the proposed algorithm.

Relations between the trauma and the midline shift can be further studied. For example, during the algorithm development, we find that the size of the hemorrhage is linearly related with the midline shift distance.

The quantification results of the midline shift can be further integrated with other meta-data such as patients' gender, age and admission information. Patients' data retrieval system can be build and statistical mining can be carried out based the integration.

APPENDIX

A CT SCAN EXAMPLE

One CT scan contains multiple slices. In this appendix, we illustrate the slices of a healthy brain CT scan in axial scanning direction. The order is from bottom upwards. Hence the nasal cavity comes first, and the last one is the top of the head. The scan contains 19 slices. Each slice has dimension 512 by 512.

Slice 1

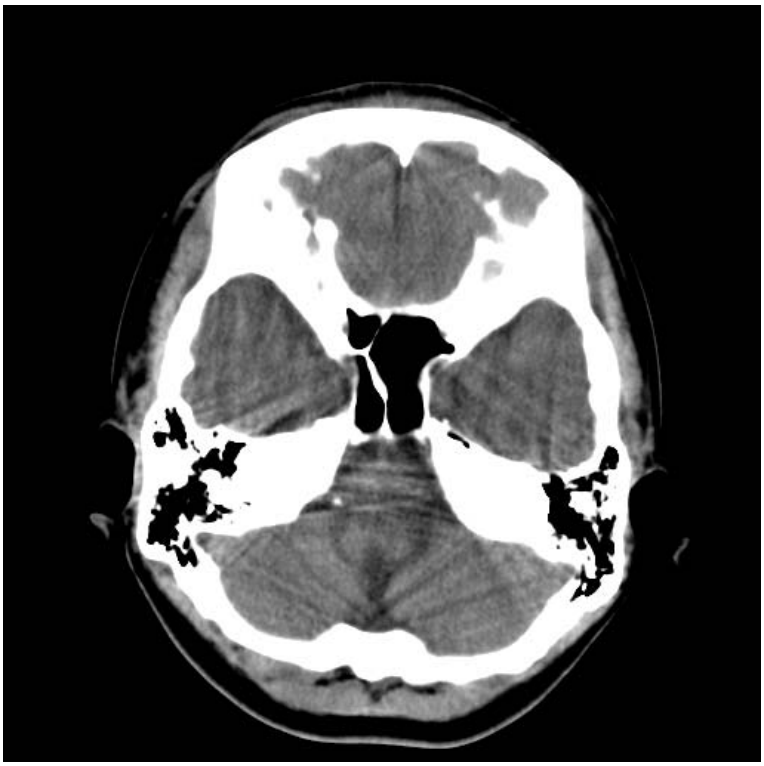

Slice 2

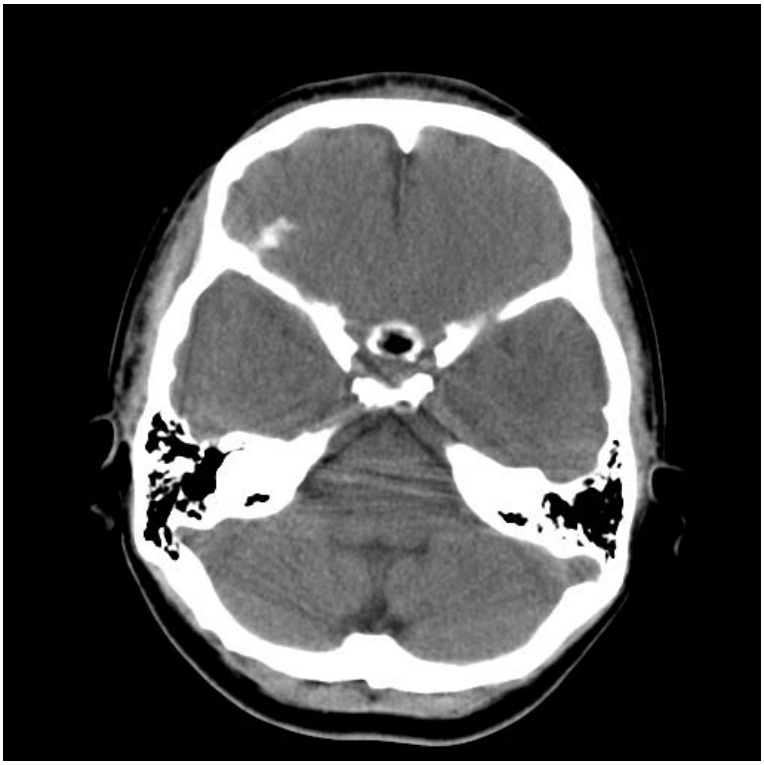

Slice 3

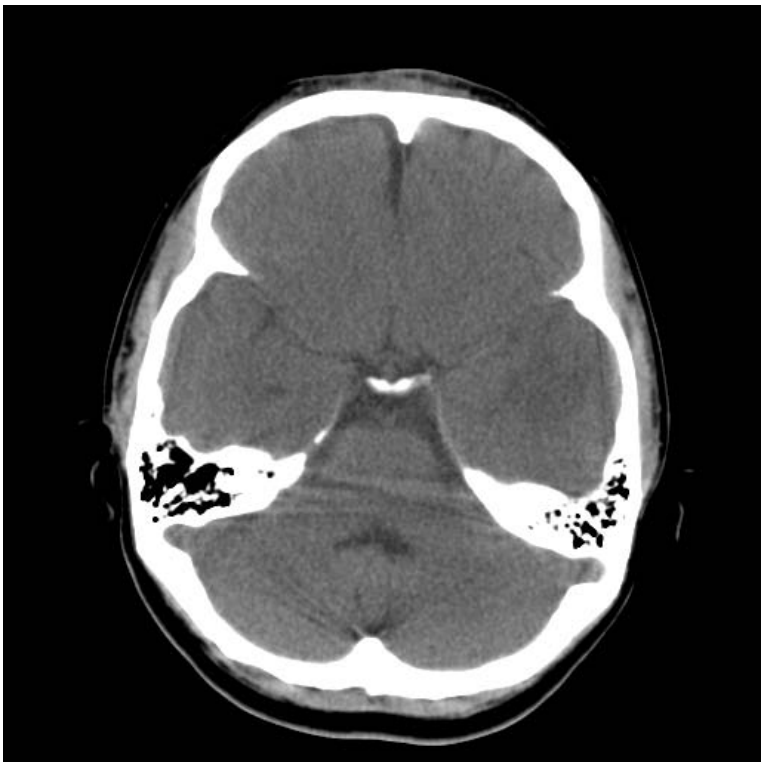

Slice 4

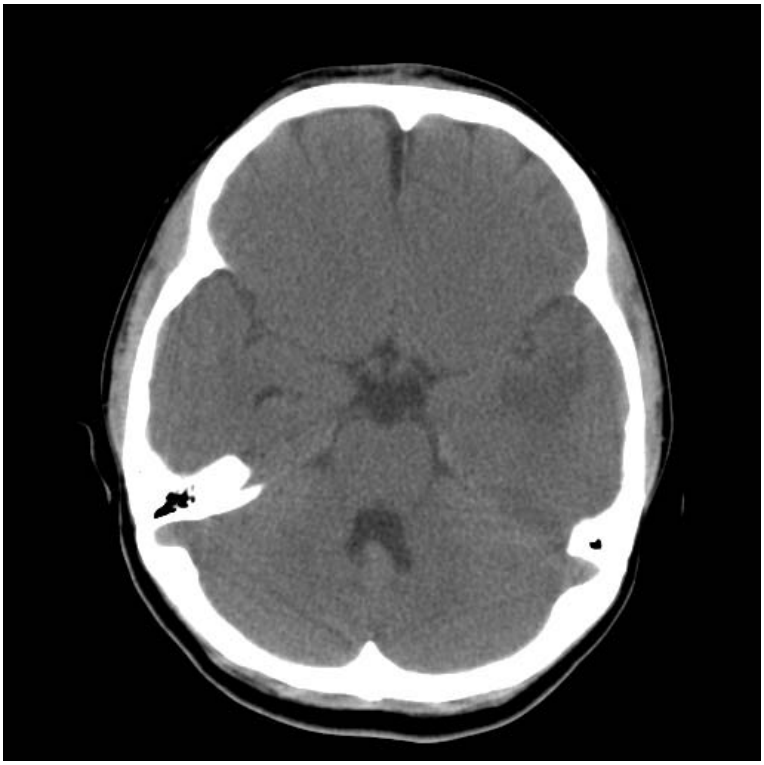

Slice 5

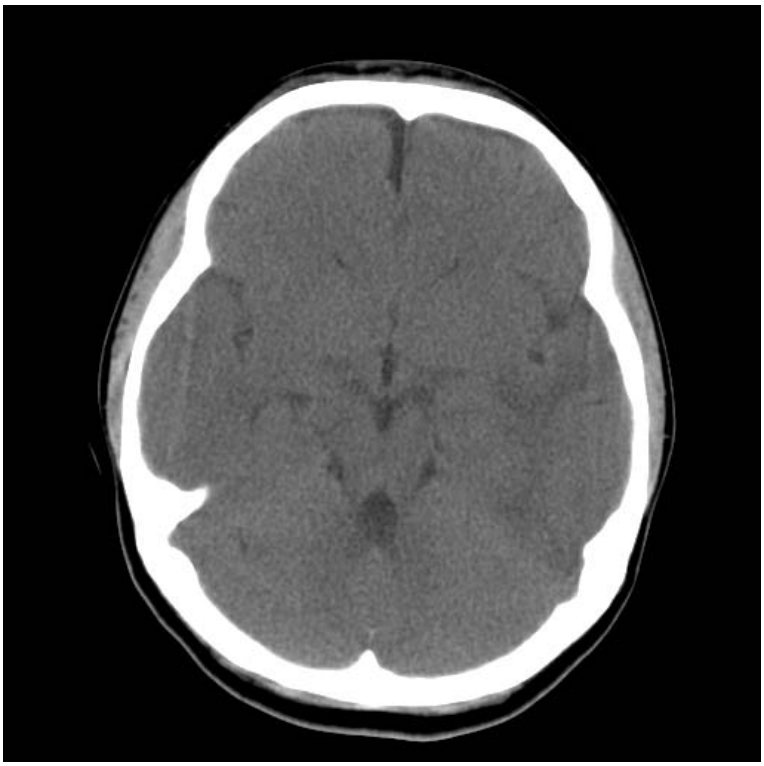

Slice 6

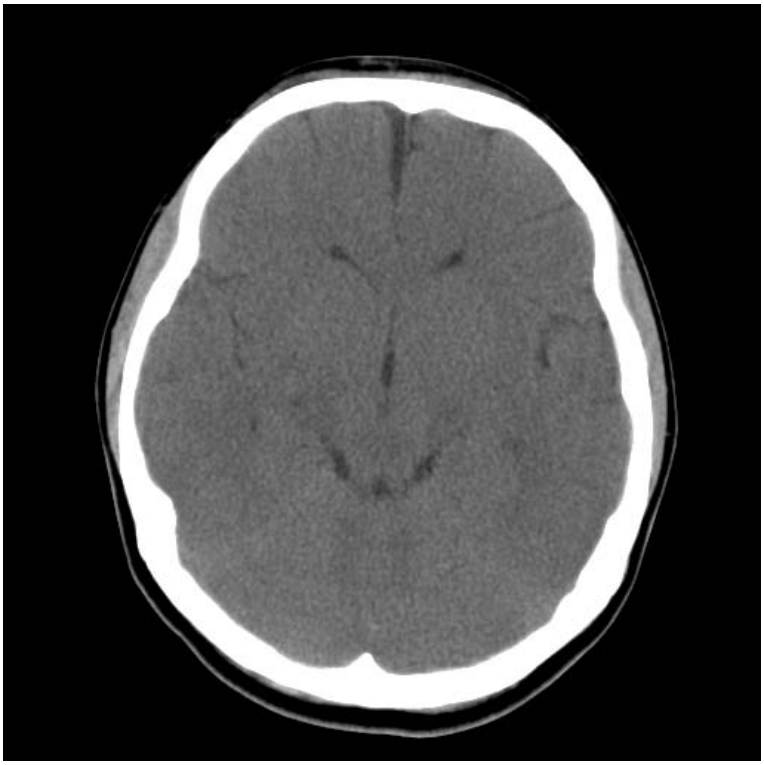

Slice 7

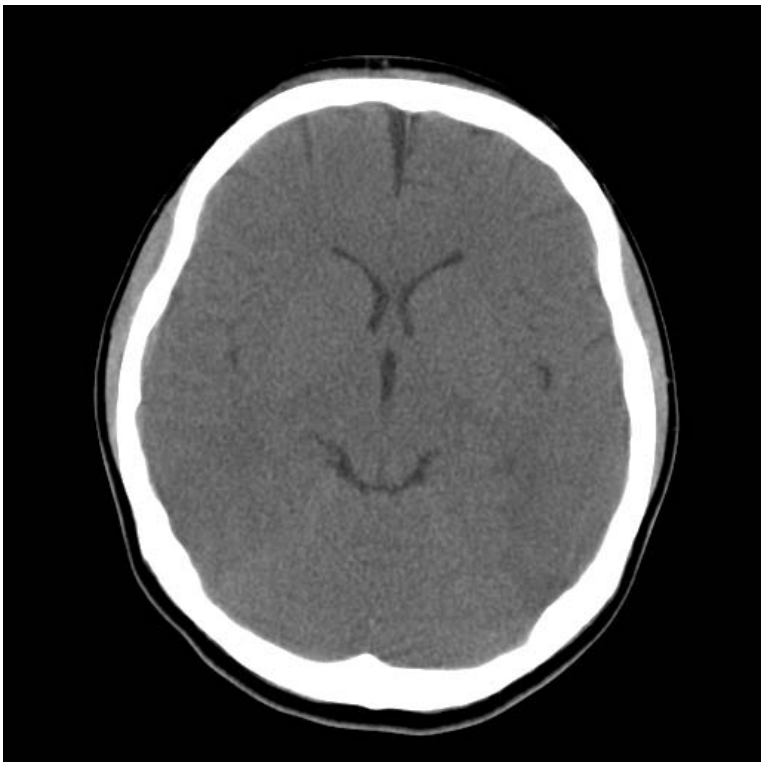

Slice 8

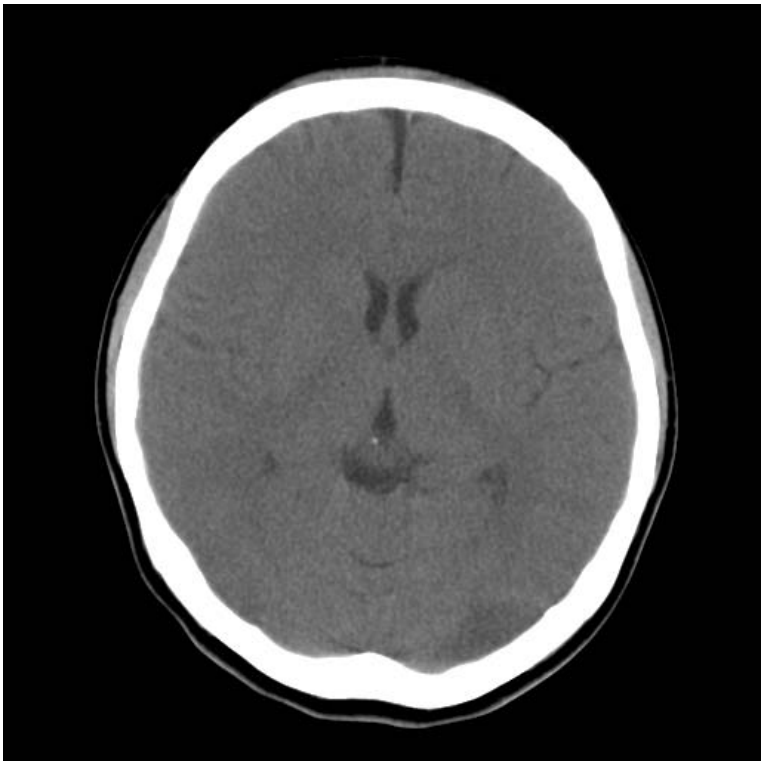

Slice 9

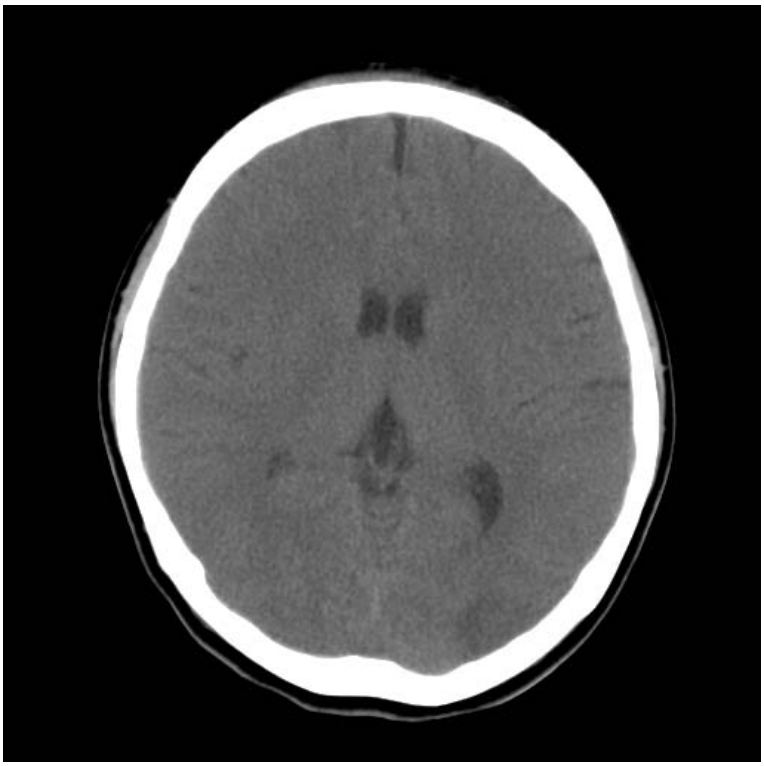

Slice 10

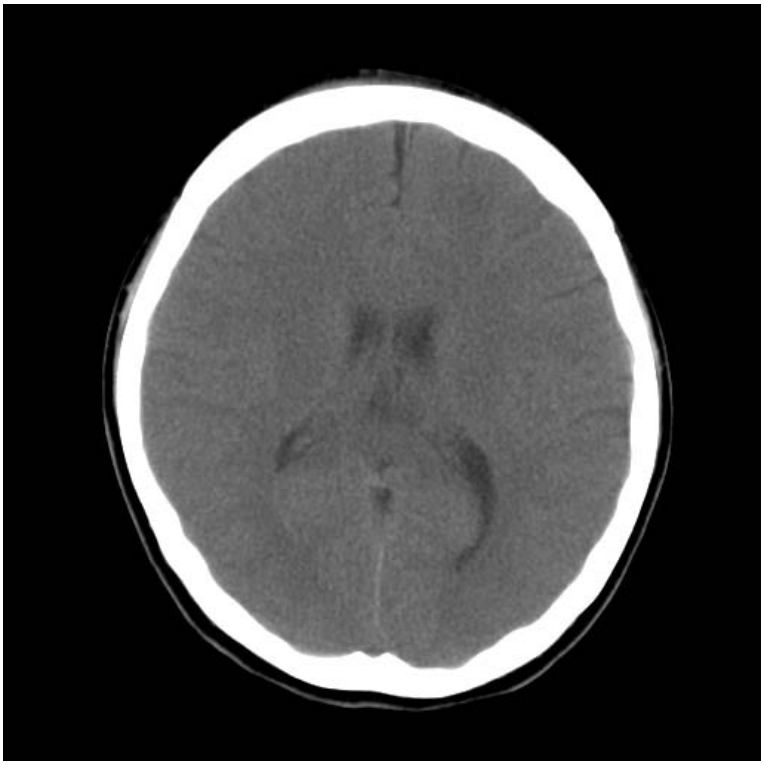

Slice 11

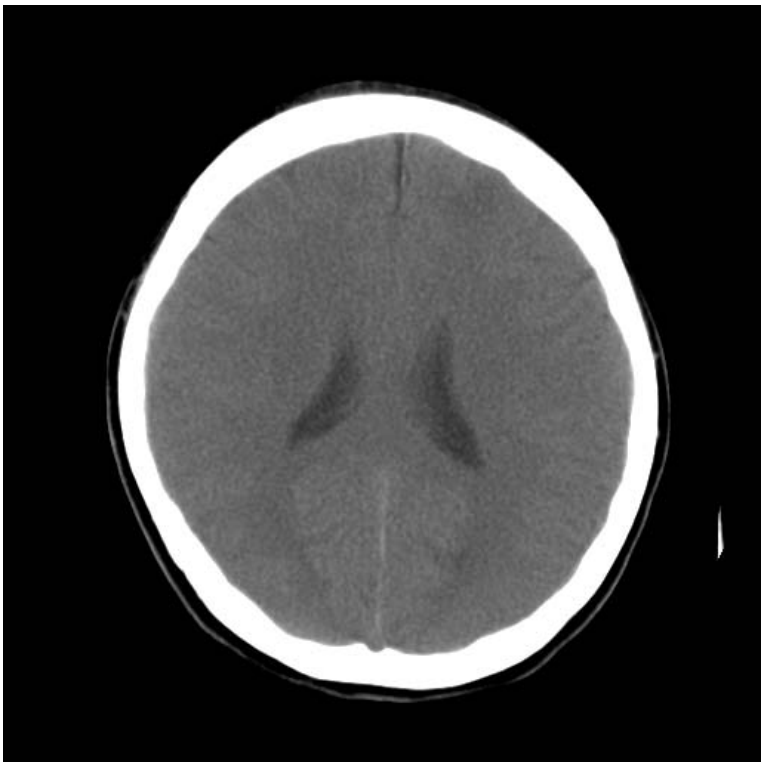

Slice 12

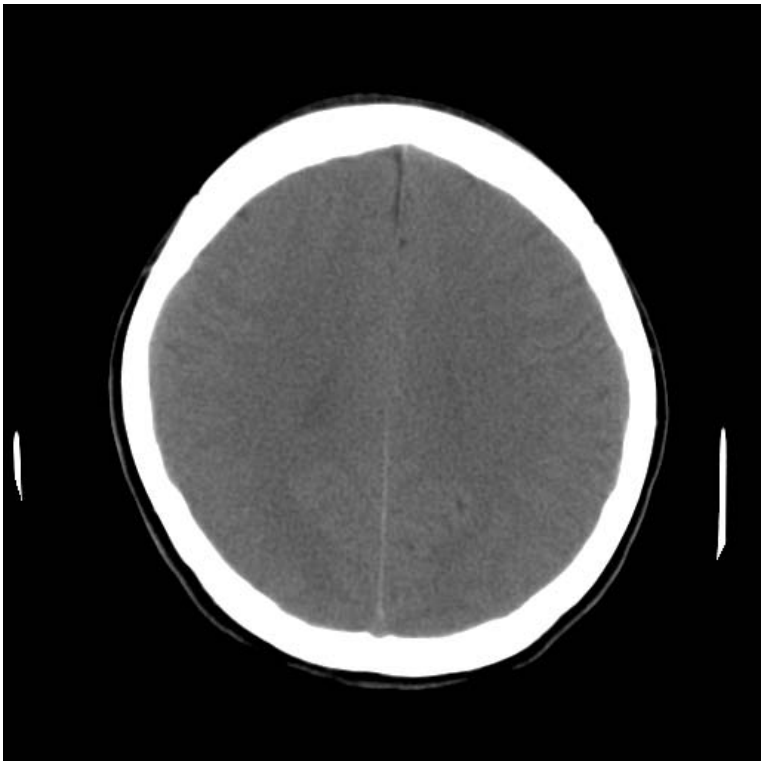

Slice 13

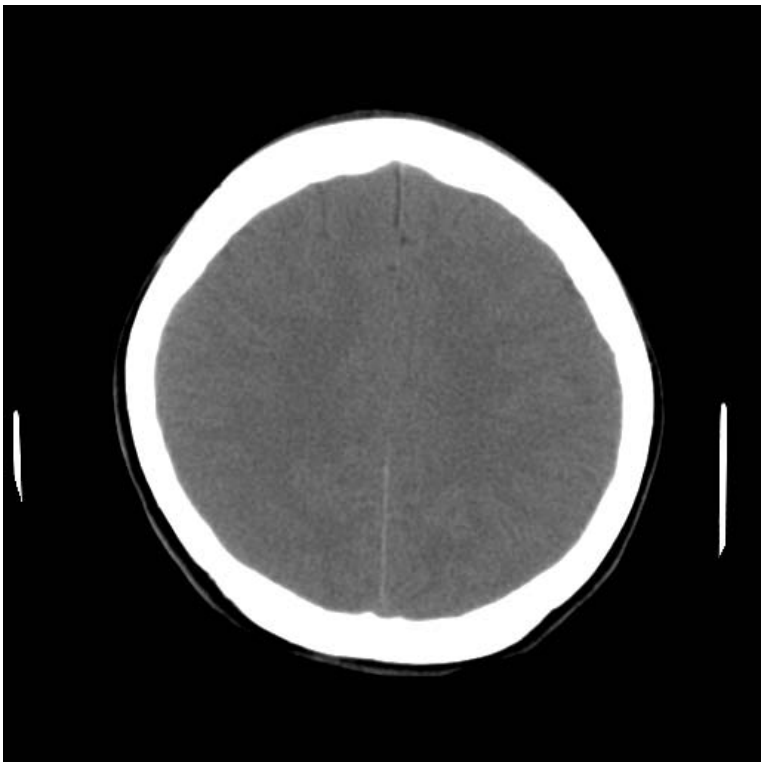

Slice 14

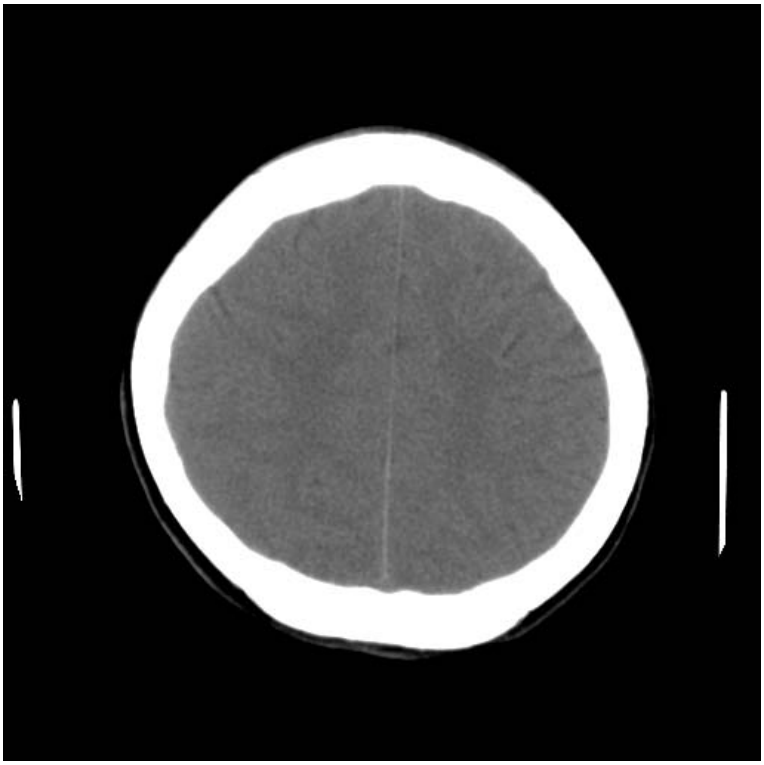

Slice 15

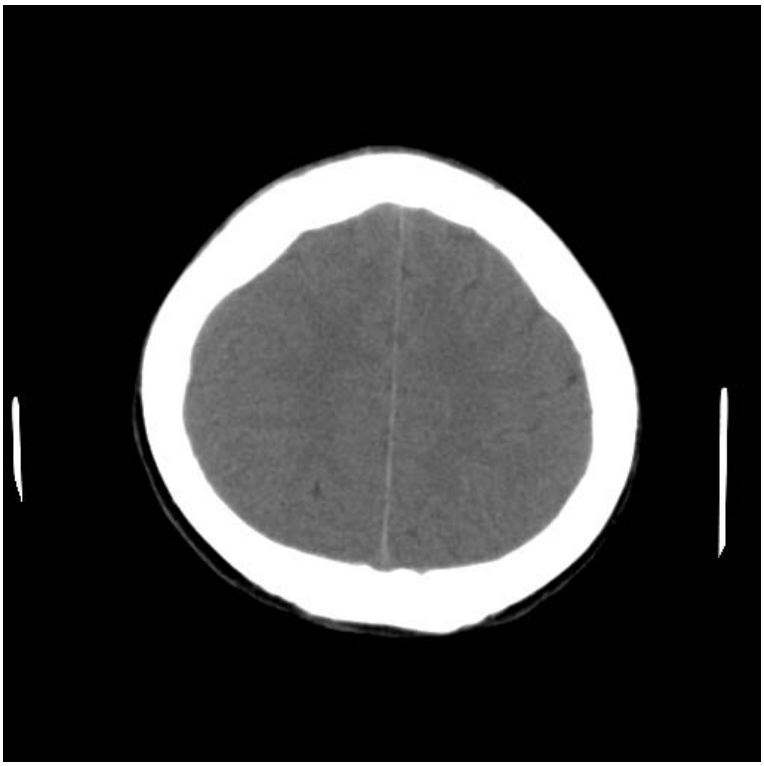

Slice 16

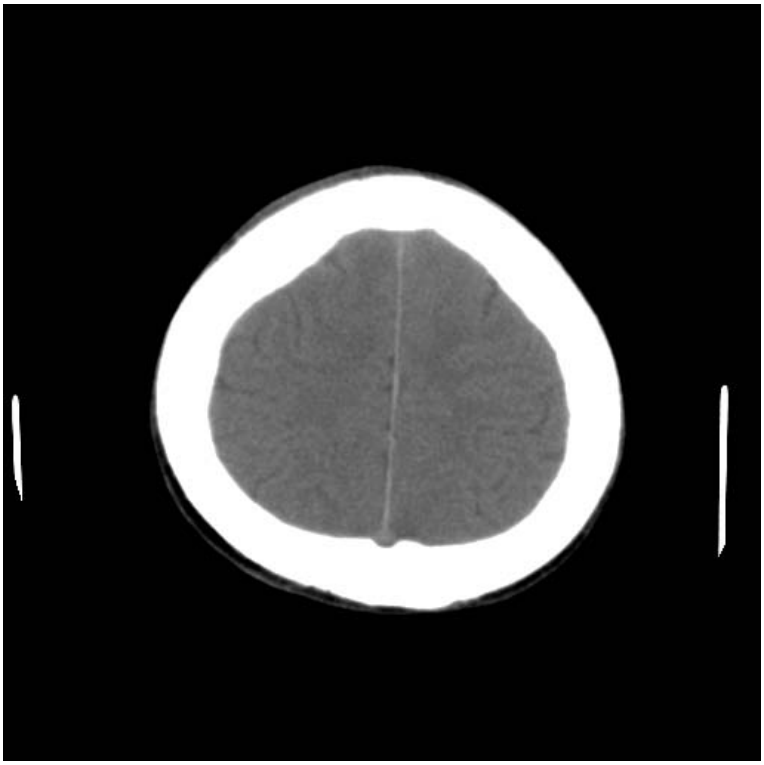

Slice 17

Slice 18

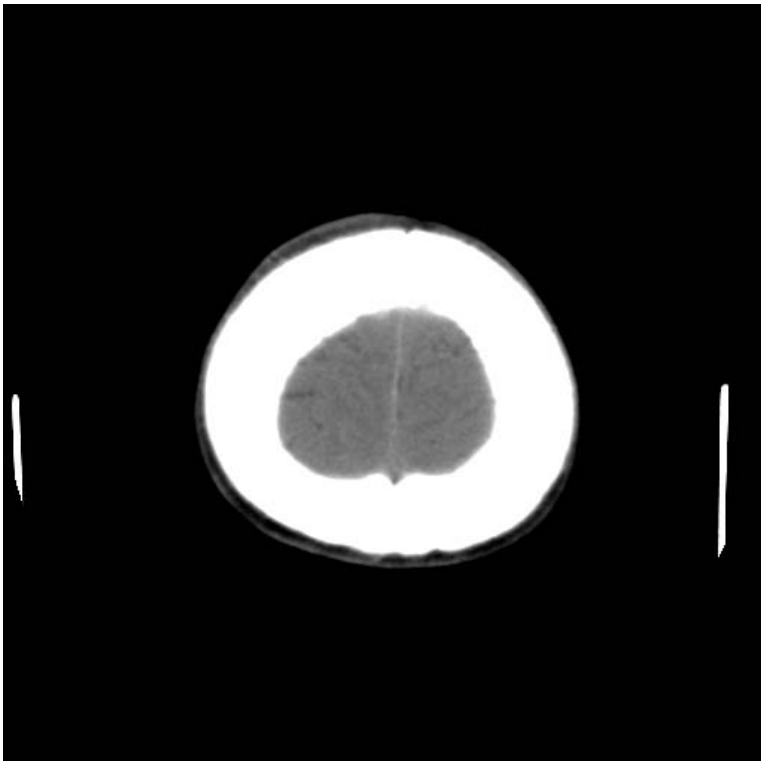

Slice 19

AUTHOR BIOGRAPHY

Liu Ruizhe is a PhD candidate in the Department of Computer Science, School of Computing, National University of Singapore. His research interests include Medical Image Processing, Analysis, and Quantification, Information Extraction and Retrieval, Computer Vision and Pattern Recognition.

During his PhD candidature, his publications include

- R. Liu, S. Li, C. L. Tan, C. K. Lee, B. C. Pang, C. C. T. Lim, Q. Tian, and Z. Zhang, "Fast traumatic brain injury CT slice indexing via anatomical feature classification", *IEEE International Conference on Image Processing (ICIP) 2010*, Hong Kong, China, 26-29 September 2010.
- R. Liu, S. Li, C. L. Tan, C. K. Lee, B. C. Pang, C. C. T. Lim, Q. Tian, and Z. Zhang, "From hemorrhage to midline shift: a new method of tracing the deformed midline in traumatic brain injury CT images", *IEEE International Conference on Image Processing (ICIP) 2009*, Cairo, Egypt, 7-10 November 2009.[1]

[1] Up to July 15th, 2011, the citation count is **2** by *google scholar*.

- R. Liu, C. L. Tan, C. K. Lee, B. C. Pang, C. C. T. Lim, Q. Tian, S. Tang, and Z. Zhang, "Hemorrhage slices detection in brain CT images", *International Conference on Pattern Recognition (ICPR) 2008*, Tampa, Florida, US, 8-11 December 2008.[2]
- R. Liu, W. Huang, and C. L. Tan, "Extraction of vectorized graphical information from scientific chart images", *International Conference on Document Analysis and Recognition (ICDAR) 2007*, Curitiba, Brazil, 23-26 September 2007.[3]
- L. Situ, R. Liu, and C. L. Tan, "Text localization in web images using probabilistic candidate selection model", *International Conference on Document Analysis and Recognition (ICDAR)* 2011, Beijing, China, 18-21 September 2011.
- S. Li, T. Gong, J. Wang, R. Liu, C. L. Tan, T. Y. Leong, B. C. Pang, C. C. T. Lim, C. K. Lee, "TBIdoc: 3D content-based CT image retrieval system for traumatic brain injury", *SPIE Medical Imaging Conference*, San Diego, CA, USA, 13-18 Feb 2010.[4]
- T. Gong, R. Liu, C. L. Tan, N. Farzad, C. K. Lee, B. C. Pang, Q. Tian, S. Tang, Z. Zhang, "Classification of CT brain images of head trauma", *2nd IAPR International Workshop on Pattern Recognition in Bioinformatics (PRIB) 2007*, Singapore, 1-2 October 2007.[5]

[2] Up to July 15th, 2011, the citation count is **8** by *google scholar*.
[3] Up to July 15th, 2011, the citation count is **2** by *google scholar*.
[4] Up to July 15th,, 2011 the citation count is **2** by *google scholar*.
[5] Up to July 15th, 2011, the citation count is **5** by *google scholar*.

BIBLIOGRAPHY

[Andrews88] B. T. Andrews, B. W. Chiles, W. L. Olsen, and L. H. Pitts, "The effect of intracerebral hematoma location on the risk of brain-stem compression and on clinical outcome", *Journal of Neurosurgery*, Vol. 69(4), pp. 518-522, 1988.

[Baillard00] C. Baillard, P. Hellier, and C. Barillot, "Segmentation of 3D brain structures using level sets and dense registration", In *Proceedings of IEEE Workshop on Mathematical Methods and Biomedical Image Analysis*, pp. 94-101, 2000.

[Barber96] C. B. Barber, D. P. Dobkin, and H. T. Huhdanpaa, "The Quickhull algorithm for convex hulls", *ACM Transactions on Mathematical Software*, Vol. 22(4), pp. 469-483, 1996.

[Barr07] R. M. Barr, A. D. Gean, T. H. Le. "Craniofacial trauma". *Fundamentals of Diagnostic Radiology*. Williams & Wilkins. pp. 69. 2007.

[Besag96] J. E. Besag, "On the statistical analysis of dirty pictures", *Journal of the Royal Statistical Society*, Vol. 48(3), pp. 259-302, 1986.

[Blissitt06] P. A. Blissitt, "Care of the critically ill patient with penetrating head injury", *Critical Care Nursing Clinics of North America*, Vol. 18(3), pp. 321-322, 2006.

[Boone07] J. M. Boone, "Radiological interpretation 2020: toward quantitative image assessment", *Medical Physics*, Vol. 34(11), pp. 4173-4179, 2007

[Bradshaw87] J. R. Bradshaw, *Brain Imaging: An Introduction*, Wright, 1987.

[Burtscher05] M. Burtscher and I. Szezyrba, "Numerical modeling for brain dynamics in traumatic situations – impulsive translations", *In Proceedings of International Conference on Mathematics and Engineering Techniques in Medicine and Biological Sciences (METMBS) 2005*, pp. 205-211, 2005.

[Canny86] J. Canny, "A computational approach to edge detection", *IEEE Transactions on Pattern Analysis and Machine Intelligence*, Vol. 8(6), pp.679-698, 1986.

[Chan07] T. Chan, "Computer aided detection of small acute intracranial hemorrhage on computer tomography of brain", *Computerized Medical Imaging and Graphics*, Vol. 7(4-5), pp. 285-298, June-July 2007.

[Chapman99] S. B. Chapman, H. S. Levin, and S. L. Lawyer, "Communication problems resulting from brain injury in children: special issues of assessment and management", *Communication Disorders Following Traumatic Brain Injury*, pp. 235-236, Psychology Press, 1999.

[Chen09] W. Chen and K. Najarian, "Segmentation of ventricles in brain CT images using Gaussian mixture model method", *In Proceedings of IEEE International Conference on Complex Medical Engineering*, pp. 15-20, April 2009.

[Chen10] W. Chen, K. Najarian, and K. Ward, "Actual midline estimation from brain CT scan using multiple regions shape matching", *In Proceedings of International Conference on Pattern Recognition (ICPR) 2010*, pp. 2552-2555, 2010.

[Chui92] C. K. Chui, *An Introduction to Wavelets*, Academic Press Inc., New York, 1992.

[Collins02] C. Collins, and J. Dean, "Acquired brain injury", *Occupational Therapy and Physical Dysfunction: Principles, Skills and Practice*, pp. 395-396, Churchill Livingstong, 2002.

[Cotter02] C. S. Cotter, P. K. Smolarkiewicz, and I. N. Szczyrba, "A viscoelastic fluid model for brain injuries", *International Journal for Numerical Methods in Fluids*, Vol. 40, pp. 303-311, 2002.

[Daniel08] C. Danial and C. Sullivan, "Imaging as a quantitative science", *Radiology*, Vol. 248(2), pp. 328-332, 2008.

[Deleo85] J. M. Deleo, M. Schwartz, H. Creasey, N. Cutler, and S. I. Rapoport, "Computer-assisted categorization of brain computerized tomography pixels into cerebrospinal fluid, white matter, and gray matter", C*omputer and Biomedical Research*, Vol. 18, pp. 79-88, 1985.

[Dempster77] A. P. Dempster, N. M. Laird, and D. B. Rubin, "Maximum likelihood from incomplete data via the EM algorithm", *Journal of the Royal Statistical Society*, Vol. 39(1), pp. 1-38, 1977.

[Dowine] A. Dowine, *Tutorial CT: in Head Trauma*, http://www,radiology.co.uk/srs-x/tutors/cttrauma/tutor.htm

[Duda72] R. O. Duda and P. E. Hart, "Use of the Hough transformation to detect lines and curves in pictures", *Communications of the ACM*, Vol. 15(1), pp.11-15, 1972.

[Element] *Introduction to the brain* http://www.elementssupportservices.com/InfoSheets/introduction-to-the-brain.html

[Fisher25] R. A. Fisher, *Statistical Methods for Research Workers*, Edinburgh: Oliver and Boyd, 1925.

[Fitzgibbon99] A. Fitzgibbon, M. Pilu, and R. B. Fisher, "Directed least square fitting of ellipses", *IEEE Transactions on Pattern Analysis and Machine Intelligence*, Vol. 21, pp. 476-480, 1999.

[Forsyth02] D. A. Forsyth and J. Ponce, *Computer Vision: A Modern Approach*, Prentice Hall, 2002.

[Gefen08] S. Gefen, N. Kiryati, and J. Nissanov, "Atlas-based indexing of brain sections via 2-D to 3-D image registration", *IEEE Transactions on Journal of Biomedical Engineering*, Vol. 55(1), pp. 147-156, Jan 2008.

[Gong.T.PRIB.07] T. Gong, R. Liu, C. L. Tan, N. Farzad, C. K. Lee, B. C. Pang, Q. Tian, S. Tang, Z. Zhang, "Classification of CT brain images of head trauma", *2nd IAPR International Workshop on Pattern Recognition in Bioinformatics (PRIB) 2007*, Singapore, 1-2 October 2007.

[Greenspan06] H. Greenspan, A. Ruf, and J. Goldberger, "Constrained Gaussian mixture model framework for automatic segmentation of MR brain images", *IEEE Transactions on Medical Imaging*, Vol. 25(9), pp. 1233-1245, 2006.

[Gruen02] P. Gruen, "Surgical management of head trauma", *Neuroimaging Clinics of North America*, Vol. 12, pp. 339-343, 2002.

[Haar10] A. Haar, "Zur theorie der orthogonalen funktionensysteme", *Mathematische Annalen*, Vol. 69(3), pp. 331-371, 1910.

[Han07] X. Han and B. Fischl, "Atlas renormalization for improved brain MR image segmentation across scanner platforms", *IEEE Transactions on Medical Imaging*, Vol. 26, pp. 479-486, 2007.

[Hannay04] H. J. Hannay, D. B. Howieson, D. W. Loring, J. S. Fischer, and M. D. Lezak, "Neuropathology for neuropsychologists", *Neuropsychological Assessment*, pp. 159-162, Oxford University Press.

[Hara07] T. Hara, N. Matoba, X. Zhou, S. Yokoi, H. Aizawa, H. Fujita, K. Sakashita, and T. Matsuoka, "Automated detection of extradural and subdural hematoma for content-enhanced CT images in emergency medical care", *In Proceedings of SPIE*, 2007.

[Haralick73] R. M. Haralick, K. Shanmugam, and I. Dinstein, "Textual features for

image classification", *IEEE Transactions on Systems, Man, and Cybernetics*, Smc-3(6), pp. 610-621, 1973.

[Holden10] M. Holden, J. A. Schnable, and D. L. G. Hill, "Quantifying small changes in brain ventricular volume using non-rigid registration", *Lecture Notes on Computer Science*, Vol. 2208, pp. 49-56, 2010.

[Hossam07] E. Hossam, A. E. Munim, and A. A. Farag, "Curve/surface representation and evolution using vector level sets with application to the shape-based segmentation problem", *IEEE Transactions on Pattern Analysis and Machine Intelligence*, Vol. 29(6), pp. 945-957, 2007.

[Hu05] Q. Hu, G. Qian, A. Aziz, and W. L. Nowinski, ""Segmentation of brain from computed tomography head images", *IEEE Engineering in Medicine and Biology Society*, pp. 3375-3378, 2005.

[Huang99] H. K. Huang, *PACS: Basic Principles and Applications*, Wiley-Liss Inc, Canada, 1999.

[Huang07] J. Huang, X. Huang, D. Metaxas, and L. Axel, "Adaptive metamorphs model for 3D medical image segmentation", In Proceedings of International Conference on Medical Image Computing and Computer-Assisted Intervention (MICCAI) 2007, pp. 302-310, 2007.

[Jackson98] P. Jackson, *Introduction to Expert Systems*, 3rd edition, Addison-Wesley, 1998.

[Jennett98] B. Jennett, "Epidemiology of head injury", *Archives of Disease in Childhood*, Vol. 78(5), pp. 403-406, 1998.

[Jolliffe02] I. T. Jolliffe, *Principle Component Analysis, Springer Series in Statistics*, 2nd edition, 2002.

[Kass88] M. Kass, A. Witkin, and D. Terzopoulos, "Snakes: active contour models", *International Journal of Computer Vision*, pp. 321-331, 1988.

[Kaus01] M. R. Kaus, S. K. Warfield, A. Nabavi, P. M. Black, F. A. Jolesz, and R. Kikinis, "Automated segmentation of MR images of brain tumors", *Radiology*, Vol. 218, pp. 586-591, 2001.

[Kenney62] J. F. Kenney and E. S. Keeping, *Mathematics of Statistics*, 3rd edition, Princeton, 1962.

[Kim00] T. S. Kim, M. Singh, W. Sungkarat, C. Zarow, and H. Chui, "Automatic registration of postmortem brain slices to MRI reference volume", *IEEE Transactions on Nuclear Science*, Vol. 47(4), pp. 1607-1613.

[Knaus85] W. A. Knaus, E. A. Draper, D. P. Wagner, and J. E. Zimmerman, "APACHE II: a severity of disease classification system", *Critical Care Medicine*, Vol. 13, pp. 818-829, 1985.

[Knaus91] W. A. Knaus, D. P. Wagner, E. A. Draper, J. E. Zimmerman, M. Bergner, P. G. Bastos, C. A. Sirio, D. J. Murphy, T. Lotring, and A. Damiano, "The APACHE III prognostic system. Risk prediction of hospital mortality for critically ill hospitalized adults", *Chest*, Vol. 100(6), pp. 1619-1636, 1991.

[Kyriacou02] S. K. Kyriacou, A. Mohamed, K. Miller, and S. Neff, "Brain mechanics for neurosurgery: modeling issues", *Biomechanics and Modeling in Mechanobiology*, Vol. 1(2), pp. 151-164, 2002.

[Lauric07] A. Lauric, and S. Frisken, "Soft segmentation of CT brain data", *Technical Report TR-2007-3*, Turfs University, MA, 2007.

[Li95] H. Li, R. Deklerck, B. D. Cuyper, A. Hermanus, E. Hyssen, and J. Cornelis, "Object recognition in brain CT-scans: knowledge-based fusion of data from multiple feature extractions", *IEEE Transactions on Medical Imaging*, Vol. 14(2), pp. 212-229, 1995.

[Li.S.SPIE.10] S. Li, T. Gong, J. Wang, R. Liu, C. L. Tan, T. Y. Leong, B. C. Pang, C. C. T. Lim, C. K. Lee, "TBIdoc: 3D content-based CT image retrieval system for traumatic brain injury", *SPIE Medical Imaging Conference*, San Diego, CA, USA, 13-18 Feb 2010.

[Liao06] C. C. Liao, I. J. Chiang, F. Xiao, and J. M. Wong, "Tracing the deformed midline on brain CT", *Biomedical Engineering – Applications, Basis, and Communications*, Vol. 18, pp. 305-311, 2006.

[Liao10] C. C. Liao, F. Xiao, J. M. Wong, and I. J. Chiang, "Automatic recognition of midline shift on brain CT images", *Computers in Biology and Medicine*, Vol. 40(3), pp. 331-339, Mar 2010.

[Lin00] E. Lin, 頭部 CT 的判讀 (*Interpretation of Brain CT*), http://www.oocities.org/~dr_ericlin/ct_read/00_content.html

[Liu01] Y. Liu, R. Collins, and W. Rothfus, "Robust midsagittal plane extraction from normal and pathological 3D neuroradiology images", *IEEE Transactions on Medical Imaging*, Vol. 20, pp. 175-192, 2001.

[Liu04] Y. Liu, N. A. Lazar, W. E. Rothfus, F. Dellaert, A. Moore, J. Schneider, and T. Kanade, "Semantic-based biomedical image indexing and retrieval", *Trends and Advances in Content-based Image and Video Retrieval*, Shapiro, Kriege, and Veltkamp, edited, Feb 2004.

[Liu97] Y. Liu, W. E. Rothfus, and T. Kanade, "Content-based 3D neuroradiologic image retrieval: preliminary results", *IEEE Content-based Video and Image Retrieval Workshop Associated with CVPR97*, June 1997.

[Liu.J04] J. Liu, N. Pagoulatos, and Y. Kim, "Ultrasound spatial compounding via registration of 2D slices into 3D volume", In Proceedings of *IEEE International Ultrasonics, Ferroelectries, and Frequency Control Joint 50th Anniversary Conference*, 2004.

[Liu,Jm07] J. Liu, S. Huang, A. Aziz, and W. L. Nowinski, "Three dimensional digital atlas of the orbit constructed from multi-modal radiological images", *International Journal on Computer Assisted Radiological Surgery*, Vol. 1(5), pp. 275-283, 2007.

[Liu.Jm08] J. Liu, S. Huang, and W L. Nowinski, "A hybrid approach for segmentation of anatomic structures in medical images", International Journal on Computer Assisted Radiological Surgery, Vol. 3(3-4), pp. 213-219, 2008.

[Liu.Jm08(2)] J. Liu, W. Gao, S. Huang, and W. L. Nowinski, "A model-based, semi-global segmentation approach for automatic 3D point landmarks localization in neuroimages", *IEEE Transactions on Medical Imaging*, Vol. 27, pp. 1034-1044, 2008.

[Liu.Jm09] J. Liu, S. Huang, and W. L. Nowinski, "Automatic segmentation of the human brain ventricles in MR images by knowledge-based region growing and trimming", *Neuro -informatics*, Vol. 7, pp. 131-136, 2009.

[Liu.Jm10] J. Liu, S. Huang, I. Volkau, W. Ambrosius, L. C. Lee, and W. L. Nowinski, "Automatic model-guided segmentation of the human brain ventricular system from CT images", Academic Radiology, Vol. 17(6), pp. 718-726, 2010.

[Liu.R.ICDAR.07] R. Liu, W. Huang, and C. L. Tan, "Extraction of vectorized graphical information from scientific chart images", *International Conference on Document Analysis and Recognition (ICDAR) 2007*, Curitiba, Brazil, 23-26 September 2007.

[Liu.R.ICPR08] R. Liu, C. L. Tan, C. K. Lee, B. C. Pang, C. C. T. Lim, Q. Tian, S. Tang, and Z. Zhang, "Hemorrhage slices detection in brain CT images", *International Conference on Pattern Recognition (ICPR) 2008*, Tampa, Florida, US, 8-11 December 2008.

[Liu.R.ICIP09] R. Liu, S. Li, C. L. Tan, C. K. Lee, B. C. Pang, C. C. T. Lim, Q. Tian, and Z. Zhang, "From hemorrhage to midline shift: a new method of tracing the deformed midline in traumatic brain injury CT images", *IEEE International Conference on Image Processing (ICIP) 2009*,

Cairo, Egypt, 7-10 November 2009.

[Liu.R.ICIP10] R. Liu, S. Li, C. L. Tan, C. K. Lee, B. C. Pang, C. C. T. Lim, Q. Tian, and Z. Zhang, "Fast traumatic brain injury CT slice indexing via anatomical feature classification", *IEEE International Conference on Image Processing (ICIP) 2010*, Hong Kong, China, 26-29 September 2010.

[Loncaric97] S. Loncaric and K. Domagoj, "A method for segmentation of CT head images", *Lecture Notes in Computer Science*, Vol. 1311, pp. 388-395, 1997.

[Maas05] A. I. R. Maas, C. W. P. M. Hukkelhoven, L. F. Marshall, E. W. Steyerberg, A. B. Valadka, R. Bullock, D. W. Marion, J. H. Huang, N. Ranalli, E. L,. Zager, and J. E. Wilberger, "Prediction of outcome in traumatic brain injury with computed tomographic characteristics: a comparison between the computed tomographic classification and combinations of computed tomographic predictors", *Neurosurgery*, Vol. 57(6), pp. 1173-1182, 2005.

[Maas08] A. I. Maas, N. Stocchetti, and R. Bullock, "Moderate and severe traumatic brain injury in adults", *The Lancet Neurology*, Vol. 7, 2008.

[MacQueen67] J. B. MacQueen, "Some methods for classification and analysis of multivariate observations", *In Proceedings of 5th Berkeley Symposium on Mathematical Statistics and Probability*, pp. 281-297, 1967

[Maksimovic00] R. Maksimovic, S. Stankovic, and D. Milovanovic, "Computed tomography image analyzer: 3D reconstruction and segmentation applying active contour models – 'snakes'", *International Journal of Medical Informatics*, Vol. 58-59, pp. 29-37, 2000.

[Mallat89] S. G. Mallat, "A theory for multiresolution signal decomposition: the wavelet representtaion", *IEEE Transactions on Pattern Analysis and Machine Intelligence*, Vol. 11, pp. 674-693, 1989.

[Marshall91] L. F. Marshall, S. B. Marshall, M. R. Klauber, M. V. B. Clark, H. M. Eisenberg, J. A. Jane, T. G. Luerssen, A. Marmarou, and M. A. Foulkes, "A new classification of head injury based on computerized tomography", *Journal of Neurosurgery*, Vol. 75, pp. 14-20, 1991.

[McCaffrey97] R. J. McCaffrey, "Special issues in the evaluation of mild traumatic brain injury", *The Practice of Forensic Neuropsychology: Meeting Challenges in the Courtroom*, pp. 71-75, Plenum Press.

[Mitchell97] T. M. Mitchell, *Machine Learning*, McGraw Hill, 1997.

[Moons09] K. G. Moons, P. Royston, Y. Vergouwe, D. E. Grobbee, and D. G. Altman, “Prognosis and prognosis research: what, why and how?”, *BMJ*, Vol. 23, pp. 338-375, 2009.

[Müller04] H. Müller, N. Michoux, D. Bandon, B. David, and A. Geissbuhler, “A review of content-based image retrieval system in medical applications – clinical benefits and future directions”, *International Journal of Medical Informatics*, Vol. 73(1), pp. 1-23, Feb 2004.

[NEMA] DICOM official website: http://medical.nema.org/

[Orlando04] *Overview of Adult Traumatic Brain Injuries – Self Learning Packet*, Copyright by Orlando Regional Healthcare, Education and Development, 2004.

[Orrison95] W. W. Orrison, J. D. Lewine, J. A. Sanders, and M. F. *Hartshorne, Function Brain Imaging*, Mosby, 1995.

[Pang02] B. C. Pang and H. Yin, “Analysis of clinical criterion for ‘talk and deteriorate’ following minor head injury using different data mining tools”, *Journal of Neurotrauma*, National Neurotrauma Society, Gainesville, Florida, USA, in press.

[Parikh07] S. Parikh, M. Koch, and R. K. Narayan, “Traumatic brain injury”, *International Anesthesiology Clinics*, Vol. 45(3), pp. 119-135, 2007.

[Parizel01] P. M. Parizel, S. Makkat, E. V. Miert, J. W. V. Goethem, L. V. D. Hanwe, and A. M. D. Schepper, “Intracranial hemorrhage: principles of CT and MRI interpretation”, *Neuroradiology*, Vol. 11, pp. 1770-1783, 2001.

[Pham99] D. L. Pham and J. L. Prince, “Adaptive fuzzy segmentation of magnetic resonance images”, *IEEE Transactions on Medical Imaging*, Vol. 15, pp. 429-442, 1999.

[Pham00] D. L. Pham, C. Xu, and J. L. Prince, “Current methods in medical image segmentation”, *Annual Review of Biomedical Engineering*, Vol. 2, pp. 315-337, 2000.

[Pluim03] J. P. W. Pluim, J. B. A. Maintz, and M. A. Viergever, “Mutual-information-based registration of medical images: a survey”, *IEEE Transactions on Medical Imaging*, Vol. 22(8), pp. 986-1004, Aug 2003.

[Prima02] S. Prima, S. Ourselin, and N. Ayache, “Computation of the mid-sagittal plane in 3D brain images”, *IEEE Transactions on Medical Imaging*, Vol. 21(2), pp. 122-138, 2002.

[Provost00] F. Provost, "Learning with imbalanced data sets 101." *Invited paper for the AAAI'2000 Workshop on Imbalanced Data Sets*.

[Pun81] T. Pun, "Entropic thresholding, a new approach", *Computer Graphics and Image Processing*, Vol. 16, pp. 210-239, 1981.

[Quattrocchi91] K. B. Quattrocchi, P. Prasad, N. H. Willitsm, and F. C. Wagner, "Quantification of midline shift as a predictor of poor outcome following head injury", *Surgical Neurology*, Vol. 35, pp. 183-188, 1991.

[Ramachandran80] K. Ramachandran, "A coding method for vector representation of engineering drawings", In *Proceedings of IEEE*, Vol. 68(7), pp. 813-817, 1980.

[Ross89] D. A. Ross, W. L. Olsen, A. M. Ross, B. T. Andrews, and L. H. Pitts, "Brain shift, level of consciousness, and restoration of consciousness in patients with acute intracranial hematoma", *Journal of Neurosurgery*, Vol. 71(4), pp. 498-502, 1989.

[Ruttimann93] U. E. Ruttimann, E. M. Joyce, D. E. Rio, and M. J. Eckardt, "Fully automated segmentation of cerebrospinal fluid in computed tomography", *Psychiatry Research: Neuroimaging*, Vol. 50, pp. 101-119.

[Schnack01] H. G. Schnack, P. H. E. Hulshoff, W. F. C. Baare, M. A. Viergever, and R. S. Kahn, "Automatic segmentation of ventricular system from MR images of the human brain", *Neuroimage*, Vol. 14, pp. 95-104, 2001.

[Shen01] D. Shen, E. H. Herskovits, and C. Davatzikos, "An adaptive- focus statistical shape model for segmentation and shape modeling of 3-D brain structure", *IEEE Transactions on Medical Imaging*, Vol. 20, pp. 257-270, 2001.

[Shyu02] C. R. Shyu, C. Pavlopoulou, A. C. Kak, and C. E. Brodley, "Using human perceptual categories for content-based retrieval from a medical image database", *Computer Vision and Image Understanding*, Vol. 88, pp. 119-151, 2002.

[Silver05] J. M. Silver, T. W. Mcallister, and S. C. Yodufsky, *Textbook of traumatic brain injury*, Washington D. C, Amedican Psychiatric Association, 2005

[Situ.L.ICDAR11] L. Situ, R. Liu, and C. L. Tan, "Text localization in web images using probabilistic candidate selection model", *International Conference on Document Analysis and Recognition (ICDAR)* 2011, Beijing, China, 18-21 September 2011.

[Smeulders00] A. W. M. Smeulders, M. Worring, S. Santini, A. Gupta, and R. Jain, "Content-based image retrieval at the end of the early years", *IEEE Transactions on Pattern Analysis and Machine Intelligence*, Vol.

22(12), pp. 1-32, 2000.

[Sonka96] M. Sonka, S. K. Tadikonda, and S. M. Collins, “Knowledge- based interpretation of MR brain images”, *IEEE Transactions on Medical Imaging*, Vol. 15, pp. 443-452, 1996.

[Studholme99] C. Studholme, D. L. G. Hill, and D. J. Hawks, “An overlap invariant entropy measure of 3D medical image alignment”, *Pattern Recognition*. Vol. 32, pp. 71-86, 1999.

[Sucu06] H. K. Sucu, F. Gelal, M. Gokmen, F. D. Ozer, and S. Tektas, “Can midline brain shift be used as a prognostic factor to predict postoperative restoration of consciousness in patients with chronic subdural hematoma?”, *Surgical Neurology*, Vol. 66, pp. 178-182, 2006.

[Szeliski10] R. Szeliski, *Computer Vision Algorithms and Applications*, Springer, 2010.

[Trucco98] E. Trucco and A. Verri, *Introductory Techniques for 3-D Computer Vision*, Prentice Hall, 1998.

[Valadka04] A. B. Valadka, “Injury to the cranium”, *Trauma*, McGraw-Hill, pp. 385-406, 2004.

[Volkau06] I. Volkau, K. N. B. Prakash, A. Anand, A. Aziz, and W. L. Nowinski, “Extraction of the midsagittal plane from morphological neuroimages using the Kullback-Leibler’s measure”, *Medical Image Analysis*, Vol. 10, pp. 863-874, 2006.

[Whitley93] D. Whitley, “A genetic algorithm tutorial”, *Technical Report CS-93-103*. Department of Computer Science, Colorado State University, Boulder, 1993.

[Worth98] A. J. Worth, N. Makris, and M. R. Patti, “Precise segmentation of the lateral ventricles and caudate nucleus in MR brain images using anatomically driven histogram”, *IEEE Transactions on Medical Imaging*, Vol. 17, pp. 303-310, 1998.

[Xia04] Y. Xia, Q. Hu, A. Aziz, and W. L. Nowinsky, “A knowledge- driven algorithm for a rapid and automatic extraction of the human cerebral ventricular system for MR meuroimages”, *Neuroimage*, Vol. 21, pp. 269-282, 2004.

[Xu97] C. Xu and J. L. Prince, “Gradient vector flow: a new external force for snakes”, *In Proceedings of IEEE Conference on Computer Vision and Pattern Recognition (CVPR) 1997*, pp. 67-71, 1997.

[Xu98] C. Xu and J. L. Prince, “Snakes, shapes, and gradient vector flow”, *IEEE Transactions on Image Processing*, Vol. 7(3), pp. 359-369,

1998.

[Yin10] H. Yin and T. Y. Leong, "A model-driven approach to imbalanced data sampling in medical decision making", In *Proceedings of the 2010 World Congress on Medical Informatics (MEDINFO 2010)*, Cape Town, South Africa, 2010.

[Yushkevich06] P. A. Yushkevich, and J. Piveb, "User-guided 3D active contour segmentation of anatomical structure: significantly improved efficiency and reliability", *Neuroimage*, Vol. 31(3), pp. 1116-1128, 2006.

[Zheng02] Y. Zheng, C. Liu, X. Ding, and S. Pan, "A form frame-line detection algorithm based on directional single-connected chain", *Journal of Software*, Vol. 13, pp. 790-796, 2002.